Design of a Novel Deployable Baffle for a Deployable Space Telescope

V. Nagy

Technische Universiteit Delft

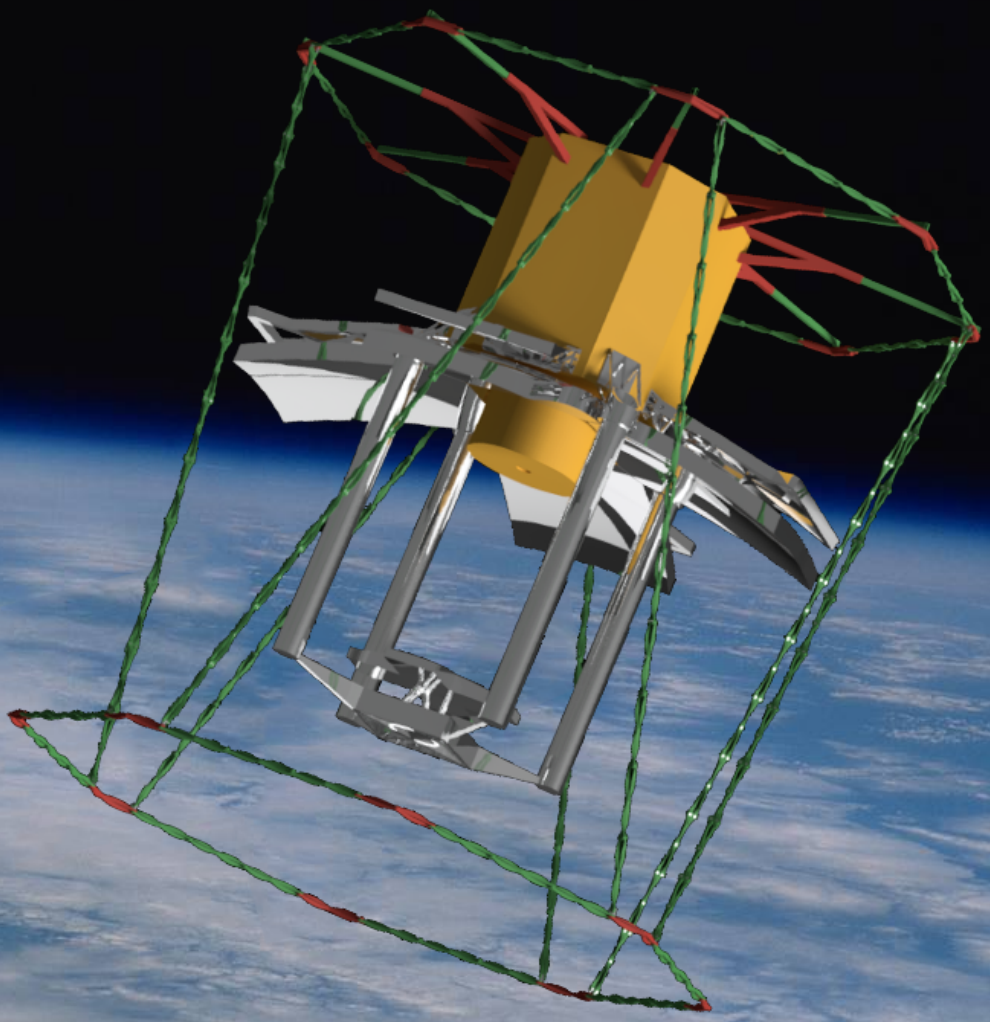

TU Delft

Design of a Novel Deployable Baffle for a Deployable Space Telescope

by

V. Nagy

to obtain the degree of Master of Science
at the Delft University of Technology,
to be defended publicly on Monday August 23, 2021 at 09:00 AM.

Student number:	4890868	
Project duration:	March 1, 2020 – August 23, 2021	
Thesis committee:	Ir. J. Bouwmeester,	TU Delft, supervisor
	Prof. dr. E.K.A. Gill,	TU Delft, chair
	Ir. I. Uriol Balbín,	TU Delft, examiner
	Ir. V. Villalba Corbacho,	TU Delft

An electronic version of this thesis is available at `http://repository.tudelft.nl/`.

TU Delft

Summary

The need for Earth observation telescopes with high spatial and temporal resolution is constantly increasing, however, current state-of-the-art telescopes are costly.

The Deployable Space Telescope project at TU Delft aims to provide a solution with an Earth observation telescope that has the same optical performance as today's best ones, but at a reduced cost. Cost reduction is achieved by decreasing the launch mass and volume of the telescope by making it deployable.

A baffle is required to surround the telescope to provide stable thermal environment, limit stray-light, and protect the optical components from debris. Because the telescope is deployable, the baffle needs to be deployable as well.

Two previous baffle designs already exist for the Deployable Space Telescope: an inflatable one by E.A. Korhonen, and a second one with telescopic deployment by J.W. Arink. The inflatable baffle did not meet the mass and volume requirements, and lacked stiffness in stowed configuration, and while the telescopic baffle corrected these flows, none of them could provide the required thermal environment for the telescope components without using active thermal control, and neither of them addressed the actuation and deployability of the baffle properly.

The initial visual spectral range of the telescope has been changed during this thesis to thermal infrared because of increased funding opportunities, novelty, and technical perspective, therefore the proposed baffle is already for the thermal infrared Deployable Space Telescope.

A deployable baffle consisting of pantographic arms has been designed, which has only one degree of freedom, therefore the whole structure follows the configuration change if one angle is changed in it, and the diameter and height change happen synchronously. This property is useful for the actuation, as reduced number of actuators is required compared to other structures with decoupled radial and axial deployment.

The proposed thermal solution with two layers of MLI, OSR-like baffle outer coating, Magic black inner coating, and a truncated cone considerably decreases the thermal gradients and temperature extremes within the baffle, and successfully shifts the overall temperature of the telescope towards colder regions, with which lower self-emittance is achieved that is useful for infrared telescopes.

Eight torsion springs are placed in the structure to actuate its deployment, and their strategic placement and amount ensures symmetric deployment with limited internal stresses. The structure is held down with cables in stowed configuration that are cut with thermal knives upon the arrival of the deployment command. The final locking of the deployed structure is achieved by latching pins.

Because of the recent change to thermal infrared spectral range, the mission requirements and budgets are not yet updated, consequently the compliance to them cannot be checked. However, a novel solution for a deployable baffle is proposed that facilitates the deployment by having one degree of freedom, and with the presented geometrical relationships the baffle can be modified to any size, if required.

Preface

Per aspera ad astra. /Motto of Gouda/

What a ride. It is my greatest pleasure to write these lines, finalizing more than one year's work. I would like to express by gratitude towards all the people who helped me take this journey. My greatest gratitude goes to my supervisor, Jasper Bouwmeester, followed by my family, who were always by my side. Big thanks to the members of the DST project, you are great, and keep up with the good work!

V. Nagy
Gouda, July 2021

Abbreviations

ADAM	Able Deployable Articulated Mast
ADCS	Attitude Determination and Control System
AHP	Analytic Hierarchy Process
AIT	Assembly, Integration and Test
AO	Atomic Oxygen
B2IH	Baffle to Instrument Housing
CSG	Centre Spatial Guyanais
CSPDA	Cable-Stiffened Pantographic Deployable Antenna
CTE	Coefficient of Thermal Expansion
CTM	Collapsible Tubular Mast
BOL	Beginning of Life
CORE	Compliant Rolling-contact Element
DST	Deployable Space Telescope
ECSS	European Cooperation for Space Standardization
EO	Earth Observation
EOL	End of Life
FAST	Folding Articulated Square Truss
FEM	Finite Element Method
GSD	Ground Sampling Distance
HDRM	Hold Down and Release Mechanism
ITAR	International Traffic in Arms Regulations
M1	Primary Mirror
M2	Secondary Mirror
M3	Tertiary Mirror
MLI	Multi-layer Insulation
MMOI	Mass Moment of Inertia
MTBF	Mean Time Between Failures
OSR	Optical Solar Reflector
PRISM	Picosatellite for Remote Sensing and Innovative Space Missions
SEDOBA	Strain Energy Deployable Optical Barrel Assembly
SMSS	Secondary Mirror Support Structure
STEM	Storable Tubular Extendible Member
TBC	To Be Checked
TBD	To Be Decided
TCS	Thermal Control System
TIR	Thermal Infrared
TU Delft	Delft University of Technology
TV/TB	Thermal Vacuum and Thermal Balance
VIS	Visual (Spectrum)

List of Figures

List of Tables

Contents

1 Introduction

This thesis presents the design process of a deployable baffle for the Deployable Space Telescope (DST). The DST project at TU Delft aims to design an Earth observation (EO) telescope that provides the same optical performance as today's the state-of-the-art EO telescopes for a fraction of cost by making the telescope deployable, therefore saving on launch volume and mass. A baffle is required to surround the telescope mirrors to provide a stable thermal environment for them, to limit the stray-light reaching the detector, and to protect from space debris. The deployability of the telescope necessitates that the baffle is deployable as well, which makes the design of the baffle an interesting multi-disciplinary challenge.

This chapter introduces the Deployable Space Telescope project, describes its novelty, presents existing telescope baffle designs, formulates the research question for the thesis, and provides a methodology to the design process.

1.1. Deployable Space Telescope Project

The Deployable Space Telescope (DST) project at TU Delft has been initiated by recognizing the growing need for Earth observation satellites with increased temporal and spatial resolution. The state-of-the-art Earth observation alternatives (WorldView-3/4) are really costly, but it can be made cheaper by providing the same resolution with a smaller and lighter satellite. Such a satellite can be made with deployable optics: by splitting up the primary mirror (M1) into deployable segments, and placing the secondary mirror on deployable booms, the launch volume can be reduced by a factor of 4, considerably decreasing the launch costs [15]. The lower costs facilitate the formation of constellations, this way reducing the revisit time and increasing the temporal resolution.

The market conditions are translated to the project's Need Statement [30]:

"There is a need for a dramatic decrease in launch cost of high-resolution Earth observation telescopes to provide data with a higher temporal resolution and at a lower price than is currently available."

The DST project aims to fill this market gap with the Deployable Space Telescope. The Mission Statement [30]:

"The goal of this project is to design and develop a Deployable Space Telescope (DST) that is capable of achieving the same GSD as state-of-the-art Earth Observation satellites for a fraction of the costs, by designing it to have a very low stowed volume and mass."

The DST project is supervised and managed by academic staff, and developed in details by an annually renewing group of master students. The project members are shown in Figure 1.1 with the specific field they work(ed) on, and with the finish year of their theses in parentheses.

The schematic design of the DST is shown in Figure 1.2. The primary mirror segments are folded in stowed configuration to be parallel to the side of the instrument housing. The secondary mirror situates closer to the field stop in stowed configuration. The stowage of the primary mirror decreases the width, while the stowage of the secondary mirror decreases the height of the telescope. The deployable baffle is attached to the instrument housing, and surrounds the primary and secondary mirrors.

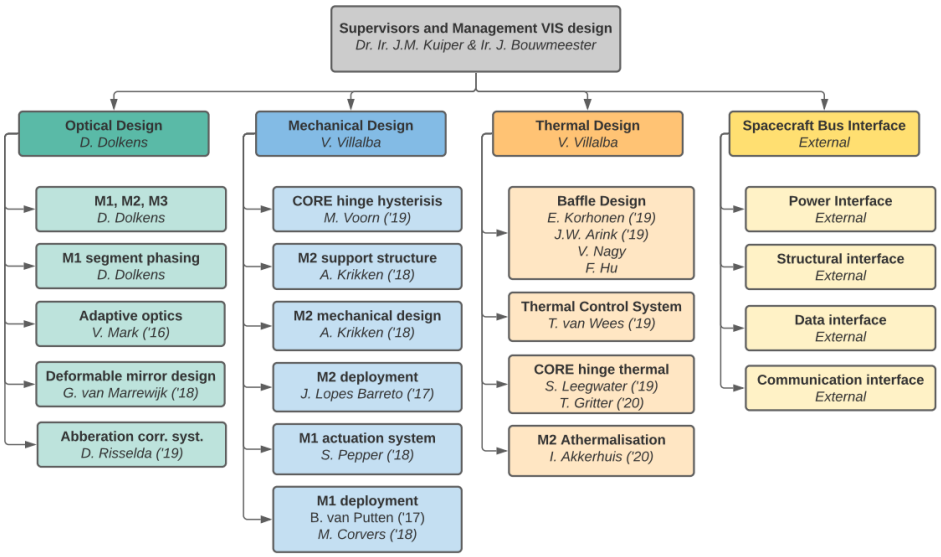

Figure 1.1: *Organisational structure of the Deployable Space Telescope project. [11]*

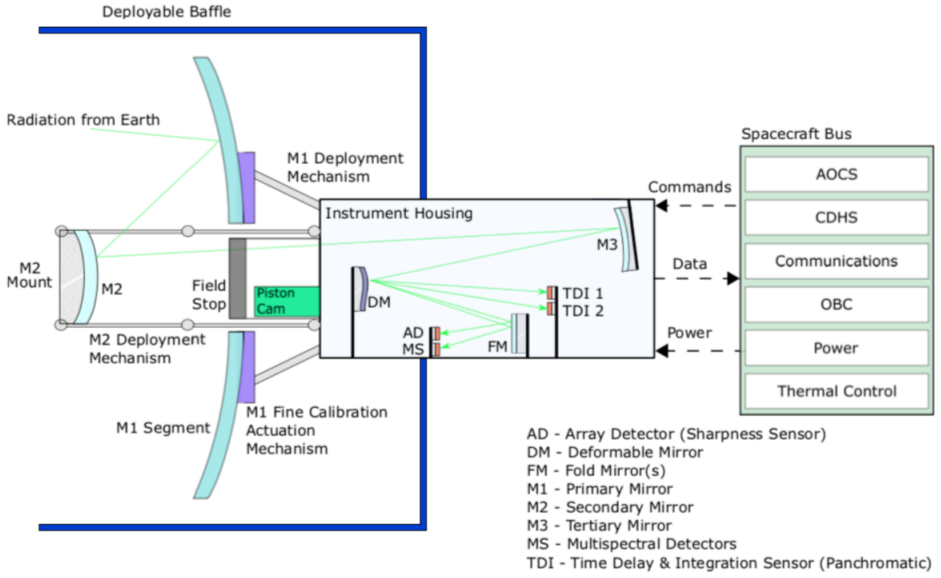

Figure 1.2: *Schematic design of the Deployable Space Telescope. [39]*

The resolution of an Earth observation satellite is described by its ground sampling distance (GSD), the distance of two pixels measured on the ground. The DST has a GSD of 25 cm/pixel at 500 km altitude in one panchromatic channel from 450 to 650 nm, the same as WordView-4 has (corrected for the different altitudes). The orbit of the DST is a Sun-synchronous orbit with Local Time of Descending Node of 10:30 [5].

1.2. Space Telescope Baffles

Equipping space satellites with baffles is a proven way to limit stray-light and provide a stable thermal environment for the optical components. A selection of launched/proposed baffles is presented in this section to provide an overview and baseline about the best practices for baffles. The listing is limited to (quasi)cylindrical baffles, as the low Earth orbit prohibits the use of one-sided shielding, like the sunshields of the James Webb Space Telescope.

The easiest and most used baffle technology in space is a monolithic baffle that cannot be deployed, but has its final shape and volume already at launch. The most famous example is the Hubble Space Telescope, which contributed to ground-breaking discoveries since 1990. WorldView-4 is an Earth observation telescope

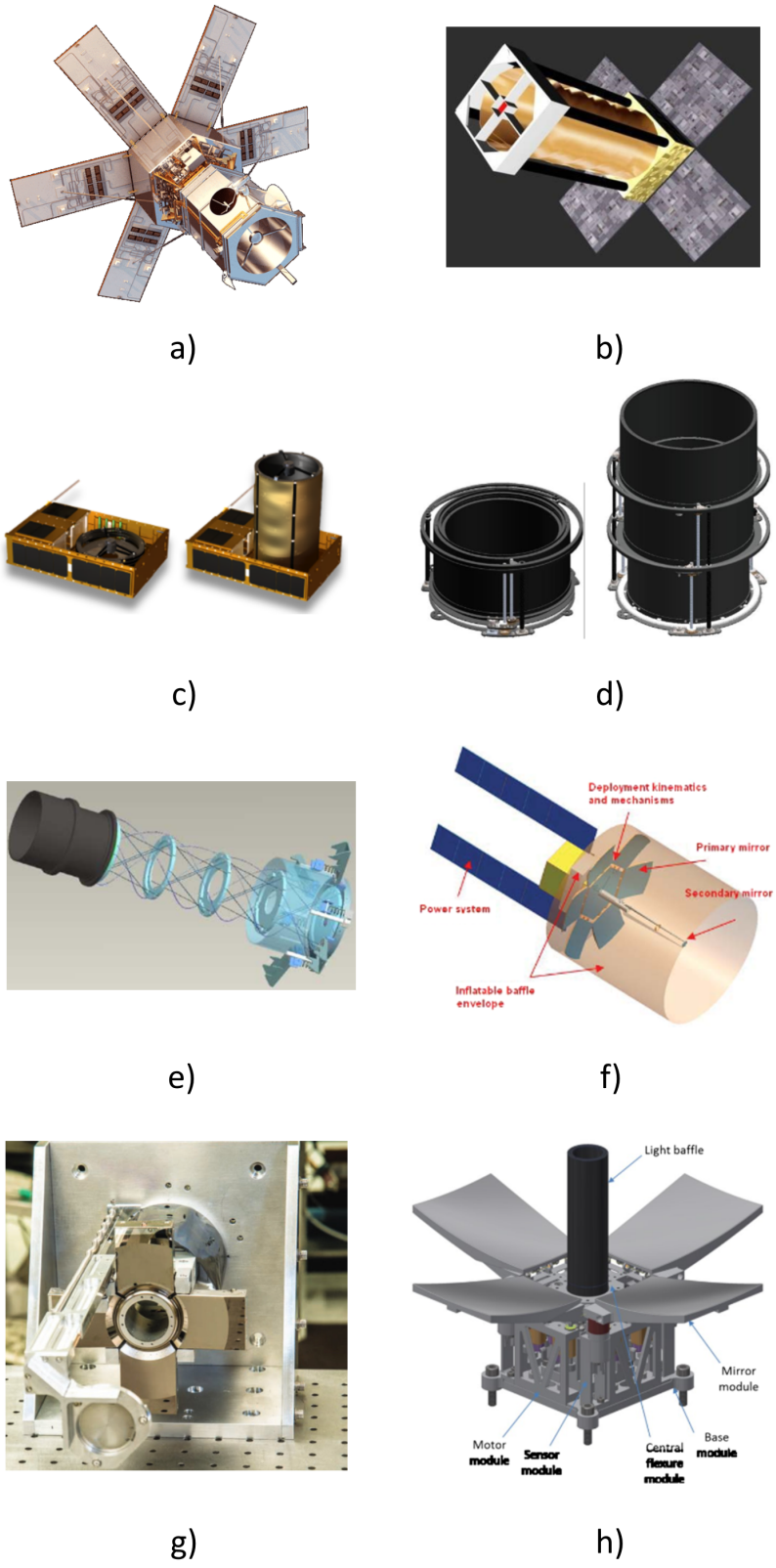

Figure 1.3: *An overview of space telescope baffles. a) WorldView-4 satellite [Courtesy of ESA], b) Dobson Space Telescope, c) Collapsible Space Telescope, d) Surrey Satellite Technologies Limited deployable telescope, e) Picosatellite for Remote Sensing and Innovative Space Missions, f) Large Aperture Telescope Technology satellite, g) Deployable Petal Telescope, h) Deployable Space Telescope (UK Astronomy Technology Centre) [49]*

(Figure 1.3a) launched in 2016 that is equipped with a fixed baffle, and serves as the baseline for the DST in imaging resolution.

There are several telescope concepts with deployable optics that only increase the focal length with the deployment of the secondary mirror, but does not increase the aperture diameter with a deployable primary mirror. The deployment of the baffle for these telescopes are fairly simple as it is usually done by attaching a baffle shroud to the deployable element that pulls the shroud taut when deployed. The Dobson Space Telescope (Figure 1.3b) was proposed by a team of researchers at TU Berlin. The deployment of its secondary mirror is achieved by a rigid deployable truss, which deploys the baffle as well [49]. The Collapsible Space Telescope (Figure 1.3c) deploys its secondary mirror with strain energy stored in coiled masts, while deploying the baffle synchronously. Surrey Satellite Technologies Limited proposed a telescope (Figure 1.3d) with telescopic barrels, in which the telescopic segments are deployed with lead screws. The Picosatellite for Remote Sensing and Innovative Space Missions (PRISM) is the only launched satellite (Figure 1.3e) from this list, with coiled masts deploying the secondary mirror and the baffle, similarly to the Collapsible Space Telescope [49].

The next group of space telescopes include telescopes with deployable primary mirror segments, and they may or may not deploy the secondary mirror. In these cases the aperture diameter is increased by M1 deployment, and the focal length increase depends on the deployability of the secondary mirror. The Large Aperture Telescope Technology project proposed a satellite (Figure 1.3f) with deployable primary and secondary mirrors by means of elastic memory composite hinges. The baffle is inflatable, and surrounds the entire telescope to limit stray-light [49]. The Deployable Petal Telescope (Figure 1.3g) unfolds it primary mirror and linearly deploys its secondary mirror, but a collapsible baffle is only present in the space between the mirrors. This arrangement helps with the mitigation of stray-light, but does not provide a stable thermal environment for the telescope. In the Deployable Space Telescope proposed by UK Astronomy Technology Centre (Figure 1.3h) both mirrors are deployable, and a baffle is present between the mirrors to limit stray-light.

Based on the presented list and a collection of deployable space telescopes by Villalba [49] the baffle of the deployable space telescopes either deploys in single dimension (on-axis) only, or situates between the primary and secondary mirror, providing only stray-light protection, but not stable thermal environment. The only concept that has a deployable baffle deployed in 3D is the Large Aperture Telescope Technology project, however, its inflatable baffle is not detailed. In this sense TU Delft's Deployable Space Telescope is a novel project with deployed primary and secondary mirrors, and with a baffle that deploys in 3D, both increasing its diameter and axial size.

1.3. Problem Description

The function of the baffle in the Deployable Space Telescope is threefold:

1. **Stable thermal environment.** The baffle provides a stable thermal environment for the optical components of the telescope. Without a stable thermal environment the thermo-elastic deformations of the telescope components degrade the optical performance.

2. **Stray-light mitigation.** The baffle minimizes the stray-light that reaches the detector. Only the light coming from the optical field of view is useful, the rest corrupts the telescope performance.

3. **Protection from space debris.** Without the baffle the optical parts of the telescope are directly exposed to space debris and micrometeoroids. The third function of the baffle is to provide protection to the optical parts from them.

All three of the baffle functions are of elemental importance, and show that without the baffle the DST could not perform its mission. As the primary and secondary mirrors are deployable, the baffle needs to be deployable as well to minimize the stowed volume of the satellite.

The work in the DST project is picked up after two baffle designs that failed to comply with the thermal requirements, and none of them addressed the actuation and the deployability of the baffle properly. An inflatable baffle has been proposed by E.A. Korhonen [24], that did not meet the mass and volume requirements, and lacked stiffness in stowed configuration. The next iteration has been made by J.W. Arink [5], who designed a telescopic baffle for the DST. This baffle complied with the mass and volume budget, but still could not provide the required thermal environment for the telescope components without using active thermal control.

To address the shortcomings of the previous baffle designs, a third iteration is made in this thesis. The Thesis Need Statement [34]:

"To ensure the compliance with the optical requirements by maintaining stable thermal environment, there is a need for a new thermomechanical design for the deployable baffle of the DST with increased feasibility of the deployment system, while meeting mass-, volume-, and structural requirements."

Based on this, the Research Question is formulated [34]:

"What are the most effective strategies to improve the deployability of the baffle of the Deployable Space Telescope, while ensuring compliance with thermal-, mass-, volume-, and structural requirements and budgets?"

1.4. Change to Thermal Infrared

During the work on the thesis an important decision has been made by the project leaders: the DST is to be redesigned so that it no longer works in the visual spectrum (VIS) of light, but rather in the thermal infrared (TIR). The reasons for the change include increased funding opportunities, novelty, and technical perspective.

The updated organisational structure for the VIS DST is shown in Figure 1.4.

For the new light spectrum a completely new set of mirrors has been designed, and that has practically restarted the project. As this decision has been made during writing this thesis, it includes legacy VIS topics as well as chapters that are concerned with the TIR telescope. Until (and including) the Deployment Mechanism Trade-off (Chapter 3) the VIS telescope, and from the Preliminary Thermomechanical Design (Chapter 4) the TIR telescope is discussed. To avoid confusion the chapters clearly indicate if they are about the TIR telescope.

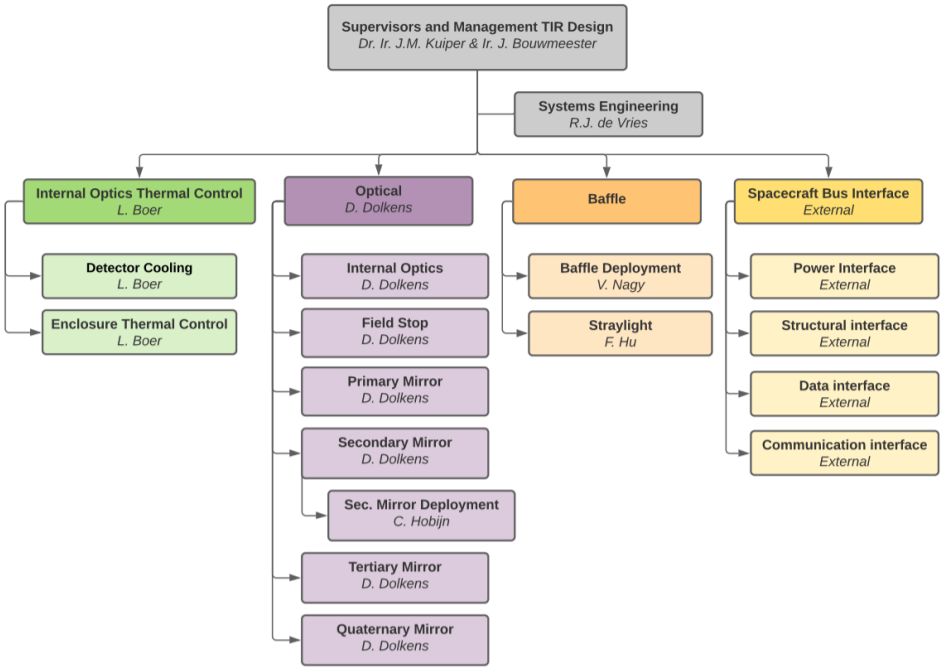

Figure 1.4: *Organisational structure of the TIR Deployable Space Telescope project. [11]*

1.5. Methodology

The design steps are presented below.

1. **Requirement Review [VIS, Chapter 2].** The design process of the deployable baffle starts with reviewing the requirements that have already been collected in the past theses for the DST baffle, and based on them a new, updated set of requirements are collected. The requirements not only constrain the design process, but also give goals to optimize for, therefore facilitating trade-offs. A complete set of requirements is of elemental importance for an engineering design process.

2. **Deployment Mechanisms Trade-off [VIS, Chapter 3].** A trade-off is performed among deployment mechanism alternatives to select the best one to use in the baffle. The process starts with the definition of the method of the trade-off, followed by the identification of the decision criteria and alternatives. Then, group decision making is utilized in the criteria weighing to limit the subjectivity of the trade-off. The process ends with sensitivity analysis. The deployment mechanisms trade-off is arguably the most important part of the thesis, with the result affecting the rest of the work. Great emphasis is placed on selecting the criteria that steer the trade-off in accordance with the requirements collected previously.

3. **Preliminary Thermomechanical Design [TIR, Chapter 4].** The deployable baffle is designed with the deployment mechanism that won the trade-off. Based on a preliminary mechanical design that defines the dimensions of the baffle a thermal study is prepared, with which the baffle geometries, materials, and additional appendages are selected. At the end of this step the achievable thermal environment within the baffle is presented.

4. **Detailed Mechanical Design [TIR, Chapter 5].** The baffle geometry is worked out in detail, and is optimized for the requirements and budgets. Its integration with the rest of the telescope is performed, and its actuation is discussed. This step is partially an optimization of the preliminary design discussed previously to help with better requirement and budget compliance. Furthermore, additional mechanisms are introduced to promote the feasibility of the deployment and the actuation of the baffle.

2

Requirements Review

Korhonen and Arink both collected a list of requirements for their baffle designs for the VIS Deployable Space Telescope. In this chapter these requirements are compared, reviewed, updated, and supplemented, resulting in an up-to-date list of requirements for the TIR DST.

2.1. Comparison

This thesis is the third iteration of the baffle design for the Deployable Space Telescope, therefore the requirement generation starts with the collection and review of the baffle requirements from the previous two theses. The requirements of Arink and Korhonen are collected in a comparison table (see Table 2.1) in such a way that same or similar requirements are collected in one row. The requirements are given new numbers (first column) to facilitate referencing.

Requirements #1-5 are practically the same in both theses. The 30 g quasi-static load requirement originates from Pepper's thesis [39], and has been reused ever since. The value seems to be very high, therefore it is recommended to cross-check it with the possible launcher datasheets. Requirements #6-7 are only present in Arink's work. Requirement #7 might change with a different SMSS design (see Section 3.6.6) therefore it is recommended to be checked later.

Arink has more detailed requirements concerning successful deployment (#8-17). Requirement #8 is different in the two theses, but both are important. Arink's requirement needs clarification about the reliability of the deployment, although it cannot be quantified without an extensive reliability analysis. Requirement #9 is vague, a better formulation is recommended. Requirements #10 and #12 should be supplemented with condition "during deployment". Requirement #13 should give at least an indication about the deployment accuracy: 50 mm seems like a balance between an impossible requirement and having serious effects of the misalignment. Nevertheless, the optical and thermal effects need to be checked and then the requirement revisited. Requirement #15 prescribes different clearances in the two theses, out of which the smaller (100 mm) is favoured, as 200 mm clearance would increase the baffle stowed volume unreasonably. Furthermore, Akkerhuis raised a flag that the SMSS booms intersect the baffle in stowed configuration [3], and later further problems have been found with the SMSS (see Section 3.6.6). Consequently, requirement #15 needs to be changed to consider more DST components and all configurations.

Requirements #18-22 concern the thermal and optical environment. Korhonen's version of requirement #18 is too specific, which could drive the design, therefore Arink's one is kept. Requirement #19 is not backed up by Arink, therefore it is preferred to use #18 instead. For requirement #20 Arink's formulation is broader and includes Korhonen's one. Requirement #21 is vague, it is recommended to include a value. Requirement #22 has usable parts in both previous theses: IR wavelengths are not important from the optical point of view as the detector is not able to pick it up [14]. The 90% limit of the incident radiation is a good starting point, but only if it is backed up stray-light modelling and/or budgeting.

Arink included much more requirements for survival in space environment than Korhonen (requirements #23-37). Requirement #23 contains methodology and is not formulated as a requirement. The debris size should be checked and the meaning of survival specified in requirement #24. Three separate requirements are recommended instead of requirement #26. Requirement #29 should not specify a temperature (range), the survival should be based on the simulated extreme hot and cold conditions. Arink's 0.9 Hz limit in re-

quirement #36 stems from Korhonen's thesis, in which she concluded that with 0.92 Hz first eigenfrequency in deployed configuration the structure withstands the operational loads [5]. The value is recommended to be checked, but in a collaborative NASA/DLR project [6] a boom was required to have deployed first eigenfrequency of 0.05 Hz (or higher), to be used in small satellites. Compared to that, 0.9 Hz is 18x higher. Requirement #37 originated from Krikken's thesis [25], but with a new SMSS designs the value needs to be checked. In requirement #38 the part "over the mission lifetime of the DST" should be removed because the baffle does not have operational costs. In the absence of the DST cost budget the cost cannot be specified yet.

The safety requirements (#39-51) are again more elaborated by Arink. Requirement #40 should be removed as it is not a requirement on the system. Requirement #42 might drive the design too much, and a reliability target is already set with the reformulation of requirement #8. In requirement #46 Arink used the method of NASA to account for temperature uncertainties (±5 K), previously van Wees used the method described in ECSS (±15 K) [48]. ECSS is recommended to be used in Europe.

Requirement #61 originates from literature, as there is no overall mass budget for the spacecraft. 15 kg is a good starting point, but the value needs to be checked when the mass budget becomes available. Requirement #64 should be given a value. It is foreseen that it can be relaxed, and half an hour is recommended as a first estimate, but it needs to be checked later.

Table 2.1: *Comparison of Arink's and Korhonen's requirements.*

	Arink		**Korhonen**	
#	**ID**	**Requirement**	**ID**	**Requirement**
Survive Launch				
1	BAF-MEC-03	The baffle shall survive the launch in stowed configuration.	BAF-STRU-01	The stowed baffle system shall survive launch.
2	BAF-MEC-03-01	The baffle shall survive a quasi-static load of 30g applied simultaneously to the x- and y- axes in the launcher coordinate frame in the stowed configuration during launch.	BAF-STRU-01-01	The stowed baffle system shall withstand up to 30 g of quasi-static acceleration applied simultaneously in the x- and y-axes in the launcher coordinate frame.
3	BAF-MEC-03-02	The baffle shall survive a quasi-static load of 30g applied simultaneously to the x- and z- axes in the launcher coordinate frame in the stowed configuration during launch.	BAF-STRU-01-02	The stowed baffle system shall withstand up to 30 g of quasi-static acceleration applied simultaneously in the x- and z-axes in the launcher coordinate frame.
4	BAF-MEC-03-03	The baffle shall survive a quasi-static load of 30g applied simultaneously to the y- and z- axes in the launcher coordinate frame in the stowed configuration during launch.	BAF-STRU-01-03	The stowed baffle system shall withstand up to 30 g of quasi-static acceleration applied simultaneously in the y- and z-axes in the launcher coordinate frame.
5	BAF-MEC-03-04	The baffle shall have a minimum first eigenfrequency of 100 Hz in stowed configuration.	BAF-STRU-01-04	The stowed baffle shall have a first eigenfrequency above 100 Hz.
6	BAF-T-04	The stowed baffle shall survive a heat flux of 1135 W/m2 immediately after separation of the fairing.		
7	M2-T-01	The bulk temperature of the booms shall not exceed 373K during stowage.		
Successful Deployment				
8	BAF-MEC-04	The baffle shall deploy succesfully.	BAF-MEC-01	The baffle shall be deployable.
9	BAF-MEC-04-03	The baffle shall survive deployment.		
10	BAF-MEC-04-03-01	The baffle shall survive local- and global buckling loads.		
11	BAF-MEC-04-03-02	The baffle shall survive deployment shocks and vibrations.		

12	BAF-MEC-04-03-04	The baffle shall mitigate the creation of hot-spots such that it shall not result in consequential structural- or thermal damage that does not conform to the operational requirements.		
13	BAF-MEC-04-04	The baffle shall achieve a deployed configuration that conforms to the operational requirements with a position accuracy of TBD m.		
14	BAF-MEC-04-04-02	The baffle geometry shall not obstruct any telescope elements and not interfere with the optical performance.	BAF-MEC-06	The baffle shall not obstruct any other telescope elements during any part of the mission.
15	BAF-MEC-04-04-02-01	The baffle shall have a clearance of 200 mm in deployed configuration between M1 and any point of the baffle.	BAF-MEC-06-02	The deployed baffle shall have a clearance of >100 mm from M1 in every direction.
16	BAF-MEC-04-05	The baffle shall not impede the deployment of the primary- and secondary mirror.	BAF-MEC-06-04	The deployed baffle shall not interfere with the deployment of the primary and secondary mirror elements.
17	BAF-MEC-04-05-01	The baffle shall deploy before the primary- and secondary mirror.	BAF-MEC-06-03	The baffle shall be deployed before the primary and secondary mirror elements.
Perform Operations				
18	BAF-T-01	The baffle shall create a stable thermal environment for all sub-systems, so that the mechanical displacement budgets will be met.	BAF-THE-03	The deployed baffle shall have an effective emissivity of at most <TBD>.
19	BAF-T-01-01	The temperatures of all sub systems within the baffle shall remain within a stability bandwith of 253-323 K.		
20	BAF-T-01-02	The baffle shall maintain its operational functionality in both extreme cases of BOL- and EOL thermo-optical material properties.	BAF-MEC-08-01	The deployed baffle shall survive the space environment for 5 years without a loss in the optical properties of more than TBD.
21	BAF-O-01	The baffle shall mitigate stray-light in deployed configuration.		
22	BAF-O-01-01	The internal layer of the baffle shall absorb at least 90 % of incident radiation in both UV- and IR wavelength spectra.	BAF-OPT-01	The inner surface of the baffle shall absorb at least <TBD>% of radiation in the wavelength range 450-700 nm.
Survive OPS & Space Environment				
23	BAF-MEC-07-01	The operational loads shall be added to the in-orbit loads.		
24	BAF-MEC-07-02	The baffle shall survive the impact of medium sized debris, 1 <d <100mm.		
25	BAF-MEC-07-03	The materials to be used for the baffle shall limit outgassing to a TML of <1 % and CVCM of <0.01 %.		
26	BAF-MEC-07-04	The baffle shall be resistant to AO and plasma/ionizing radiation.		
27	BAF-MEC-07-04-01	The baffle shall avoid electrical charging.		
28	BAF-T-02	The baffle shall survive the thermal operational- and environmental loads in deployed configuration.		
29	BAF-T-02-01	The baffle shall survive extreme hot and cold temperatures between -250 °C and +177 °C respectively.	BAF-THE-01	All baffle elements shall survive temperatures up to 393 K.

30	BAF-T-02-02	The baffle shall survive the thermal loads both with BOL- and EOL optical properties.		
31	BAF-MEC-07-06	The baffle shall survive the mechanical operational- and environmental loads in deployed configuration.	BAF-MEC-08-02	The baffle shall maintain its structural integrity for 5 years.
32			BAF-STRU-03	The deployed baffle shall structurally survive the micro-gravity environment.
33	BAF-MEC-07-06-01	The baffle shall survive on-board vibrations of TBD due to the reaction wheel in deployed configuration.		
34	BAF-MEC-07-06-02	The baffle shall mitigate the effect of thermal flutter in deployed configuration.		
35	BAF-MEC-07-06-03	The baffle shall survive vibration fatigue due to on-board vibrations and thermal flutter.		
36	BAF-MEC-07-06-03-01	The baffle structure shall have a minimum first eigenfrequency >0.9 Hz in deployed configuration.	BAF-STRU-02	The deployed baffle shall have a first eigenfrequency above <TBD>Hz.
37	M2-T-02	The bulk temperature of the booms shall not exceed 473K when deployed.		
Cost				
38	BAF-SYS-01	The total cost of the baffle shall be no more than TBD over the mission lifetime of the DST.		
Safety				
39	BAF-SYS-02	The baffle shall have an operational expected lifetime of 5 years.	BAF-MEC-08	The baffle shall survive the space environment for 5 years.
40	BAF-SYS-02-01	All single point of failure modes of the baffle and its sub-components shall be identified.		
41	BAF-SYS-02-02	The baffle shall have a MTBF of at least 5 years for single point of failure components.		
42	BAF-SYS-02-03	All single point of failures should be eliminated by redundant components.		
43	BAF-SYS-03	Active elements of mechanisms, such as sensors, motor windings, brushes, actuators, switches and electronics, shall be redundant if a mechanism is is not completely redundant.		
44	BAF-SYS-04	The baffle shall use space qualified parts, materials and procesess (PMP).		
45	BAF-SYS-05	The baffle shall be designed such that conformance to performance requirements can be demonstrated by thermal analyses and thermal test.		
46	BAF-SYS-06	Verification by analysis shall take into account uncertainties: a 5 degrees temperature calculation uncertainty margin and 25 % mass uncertainty.		
47	BAF-SYS-07	The baffle shall be designed using factors of safety (FoS) conform with ECSS-E-ST-32-10.		
48	BAF-SYS-07-01	The baffle shall use a minimum yield stress safety factor (FoS) of 1.25 for standard metallic materials		
49	BAF-SYS-07-02	The baffle shall use a minimum ultimate stress safety factor (FoS) of 1.5 for standard metallic materials.		

50	BAF-SYS-07-03	The baffle shall use a minimum buckling safety factor (FoS) of 2 for standard metallic materials.		
51	BAF-SYS-07-04	The baffle shall use a minimum fatigue safety factor (FoS) of 4 for standard metallic materials.		
Regulations				
52	BAF-SYS-08	The baffle shall not use any ITAR controlled components or technologies	BAF-SYS-02	The system shall not include ITAR restricted components.
53	BAF-SYS-09	The baffle shall not comply with national and international regulations during AIT activities, launch, operations and EOL.	BAF-SYS-01	The stowed baffle system shall adhere to the CSG safety regulations.
Flexibility				
54	BAF-SYS-10	The baffle design shall incorporate flexibility to accommodate modifications of requirements imposed on the TCS and deployement system during the project development phase.		
55	BAF-SYS-11	The baffle design shall incorporate flexibility to offer design trimming capabilities to accommodate late requirement updates.		
Constraints				
56	BAF-SYS-12	The volume of the baffle shall not exceed 1.5 m3 (threshold) / 0.75 m3 (goal) when in stowed configuration.	BAF-MEC-03	The stowed baffle shall increase the volume of the DST by at most 0.1 m3 (goal)/ 0.85 m3 (threshold).
57	BAF-SYS-13	The stowed baffle shall not require any power during launch.		
58	BAF-SYS-14	The operational functionality of the baffle, as well as the ability to survive the operations and space environment shall be compatible with the power- and radiation exchange of the solar panels.		
59	BAF-SYS-15	The baffle in deployed configuration should fit inside a TV/TB chamber to allow for thermal testing.		
60	BAF-SYS-15-01	The maximum volume of the baffle in deployed configuration shall conform to the usable volume of the Large Solar Simulator from ESA/ESTEC: 10 m diameter and 15 m height.		
61	BAF-SYS-16	The mass of the entire baffle including deployment mechanism shall not exceed 15 kg.	BAF-MEC-07	The total mass of the baffle and its deployment mechanism shall be at most 15 kg.
62	BAF-SYS-17	The baffle shall be given sufficient structural support by other sub-systems.	BAF-MEC-02	The baffle system shall be attached to the outside of the instrument bus during stowage and operation.
63	BAF-SYS-18	The baffle shall be manufacturable with compliance to the availability of parts and materials.		
Additional requirements from Arink (not for his thesis)				
64	BAF-MEC-04-03-03	The baffle shall deploy in TBD s within the acceleration range of TBD m/s2.	BAF-MEC-05	The baffle shall fully deploy within <TBD>seconds.

2.2. List of Requirements

Based on the reviewed requirements a new set of requirements is assembled, see Table 2.2. In addition to presenting the requirements, the table states if the requirements would change in case of a change to TIR telescope or not. In the last column the verification methods are presented for each requirement.

Table 2.2: *List of requirements. The third column specifies if the requirement would change in case of a TIR telescope. V.m.: verification method, I: inspection, A: analysis, D: demonstration, T: testing.*

ID	Requirement	TIR?	V. m.
Survive Launch			
BAF-MEC-01	The baffle shall survive the launch in stowed configuration.	No	A/T
BAF-MEC-01-01	The baffle shall survive a quasi-static load of 30g applied simultaneously to the x- and y- axes in the launcher coordinate frame in the stowed configuration during launch (TBC).	No	A/T
BAF-MEC-01-02	The baffle shall survive a quasi-static load of 30g applied simultaneously to the x- and z- axes in the launcher coordinate frame in the stowed configuration during launch (TBC).	No	A/T
BAF-MEC-01-03	The baffle shall survive a quasi-static load of 30g applied simultaneously to the y- and z- axes in the launcher coordinate frame in the stowed configuration during launch (TBC).	No	A/T
BAF-MEC-01-04	The baffle shall have a minimum first eigenfrequency of 100 Hz in stowed configuration.	No	A/T
BAF-T-01	The stowed baffle shall survive a heat flux of 1135 W/m2 immediately after separation of the fairing.	No	A/T
M2-T-01	The bulk temperature of the booms shall not exceed 373K during stowage (TBC).	Possibly	A
Successful Deployment			
BAF-MEC-02	The baffle shall be deployable.	No	I
BAF-MEC-02-01	The baffle deployment mechanism shall have at least TBD % reliability.	No	A/T
BAF-MEC-02-02	The deployment sequcence shall not damage the baffle.	No	A/D
BAF-MEC-02-02-01	The baffle shall survive local- and global buckling loads during deployment.	No	A/T
BAF-MEC-02-02-02	The baffle shall survive deployment shocks and vibrations.	No	A/T
BAF-MEC-02-02-03	The baffle shall mitigate the creation of hot-spots during deployment such that it shall not result in consequential structural- or thermal damage that does not conform to the operational requirements.	No	A
BAF-MEC-02-03	The baffle geometry shall not obstruct any telescope elements and not interfere with the optical performance.	No	I/A/D
BAF-MEC-02-03-01	The baffle shall achieve a deployed configuration that conforms to the operational requirements with a minimal position accuracy of 50 mm (TBC).	No	A/T
BAF-MEC-02-03-02	The baffle shall have a clearance of at least 100 mm in all configarations between any point of the baffle and each of the following elements of the telescope: M1, M2, PMSS, SMSS.	No	I
BAF-MEC-02-04	The baffle shall not impede the deployment of the primary- and secondary mirror.	No	D
BAF-MEC-02-04-01	The baffle shall deploy before the primary- and secondary mirror.	No	D
BAF-MEC-02-05	The baffle shall deploy in 1800 s (TBC).	No	A/T
Perform Operations			
BAF-T-02	The baffle shall create a stable thermal environment for all subsystems located inside the baffle, so that the mechanical displacement budgets will be met.	No	A/T
BAF-T-02-01	The baffle shall maintain its operational functionality in both extreme cases of BOL- and EOL thermo-optical material properties.	No	A
BAF-O-01	The straylight fraction of the incoming radiation on the detector shall be less than 1% (TBC) after correction.	Possibly	A
BAF-O-01-01	The internal layer of the baffle shall absorb at least 90% (TBC) of incident radiation in UV wavelength spectra.	Possibly	A/T
Survive OPS & Space Environment			
BAF-MEC-03	An impact of small sized debris (d <1mm) to the baffle shall not degrade the ability of the DST to continue its mission (TBC).	No	A/T
BAF-MEC-04	The materials to be used for the baffle shall limit outgassing to a TML of <1 % and CVCM of <0.01 %.	No	I
BAF-MEC-05	The baffle shall be resistant to atomic oxygen.	No	I

BAF-MEC-06	The baffle shall be resistant to plasma present in DST orbit.	No	I
BAF-MEC-07	The baffle shall be resistant to ionizing radiation.	No	I
BAF-MEC-08	The baffle shall avoid electrical charging.	No	I
BAF-T-03	The baffle shall survive the thermal operational- and environmental loads in deployed configuration.	No	A/T
BAF-T-03-01	The baffle shall survive extreme hot and cold temperatures (including 15 K modelling uncertainties) bounded by the operational range of all used materials in the baffle.	No	A/I
BAF-T-03-02	The baffle shall survive the thermal loads both with BOL- and EOL optical properties.	No	A/I
BAF-MEC-09	The baffle shall survive the mechanical operational- and environmental loads in deployed configuration.	No	A/T
BAF-MEC-09-01	The baffle shall survive on-board vibrations due to the reaction wheel in deployed configuration.	No	A/T
BAF-MEC-09-02	The baffle shall mitigate the effect of thermal flutter in deployed configuration.	No	A/T
BAF-MEC-09-03	The baffle shall survive vibration fatigue due to on-board vibrations and thermal flutter.	No	A/T
BAF-MEC-09-04	The baffle structure shall have a minimum first eigenfrequency >0.9 Hz in deployed configuration (TBC).	No	A/T
M2-T-02	The bulk temperature of the SMSS booms shall not exceed 473K when deployed (TBC).	Possibly	A
Cost			
BAF-SYS-01	The total cost of the baffle shall be no more than TBD.	Possibly	I
Safety			
BAF-SYS-02	The baffle shall have an expected operational lifetime of 5 years.	Depends on the new mission profile	A
BAF-SYS-02-01	The baffle shall have a MTBF of at least 5 years for single point of failure components.	Depends on the new mission profile	A
BAF-SYS-03	Active elements of mechanisms, such as sensors, motor windings, brushes, actuators, switches and electronics, shall be redundant if a mechanism is is not completely redundant.	No	I
BAF-SYS-04	The baffle shall use space qualified parts, materials and procesess (PMP).	No	I
BAF-SYS-05	The baffle shall be designed such that conformance to performance requirements can be demonstrated by thermal analyses and thermal test.	No	A/T
BAF-SYS-06	Verification by analysis shall take into account uncertainties: a 15 K temperature calculation uncertainty margin and 25 % mass uncertainty.	No	I
BAF-SYS-07	The baffle shall be designed using factors of safety (FoS) conform with ECSS-E-ST-32-10.	No	I
BAF-SYS-07-01	The baffle shall use a minimum yield stress safety factor (FoS) of 1.25 for standard metallic materials.	No	A/T
BAF-SYS-07-02	The baffle shall use a minimum ultimate stress safety factor (FoS) of 1.5 for standard metallic materials.	No	A/T
BAF-SYS-07-03	The baffle shall use a minimum buckling safety factor (FoS) of 2 for standard metallic materials.	No	A/T
BAF-SYS-07-04	The baffle shall use a minimum fatigue safety factor (FoS) of 4 for standard metallic materials.	No	A/T
Regulations			
BAF-SYS-08	The baffle shall not use any ITAR controlled components or technologies.	No	I
BAF-SYS-09	The baffle shall comply with national and international regulations during AIT activities, launch, operations and EOL.	No	I
BAF-SYS-10	The materials used in the baffle shall be non-toxic and have no known negative effect on human health.	No	I

Flexibility			
BAF-SYS-11	The baffle design shall incorporate flexibility to accommodate modifications of requirements imposed on the TCS and deployement system during the project development phase.	No	I
BAF-SYS-12	The baffle design shall incorporate flexibility to offer design trimming capabilities to accommodate late requirement updates.	No	I
Constraints			
BAF-SYS-13	The volume of the baffle shall not exceed 1.5 m3 (threshold) / 0.75 m3 (goal) when in stowed configuration.	Depends on the new mission profile	I
BAF-SYS-14	The stowed baffle shall not require any power during launch.	No	I
BAF-SYS-15	The operational functionality of the baffle, as well as the ability to survive the operations and space environment shall be compatible with the power- and radiation exchange of the solar panels.	No	A
BAF-SYS-16	The baffle in deployed configuration should fit inside a TV/TB chamber to allow for thermal testing.	No	I
BAF-SYS-16-01	The maximum volume of the baffle in deployed configuration shall conform to the usable volume of the Large Solar Simulator from ESA/ESTEC: 10 m diameter and 15 m height.	No	I
BAF-SYS-17	The mass of the entire baffle including deployment mechanism shall not exceed 15 kg (TBC).	Depends on the new mission profile	I
BAF-SYS-18	The baffle shall be given sufficient structural support by other subsystems.	No	I
BAF-SYS-19	The baffle shall be manufacturable with compliance to the availability of parts and materials.	No	I

3

Deployment Mechanisms Trade-off

It is of key importance to select a deployment mechanism of the DST baffle that serves the goals of the DST mission the best. In this chapter the deployment concept alternatives are selected and traded off, resulting in the best possible deployment mechanism that is used in further design steps.

3.1. Trade-off Method

Analytic Hierarchy Process (AHP) has been chosen as the trade-off process to select the best available baffle deployment concept. AHP is a mathematically based trade-off method that can help select the most valuable deployment mechanism while taking into account multiple, and even conflicting decision criteria [21]. AHP is particularly good at group decision making, as individuals' experiences can be used to estimate the relative magnitudes of factors with the help of pair-wise comparisons [43].

The steps of the AHP procedure [21]:

1. Problem definition;
2. Identifying the decision criteria and alternatives;
3. Judging the relative value of alternatives on each criterion (group);
4. Judging the relative importance of the criteria (group);
5. Synthesizing group judgements;
6. Inconsistency analysis;
7. Calculating the weights of criteria and priorities of alternatives, decision making;
8. Sensitivity analysis.

3.2. Problem Description

Before starting the trade-off process, it is important to have a clear picture what the problem is that needs to be solved. There are several deployment mechanisms that – theoretically – could be used for the baffle of the Deployable Space Telescope. Out of these concepts the best one needs to be selected, considering several aspects. To do that reliably, a trade-off process is used.

The main purpose of the baffle is to provide a stable thermal environment for the optical parts of the telescope, while it also needs to limit stray-light and protect against space debris. Because of launch vehicle limitations, the baffle needs to be lightweight and deployable with minimal stowed volume. To minimize the stowed volume, the baffle is expected to deploy in multiple directions: if the baffle shape is simplified to a cylinder, both the radius and the height of the cylinder need to increase during deployment, in other words the baffle needs to deploy radially and axially as well, respectively.

The baffle consists of two main parts: the shroud and the frame (see Figure 3.10, the frame is in silver, the shroud is in dark yellow). To fulfill its function, the most important part of the baffle is its shroud, and the frame just serves to deploy the shroud and keep it in place. However, the same shroud is of only secondary importance with respect to the deployment mechanisms selection: the frame is the mechanism that deploys, but the shroud-frame integration should be considered as well.

Like other spacecrafts, the DST and its subsystems need to be reliable, which places a limit on the complexity of the deployment mechanism. Therefore, passive deployment, or active deployment with as few

actuators as possible are preferred.

Two previous theses have been dedicated previously to the (thermo)mechanical design of the DST baffle by E. Korhonen and J.W. Arink (in chronological order). However, none of them addressed properly the actuation and deployability of the baffle, and none of them could keep the payload in the required temperature range without the need of active control. This thesis aims to fix these shortcomings with a new baffle design.

3.3. Criteria Definition & Grading

Defining the right criteria for the trade-off process is of elementary importance. Korhonen and Arink also used AHP for their trade-offs that resulted in their chosen deployment mechanisms. The criteria used by them are shown in Table 3.1. Korhonen used a limited number of criteria that resulted in the victory of the deployable concept. Arink supplemented them with three additional criteria that changed the winner: telescopic deployment. The eight criteria defined by Arink serve as a good starting point, however, they need to be further supplemented to better consider the deployability and actuation of the baffle.

The grading of the alternatives on each criterion is based on a scale from one to nine, with one being the worst and nine being the best grade. In case of criteria that are quantifiable, grading methods are given. With non-quantifiable criteria pairwise comparisons are to be used to assess the performance of the two alternatives. After the grading, the relative value of the alternatives on each criterion can be given.

Table 3.1: *Criteria used by Korhonen and Arink in previous deployment mechanism trade-offs. [5, 24]*

	Korhonen	**Arink**
Mass	x	x
Stowed volume	x	x
Complexity	x	x
Deployed stiffness	x	x
Heritage	x	x
Stowed stiffness		x
Deployment control		x
Flexibility		x

3.3.1. Mass

The maximal mass of the baffle is controlled by requirement BAF-SYS-17, namely the mass of the entire baffle shall not exceed 15 kg. As no mass budget of the satellite existed at the time of writing this thesis, the 15 kg threshold is an arbitrary one originating from previous theses [5, 24], and could be modified in accordance with other subsystems.

It is favorable to have the baffle mass as low as possible, and above a certain mass the worst grade is given. This threshold mass is chosen to be 30 kg, the double of the current requirement goal. As the preliminary total spacecraft mass is estimated to be 314 kg [27], the selected threshold is less than 10% of the total spacecraft mass, consequently, it is not unreasonably high. Between 0 kg and 30 kg the grades linearly decrease from 9 to 1, as illustrated in Figure 3.1.

Mass range, kg	**Grade**
$0 \leq m < 30$	$9 - 4/15 \cdot m$
$30 \leq m$	1

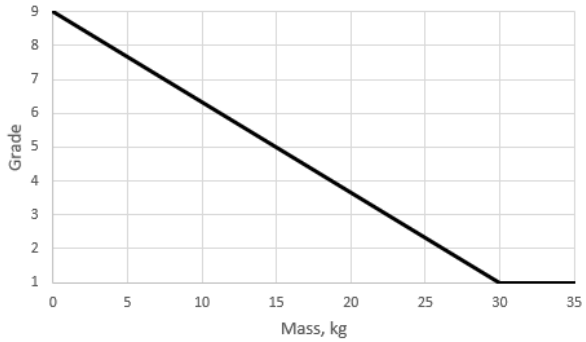

Figure 3.1: *Grading of mass criterion (m: mass).*

3.3.2. Stowed Volume

Similarly to mass, stowed volume is controlled by a requirement (BAF-SYS-13), that aims for stowed volume of less then 0.75 m^3 (goal), but allows stowed volume up to 1.5 m^3 (threshold). This directly originates from a system requirement that allows the same volumes for the instrument. As the baffle represents the outer perimeter of the instrument, the same numbers have been applied to it. The stowed volume of the instrument (without the baffle) poses a lower limit on the stowed volume of the baffle. The stowed volume of the instrument (without the baffle) is $0.76 \times 0.76 \times 1.10\ m^3 = 0.64\ m^3$ [5].

This lower limit is graded with 9, and the grades decrease linearly with increasing stowed baffle volume, and reaches the lowest grade at 2 m^3, as illustrated in Figure 3.2. The upper threshold is approx. 33% higher than the requirement threshold.

Stowed volume range, m^3	**Grade**
$0.64 \leq V < 2$	$217/17 - 100/17 \cdot V$
$2 \leq V$	1

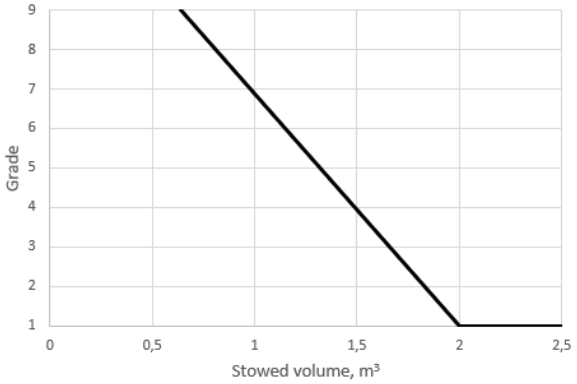

Figure 3.2: *Grading of stowed volume criterion (V: stowed volume).*

3.3.3. Stowed Stiffness

Stiffness in stowed configuration is indispensable to be able to survive AIT and LEOP as it describes the structural integrity of the baffle. With higher stiffness the baffle can better resist to vibrations, therefore higher stiffness is favorable. To quantify the criterion, eigenfrequency is used to describe the stiffness of the baffle, as they are directly correlated. Requirement BAF-MEC-01-04 specifies a minimum eigenfrequency of 100 Hz for the baffle, but higher stiffness is advantageous.

Grading the stowed stiffness is based on Figure 3.3, the eigenfrequency range in which the grades linearly change is between 75 and 125 Hz, with the requirement threshold being in the middle with grade 5.

Stowed eigenfrequency range, Hz	**Grade**
$0 \leq f < 75$	1
$75 \leq f < 125$	$-11 + 4/25 \cdot f$
$125 \leq f$	9

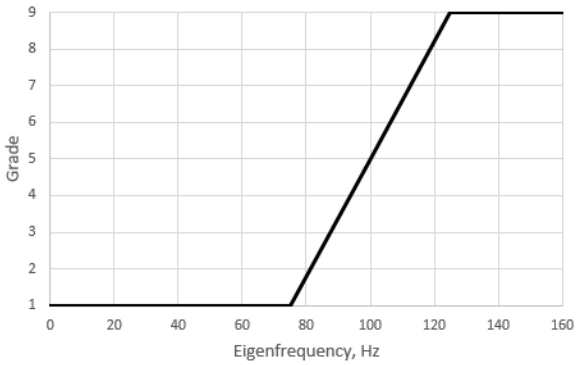

Figure 3.3: *Grading of stowed stiffness criterion (f: stowed eigenfrequency).*

3.3.4. Deployed Stiffness

Deployed stiffness is required for the baffle to have structural integrity and maintain its shape and its relative position to the optical elements of the telescope. Furthermore, higher stiffness is beneficial to avoid vibrations that might result in the satellite losing its pointing stability. Similarly to the stowed stiffness, it is quantified with eigenfrequency. According to requirement BAF-MEC-09-04, the baffle needs to have at least

0.9 Hz eigenfrequency in deployed configuration, but more is favorable.

In Korhonen's thesis it has been concluded that the baffle design could withstand operational structural loads due to reaction wheel vibrations and slew-rate rotations, and it has an eigenfrequency of 0.92 Hz [24]. Therefore, with this eigenfrequency the survival of the baffle is assured, and the requirement goal 0.9 Hz (that originates from the rounding of this eigenfrequency) is graded with a 5. Between 0 Hz and 0.9 Hz the grade increases linearly. Higher eigenfrequencies receive linearly increasing grade until 10 Hz, which received the highest grade. The change of slope in the grading graph (Figure 3.4) is there to be able to reward higher eigenfrequencies while being able to score a relatively good grade with the eigenfrequency goal. To ensure that the satellite doesn't lose its pointing stability because of baffle vibrations further analyses are needed, therefore at this point it cannot be part of the grading.

Deployed eigenfr. range, Hz	Grade
$0 \leq f < 0.9$	$1 + 40/9 \cdot f$
$0.9 \leq f < 10$	$419/91 + 40/91 \cdot f$
$10 \leq f$	9

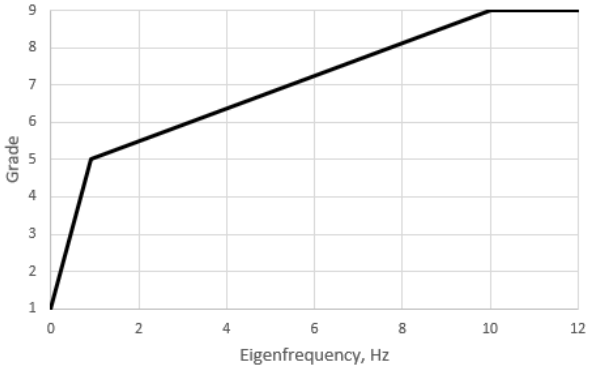

Figure 3.4: *Grading of deployed stiffness criterion (f: deployed eigenfrequency).*

3.3.5. Required Number of Actuators

Each actuator in a spacecraft is a potential point of failure, and therefore it is favorable to choose a deployment mechanism that requires as low number of actuators as possible. For reliability reasons the actuators are often paired with redundant spares, this way if one of them fails, the spare one(s) can take over the task. In the grading of this requirement the spare actuators are ignored, and the absolute minimal number of required actuators are considered. The best achievable number of actuators is one, and it is graded with 9. The grade linearly decreases till four actuators, which scores 1, as illustrated in Figure 3.5.

No. of actuators range, pcs.	Grade
$1 \leq n < 4$	$35/3 - 8/3 \cdot n$
$4 \leq n$	1

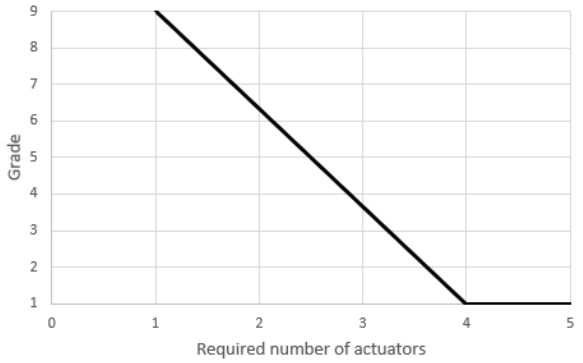

Figure 3.5: *Grading of required number of actuators criterion (n: minimal number of actuators).*

3.3.6. Actuation Method

The space industry prefers passive actuation techniques to active ones for reliability reasons. Active solutions are usually selected only if the requirements cannot be met by passive means, or the active method offers something extra that the passive ones cannot (functionality, control, precision, etc.) [34]. The criterion not only considers if the actuation is passive or active, but gives different grades based on the complexity (considered as reliability) of the solution. The number of actuators are not part of this criterion, as it is a

separate criterion on its own. Actuation method is non-quantifiable, therefore the grading of the alternatives are done by pairwise comparison. Actuation method hasn't been included in the previous theses among the trade-off criteria, however, their criterion Complexity partly covers Actuation method.

3.3.7. Integration Complexity

The baffle consists of two main parts: the frame and the shroud, as mentioned previously. This criterion judges the deployment concept alternatives based on the complexity of the integration of the frame and the shroud, and of the frame and the spacecraft bus. Complexity is assessed based on integration reliability, number of connecting elements, type of connection, and durability, and lower complexity is favorable. Integration complexity is evaluated by pairwise comparison. Complexity has been a criterion for both previous theses, however, integration was not considered in any of them.

3.3.8. Flexibility

Flexibility of the baffle design is required by BAF-SYS-11, and the criterion judges the design based on the ability to easily adjust the design according to late requirement updates [5] as the DST is in constant development. Another aspect of flexibility is how well it can be adapted to the theoretical best design found by stray-light analysis, however, the emphasis is placed on the former aspect. Flexibility is evaluated by pairwise comparison. This criterion has been present only in Arink's thesis, but he only considered the former part.

3.3.9. Reliability

The reliability of the deployment mechanism is controlled by requirement BAF-MEC-02-01, and it combines the reliability of the deployable structure and of the actuation method. The criterion Reliability expands it, and considers the reliability of the baffle assembly, hence including the shroud as well. The baffle is treated as a whole in this criterion, and the failure modes of the baffle assembly of the alternatives are considered, and assessed in pairwise comparisons. Reliability has been considered in previous theses in criterion Complexity.

3.3.10. Baffle Goals Compliance

This criterion assesses the alternatives on how well they comply with the goals of the baffle, i.e., provide stable temperatures, stray-light prevention, and protection against space debris. The baffle shroud, the deployable structure, and the actuators are evaluated together. The three goals have the same weights within this criterion, and while it was considered to assess the compliance of the three goals in three separate criteria, only small differences are expected among the alternatives, which would reduce the utility of multiple criteria. As no detailed design is available when grading the criterion, it is evaluated by pairwise comparisons based on high-level designs.

3.3.11. Discussion

Both Korhonen and Arink included the criterion Complexity in their theses [5, 24], but both of them actually meant reliability behind complexity. In this thesis Reliability, Required number of actuators, and Actuation method are used to describe baffle complexity as they are more specific and evaluable.

Furthermore, Heritage has been also removed from the criteria, although it was used in both previous theses to assess the alternatives on the space heritage of the utilized deployment concepts. The rationale behind it is that although most of the alternatives have been used in space [5, 34], none of them was used to form the frame of a baffle that is deployable in multiple dimensions. Additionally, all alternatives would be custom designed for the DST with limited standard components, making the Heritage criterion irrelevant.

Deployment control was part of Arink's criteria, however, the baffle needs to be deployed only once and with limited deployment requirements (BAF-MEC-02-03-01), and the alternatives are foreseen to have similar grades, therefore deployment control adds little to the trade-off, and it is excluded from the criteria.

In case of ten criteria, it is recommended to group them [21], this way reducing the number of future pairwise comparisons. The ten aforementioned criteria become sub-criteria, and they are grouped under criteria Launch vehicle compatibility, Deployable Structure, Actuation, and Baffle assembly according to Figure 3.6.

3.4. Criteria Weighting

The Analytic Hierarchy Process requires the criteria and sub-criteria to have an order of importance which is realized by weighting. The sub-criteria in a criteria have weights between 0 and 1, and the sum of them equals 1. Similarly, the weight of each criteria is between 0 and 1, and the sum of them equals 1.

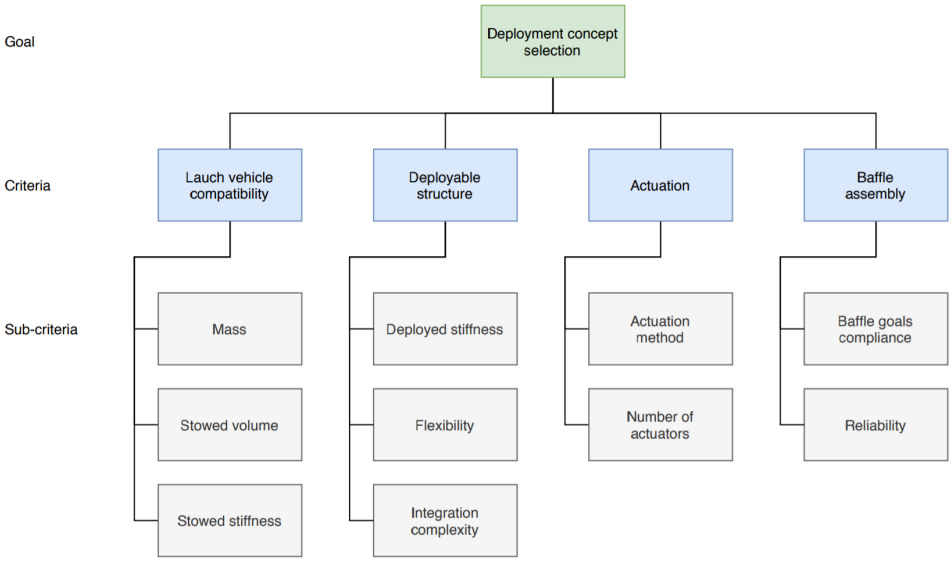

Figure 3.6: *Deployment concept selection criteria and grouping.*

Table 3.2: *Grading of the relative importance of criteria and sub-criteria in pairwise comparisons*

Numerical rating	Verbal judgements
9	Extremely more important or preferred
8	Very strongly to extremely more important or preferred
7	Very strongly more important or preferred
6	Strongly to very strongly more important or preferred
5	Strongly more important or preferred
4	Moderately to strongly more important or preferred
3	Moderately more important or preferred
2	Equally to moderately more important or preferred
1	Equally important or preferred

The weights are decided by pairwise comparisons, in which the relative importance of the criteria and sub-criteria are decided. To reduce the subjectivity of the weighting, six (including the author) project members of DST were asked to fill in a questionnaire, containing $8+6$ pairwise comparisons. The relative importance of the criteria in the pairwise comparisons are graded with numbers between 1 and 9 according to Table 3.2.

An online AHP tool [18] was used to process the input data from pairwise comparisons. The results of pairwise comparisons are shown in Table 3.3, where first the individual weights are presented, followed by the global group weights. The group results are illustrated in Figure 3.7 as well. According to this there is a group of criteria in which all criteria received relatively similar weights (between 8 and 11%), and there are two criteria that have higher - (Baffle goals compliance - 20%, Deployed stiffness - 14%), and two that have lower weights (Number of actuators - 5%, Flexibility - 5%).

Table 3.3 also shows how differently individual group members weighted the criteria. To further analyze this, the group consensuses on different nodes (see Figure 3.6) are presented in Table 3.4. The indicator is derived from the concept of diversity based on Shannon alpha and beta entropy [18]. Only on node Baffle

Table 3.3: *Criteria weighting resulted from pairwise comparisons.*

Participants	Mass	Stowed volume	Stowed stiffness	Deployed stiffness	Flexibility	Integration complexity	Actuation method	Number of actuators	Baffle goals compliance	Reliability
Group member 1	26%	13%	7%	10%	4%	17%	11%	4%	7%	2%
Group member 2	5%	38%	14%	7%	1%	3%	2%	4%	19%	6%
Author	4%	11%	19%	21%	5%	8%	13%	4%	11%	6%
Group member 3	20%	11%	4%	11%	5%	3%	3%	8%	26%	9%
Group member 4	9%	3%	1%	39%	4%	13%	4%	1%	14%	14%
Group member 5	0%	1%	3%	1%	4%	10%	25%	6%	39%	10%
Group result	**9%**	**11%**	**8%**	**14%**	**5%**	**10%**	**9%**	**5%**	**20%**	**8%**

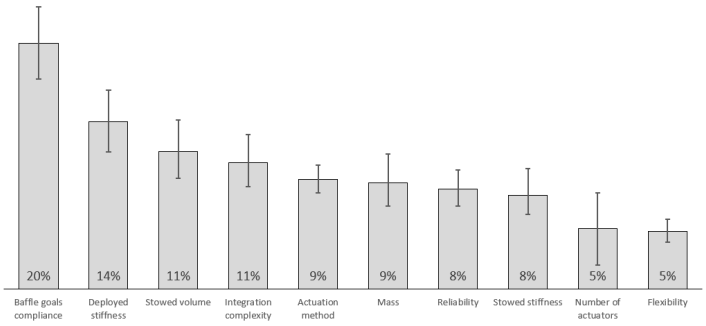

Figure 3.7: *Consolidated global weights in decreasing order, the result of the pairwise comparisons. The error bars show weight uncertainties.*

Table 3.4: *Group consensus on AHP nodes.*

Node	AHP group consensus	
Deployment concept selection	66.0%	(moderate)
Launch vehicle compatibility	51.0%	(low)
Deployable structure	69.9%	(moderate)
Actuation	62.3%	(low)
Baffle assembly	92.8%	(very high)
Global priorities	**68.0%**	**(moderate)**

assembly the group achieved very high consensus, on all the others it is moderate or low. Even on a node that contained only one pairwise comparison (Actuation) the group attained a low consensus that clearly proved the different approaches, backgrounds, and interests of group members. Some of them also included a written explanation to their choices, and these indicate that people tend to make weighting decisions based on their interests and sub-project within the DST project.

The consistency of the individual group members' answers are also checked, see Table 3.5. With the results of the pairwise comparisons arranged in a matrix, the first (dominant) normalized right eigenvector of the matrix gives the weighting, the eigenvalue determines the consistency ratio (CR) [18]. Generally, when the consistency ratio of one's answers is below 10%, they are considered consistent [18]. CRs of nodes Actuation and Baffle assembly are trivially 0% as they consist of only one pairwise comparison. The group members' answers were usually consistent, but Group member 4 had inconsistent answers for nodes Deployment concept selection (CR = 33.1%) and Launch vehicle compatibility (CR = 12.9%).

Figure 3.7 also shows weight uncertainties that are calculated based on a randomised variation of all judgment inputs by +/- 0.5 on the 1 – 9 judgment scale, reduced by the square root of the number of participants [18]. Based on this, the criterion with the highest weight (Baffle goals compliance) is the only one that does not overlap within uncertainties with other criteria. Within uncertainties the following criteria overlap: (1) Deployed stiffness, Stowed volume, Integration complexity; (2) Stowed volume, Integration complexity, Actuation method, Mass, Reliability, Stowed stiffness, Number of actuators; (3) Number of actuators, Flexibility.

With the global criteria weights determined with the help of the DST group, they will be used for the AHP trade-off to find the best alternative for the deployable baffle.

Table 3.5: *Individual group members' consistency check with consistency ratios (CRs).*

	Deployment concept selection	Launch vehicle compatibility	Deployable structure	Actuation	Baffle assembly
Group member 1	3.0%	0.0%	1.9%	0.0%	0.0%
Group member 2	6.0%	0.7%	4.0%	0.0%	0.0%
Author	0.0%	1.9%	1.9%	0.0%	0.0%
Group member 3	0.4%	1.9%	5.6%	0.0%	0.0%
Group member 4	33.1%	12.9%	9.8%	0.0%	0.0%
Group member 5	7.2%	9.0%	5.6%	0.0%	0.0%

3.5. Alternatives

The author mentioned seven options for deployment mechanisms in his literature study [34] that could be used for the baffle of the Deployable Space Telescope. These alternatives included two that have been proposed previously to be used for the DST baffle, see Table 3.6.

Table 3.6: *Deployment mechanism alternatives and their inclusion in previous trade-offs (x: mentioned, o: traded off, o: selected). [34]*

Alternative	Korhonen	Arink
Thin-walled tubular booms	o	
Inflatable structures	o	o
Telescopic structures	o	o
Coilable trusses	o	
Articulated trusses	x	
Tensegrity structures	x	
Pantographic structures		

The number of alternatives can be narrowed down before the trade-off process, as some options are less usable for the DST than others.

3.5.1. Thin-walled Tubular Booms

Thin-walled tubular booms utilize the elastic deformability of thin-walled shells [45]. A well-known example of such device is the steel tape measure, whose cross-section forms an arc of a circle in deployed state, while in stowed configuration it is flattened and rolled up in a small container [34]. A proven example of the thin-walled tubular booms is the Storable Tubular Extendible Member (STEM), depicted in Figure 3.8. STEMs are flat and rolled-up in stowed state, and they can be rolled out to create a tubular masts. There are several iterations of the Single STEM, mainly to increase the torsional stiffness: Bi-STEM that uses two diametrically opposed strips, and Collapsible Tubular Mast (CTM) that utilizes two STEMs that are bonded along the edges (Figure 3.8) [34]. Thin-walled tubular booms can be made of bistable structures, this way it is stable in both deployed and stowed state, making its storing cassette smaller and lighter [34].

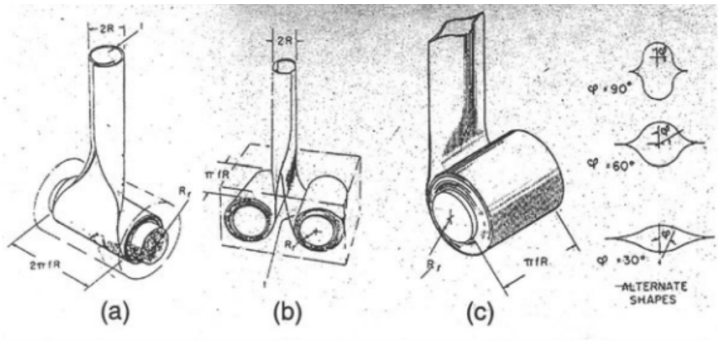

Figure 3.8: *Three types of STEM. (a) Single STEM, (b) Bi-STEM, (c) CTM. [38]*

Thin-walled tubular booms have high deployment ratio, and they are quite stiff axially and in bending, but have low torsional stiffness [45]. However, applying them to form a baffle frame is not practical, as they deploy in only one direction, and many of them would be needed to construct a mechanism that deploys in multiple directions. The actuation of thin-walled tubular booms are usually done by motors, which results in a high number of actuators needed to be used simultaneously. Because it is a high reliability risk, they are omitted from further trade-offs. Yet, STEMs are often used to actuate other deployment mechanisms.

3.5.2. Inflatable Structures

An inflatable structure consist of a flexible skin and pressurized gas that inflates it in deployed configuration. Because of this, inflatable structures have potentially the lowest mass of all deployable structures [34]. The

rigidity of these structures is inherently bad, but there are various techniques to increase it. One of the methods is using aluminium-polymer laminate as foil, and applying enough pressure to reach the yielding stress of the metal in it. Other methods use foils impregnated with resin that later cures at high temperatures or by UV-rays from the Sun [34]. The inflation gas is usually vented after deployment and rigidisation. An example of an inflatable structure is the Inflatable Antenna Experiment (IAE), with 14 m diameter canopy, illustrated in Figure 3.9.

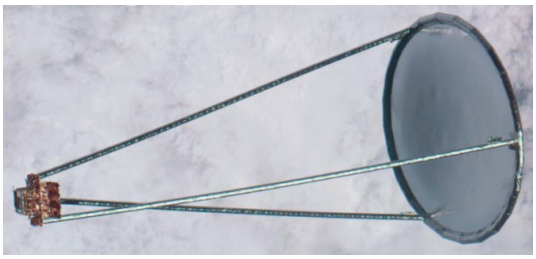

Figure 3.9: *14 m diameter inflatable antenna (IAE). [45]*

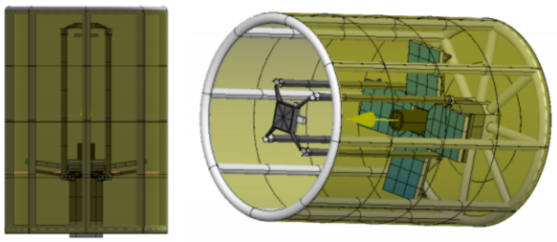

Figure 3.10: *Korhonen's inflatable baffle design for the DST. [24]*

An inflatable baffle was recommended for the DST in Korhonen's thesis [24], depicted in Figure 3.10. Later though, the design was criticized by Arink, who highlighted its lack of stiffness in stowed configuration and its noncompliance with the mass and volume budget [5]. Because of these, inflatable structures are no longer considered a viable alternative for the DST baffle.

3.5.3. Telescopic Structures

Telescopic structures consist of concentric elements that are stacked in each other in stowed configuration. During deployment the concentric elements move along the common axis, reducing the overlaps among the adjacent elements, making the structure longer. To ensure stiffness in the deployed configuration, there must be overlap remaining among the adjacent elements, the more overlap, the higher stiffness [34]. The deployment ratio of the telescopic structures is limited by the diameters, wall thicknesses, and the overlaps of the concentric elements.

Baffles with telescopic deployment can be designed to have the baffle as one telescopic tube consisting of concentric shells, or make the frame of the baffle out of telescopic rods, and attach a shroud to it. The former is an easier and more robust solution, but it allows deployment in only one direction, while mechanisms that deploy in multiple directions can be constructed out of the latter [34]. Arink proposed a deployment system based on telescopic rods in his thesis [5], illustrated in Figure 3.11. He traded off telescopic structures with inflatable ones, which resulted in the telescopic one as the winner [5]. Telescopic baffles represent a feasible choice for the baffle of the DST, and is going to be used in later trade-offs.

3.5.4. Coilable Trusses

Coilable trusses usually consist of three continuous longitudinal elements (longerons) that are braced by perpendicular and diagonal elements (battens and bracing cables, respectively) at regular intervals, see Figure 3.12. The longerons are coiled in stowed configuration, and the deployment can be based on the stored elastic energy of the longerons, while the deployment is controlled by an axial cable attached to the tip of the mast [34]. This deployment solution limits the achievable length of the truss (usually below 3 m [45]) because of the low stiffness of the partially deployed zone. Motor-driven deployment methods usually encapsulate the transition zone within a canister, this way only fully deployed, stiff parts of the structure leave the canister [22].

Although coilable trusses have extensive space heritage, none of the previous applications included multi-directional deployment. To achieve deployment in two directions, a frame should be made out of coilable trusses, similarly to telescopic structures. However, deployment of multiple trusses (many of them need to be deployed synchronously) requires control that would either result in huge number of actuators and canisters that take up valuable space, or deployment without canister but with limited stiffness during deployment. Consequently, coilable trusses are not considered further for the baffle of the Deployable space Telescope.

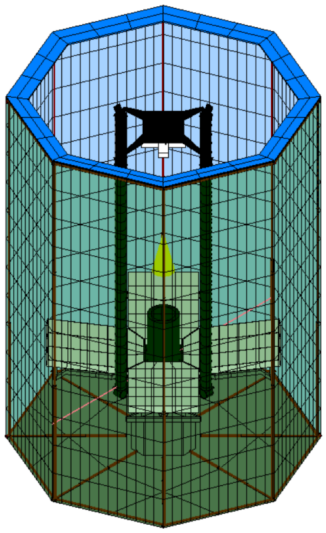

Figure 3.11: *Arink's baffle design. The telescopic structure is depicted in red. [5]*

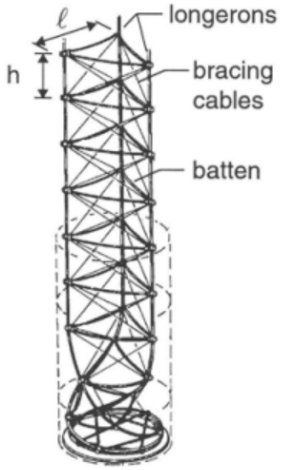

Figure 3.12: *Coilable truss. [38]*

3.5.5. Articulated Trusses

Articulated Trusses have immense space heritage, mostly thanks to their high deployment ratio and stiffness [34]. The Folding Articulated Square Truss (FAST) has four longerons that are interrupted by revolute hinges with axes parallel to the square bays, see Figure 3.13. Every second batten is flexible that facilitates deployment, and the pretensioned diagonal cables ensure stiffness in deployed configuration [34]. The deployment is done sequentially, and every deployed bay has full stiffness [22].

Able Deployable Articulated Mast (ADAM) is an evolution of FAST. In ADAM the battens are rigid, and spherical hinges join the adjacent members of the longerons. The deployment is stopped by latches on the diagonal cables, that are stiffening the bays as well, see Figure 3.14 [45].

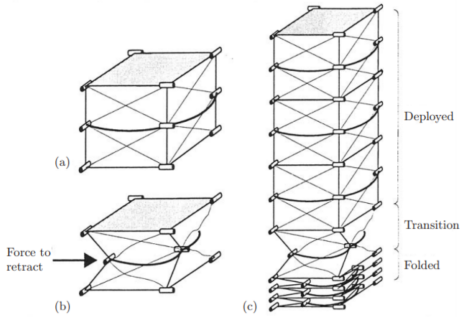

Figure 3.13: *Folding Articulated Square Truss (FAST). [45]*

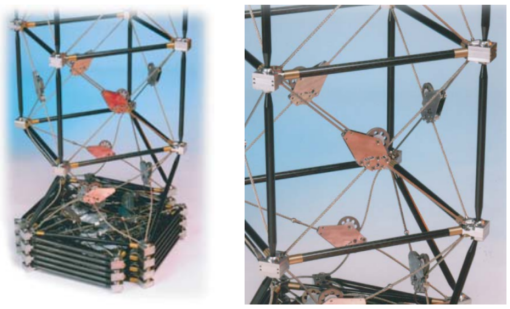

Figure 3.14: *Able Deployable Articulated Mast (ADAM). [45]*

There are several methods to deploy the FAST masts and ADAMs, including canister/nut technique (introduced with the coilable trusses), screw jacks, belt drives, among others [22]. However, all of them require active components that increase complexity and introduce extra mass and volume, and the deployment is in one direction only. Because of these reasons, articulated trusses are omitted from further trade-offs.

3.5.6. Tensegrity Structures

Tensegrity (contraction of tensile integrity) structures – according to one definition – "are based on the use of isolated components in compression inside a net of continuous tension, in such a way that the compressed members (usually bars or struts) do not touch each other and the prestressed tensioned members (usually cables or tendons) delineate the system spatially" [19], see Figure 3.15. Deployable masts can be assembled with elementary tensegrity units placed on each other, and the struts are made to be foldable (for example with a midpoint hinge, as proposed in [45]). According to a proposed design to deploy a tensegrity structure, a canister would enclose the stowed mast, and the deployment would be controlled by an inflatable tube, that

would also stabilize the unstressed mast during deployment [45].

There is potential in tensegrity structures to be applied for the DST, however, a dedicated deployment mechanism is needed to support the whole structure until it is fully deployed, because it lacks rigidity until the last stage is deployed [45]. Based on this, tensegrity structures are not recommended to be considered for the baffle of the DST.

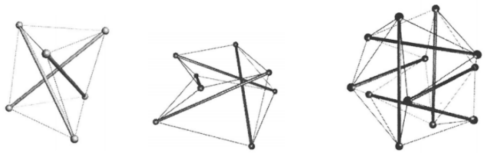

Figure 3.15: *Elementary tensegrity systems. [38]*

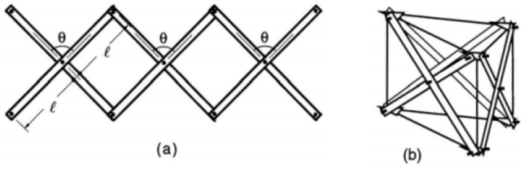

Figure 3.16: *The most basic scissor module. (a) Unfolded, (b) folded with stiffening cables. [38]*

3.5.7. Pantographic Structures

Pantographic structures (often referred as scissor structures/grids/mechanisms) consist of bars crosswise interconnected by revolute joints. This arrangement allows for relative rotation of the connected bars about the axes of the revolute joints, that is perpendicular to the plane containing the pair of bars (unit plane) [42].

Deployable pantographic structures can be designed so that their deployment status only depends on one parameter (θ in Figure 3.16). In this case the entire structure deploys synchronously [38]. It is common to add cables to pantographic structures to increase the deployed stiffness of the structure. These (passive) cables are slack in stowed configuration, and become tout and pretensioned when fully deployed. During deployment the pantograph is the only load bearing structure, whose stiffness is considerably lower [22].

Pantographic structures have space heritage (e.g. deployable radiators on ISS [34]), and it has been proven that structures can be designed based on scissor modules that deploy in multiple directions and synchronously [35]. Synchronously deployable pantographic structures can be theoretically deployed using only one actuator. Because of these unique features pantographic structures are further considered to be an alternative for the deployment mechanism of the DST baffle.

3.5.8. Discussion

Seven alternatives have been presented in this section that could be used for the deployment mechanism of the DST baffle. Out of the seven, two proved to be worthwhile to trade off further, namely the telescopic -, and pantographic structures. The rest had potential problems like deployment in only one direction, need for multiple actuators, sizable deployment tools (e.g. canisters), and while none of them is a key issue on its own, the other two alternatives exceed them in feasibility.

3.6. Pantographic Concept Preliminary Design

The design process is continued with the preliminary design of the alternatives. They are worked out with the required depth to be able to be graded for the criteria. The pantographic concept is a new one, while the telescopic one uses Arink's final design with some required modifications so it could be compared with the pantographic concept.

The goal of the preliminary design chapters is twofold: the ultimate objective remains to find the best concept for the Deploayable Space Telescope and design it to comply with the requirements, however, to be able to compare the two concepts some design choices might not be in favor for the first goal, but rather are made to make the comparison achievable. Such choices are explained in the text, and are revisited later in the detailed design phase. As the telescopic design has already been prepared by Arink [5], most of the design choices made while working on the pantographic concept are to ensure comparability.

3.6.1. Principles

Unit lines in pantographic structures can be defined as the imaginary lines running through the upper and lower end point at both sides of the unit [42]. Based on how these line vary during deployment, three types of scissor units can be distinguished, see Figure 3.17. Scissor units that consist of straight bars and have parallel unit lines are called translational units. Polar scissor units involve straight bars as well, but have intersecting

unit lines. Angulated (or articulated) units incorporate kinked bars and have intersecting unit lines, however, angulated units maintain the same angle between unit lines throughout the deployment, while polar units do not.

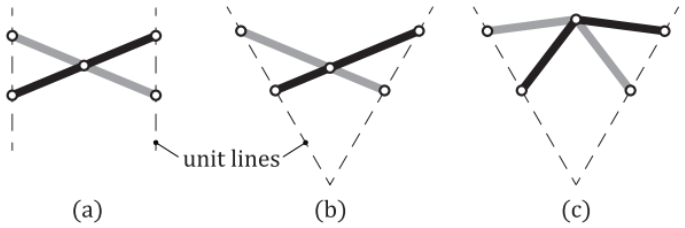

Figure 3.17: *(a) Translational, (b) polar, (c) angulated scissor units. [42]*

When scissor units are combined to form single closed loops, scissor modules are created. Multiple scissor modules form scissor grids. In other words, scissor grids are made by interconnecting multiple scissor units at their end points [42].

According to Hoberman's discovery, angulated scissor units can be used for radial deployment while maintaining the original shape, see Figure 3.18. Based on this geometry several structures have been designed, including retractable roofs, deployable arches, but probably the most famous one is the Hoberman sphere (Figure 3.19) [2].

Figure 3.18: *An expanding hexagon consisting of angulated scissor units. [2]*

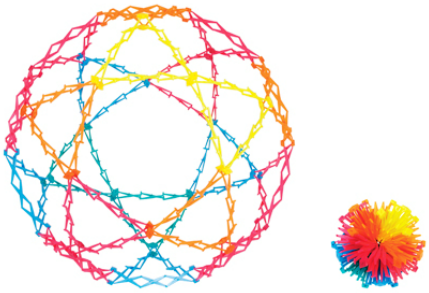

Figure 3.19: *Hoberman sphere in deployed (left) and undeployed (right) state. Courtesy of Hoberman Associates.*

To achieve the iconic behavior of the angulated units in Hoberman's designs, the angle in an arm is prescribed as [2]:

$$\angle HIG = \pi - \frac{2\pi}{N} \tag{3.1}$$

where N is the number of edges in an equilateral polygon, see Figure 3.20.

There are other solutions to achieve radial deployment. An example is the Cable-Stiffened Pantographic Deployable Antenna (CSPDA). The CSPDA is a deployable ring-like pantograph that consists of three different pairs of rods, connected by scissor joints, illustrated in Figure 3.21. The deployed diameter of the structure is 3.5 m, while the stowed configuration have the diameter of 0.6 m and length of 1.2 m [45]. CSPDA incorporates cables to increase the deployed stiffness. In CSPDA the radial deployment is facilitated by a clever geometrical design consisting of only translational scissor units. Compared to Hoberman's solution CSPDA is more complex, and utilizes 3D deployment instead of being limited to a plane.

3.6.2. Previous Experiences

A cylindrical prototype based on pantographic elements has been developed that can be deployed in multiple dimensions synchronously [35], illustrated in Figure 3.24. It was a proof of concept as it was designed with the deployable baffle for the DST in mind, but was neither optimized for deployment ratio, number of parts, etc., nor it had the right proportions.

The structure of the prototype consisted of scissor grids that were made up of straight and angulated units. The radial and axial deployment of the cylinder were separated as they acted on different grids, see Figure 3.22, however their integration was solved in a way so that the deployment of one triggers the deployment

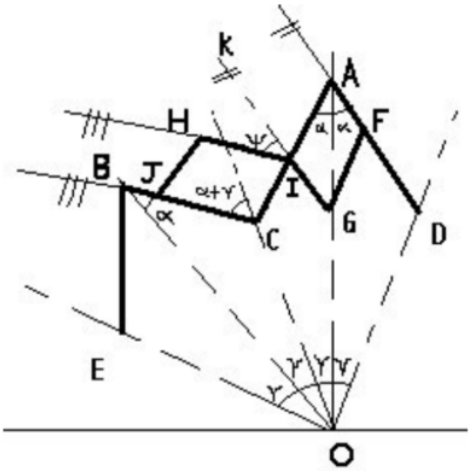

Figure 3.20: *Relationship between angles in a Hoberman N-gon. [2]*

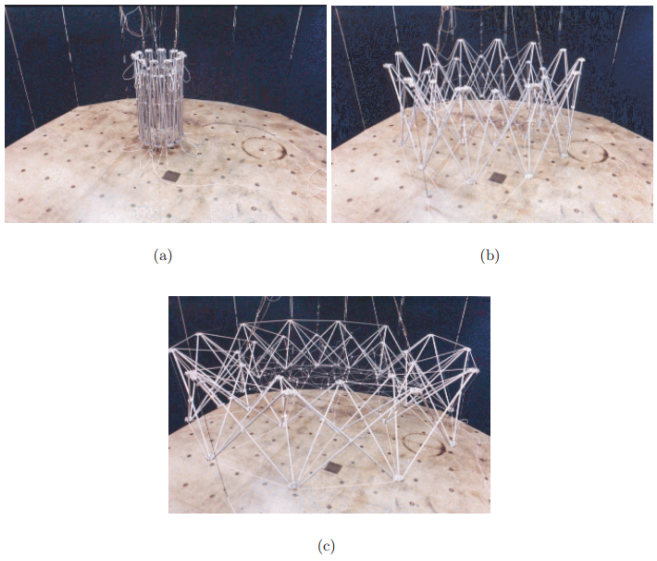

Figure 3.21: *Deployment sequence of the Cable-Stiffened Pantographic Deployable Antenna (CSPDA). [45]*

of the other as well (Figure 3.24). These connections between the radial and axial grids allow for synchronous deployment in both directions.

The fasteners within the pantographic units were machine screws and locknuts that were placed in holes big enough to support revolute motion. The joints between the radial and axial grids were simple elements that connected to the grids the same way as described in the previous sentence, see Figure 3.23.

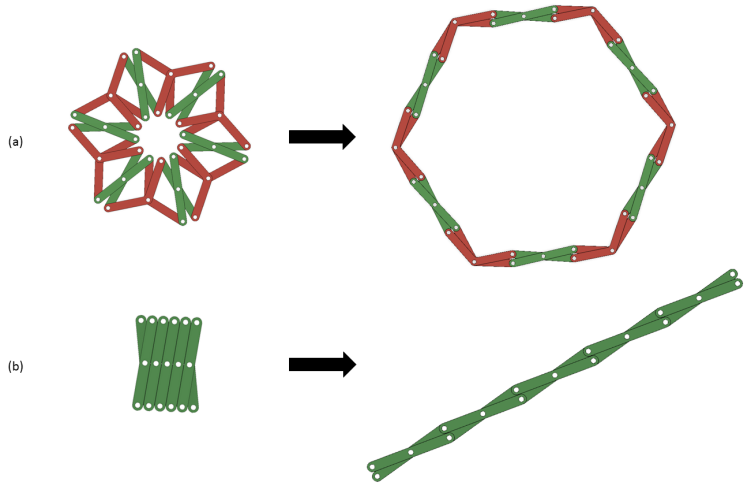

Figure 3.22: *Pantographic grids responsible for (a) radial and (b) axial deployment. Straight units are depicted with green, angulated ones are with red color. [35]*

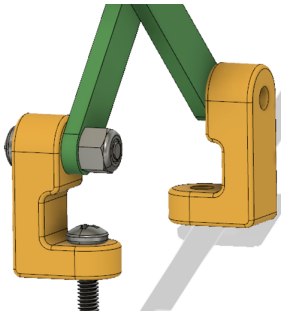

Figure 3.23: *Joints (in yellow). The radial grid and some fasteners are not depicted. [35]*

The grids responsible for radial deployment consisted of both straight and angulated units. In theory the angulated units only would have been enough to facilitate radial deployment, as seen in Hoberman sphere [2], however, using only angulated units would have limited the design options to:

1. Changing the number of edges in the equilateral polygon the radial grid describes. With the number of edges changing, the angle of the angulated units changes in a prescribed manner according to Equation (3.1).
2. Changing the arm length of the angulated units. In this case the proportions of the radial grid (including deployment ratio) remain the same, but the size of grid changes.

However, with straight units added between the angulated units, the design options expand to:

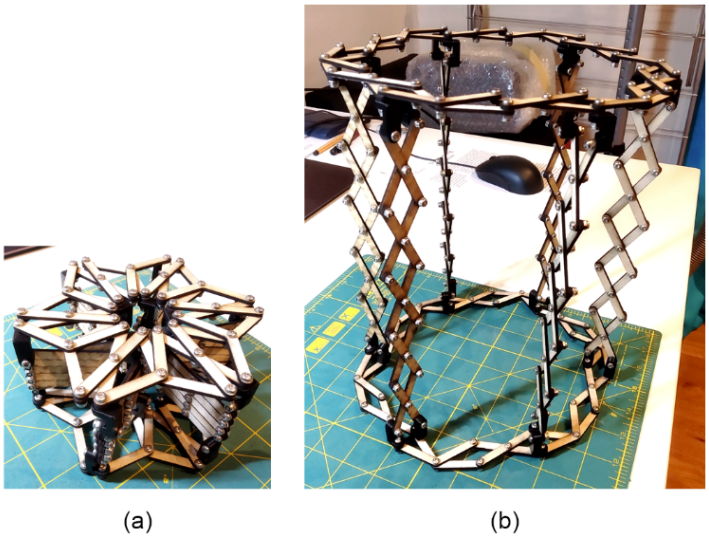

Figure 3.24: *Prototype of a synchronously deployable cylinder in (a) stowed, (b) deployed state. [35]*

1. Changing the number of edges in the equilateral polygon the radial grid describes. With the number of edges changing, the angle of the angulated units changes in a prescribed manner according to Equation (3.1).
2. Changing the arm length of the angulated units.
3. Changing the arm length of the straight units.
4. Changing the number of straight units between the angulated ones.

With the extended range of design freedom the deployment ratio can be customized according to one's requirements, an opportunity that the grids consisting of only angulated units lacked.

The prototype succeeded as a proof of concept, it proved that a cylindrical baffle that deploys synchronously in multiple dimensions can be created out of scissor units. Additionally, it also provided insights on improvement possibilities: the tolerances between holes and screws (or other fastener that allows rotational movement) should be minimized. In the prototype Ø3 mm holes were lasercut in the arms for M2.5 screws. The tolerance allowed for easy rotation, but also for distorted geometries with the grids fully extended, see Figure 3.25. Another solution for reducing the undesired play in the grids is to limit their deployment [35].

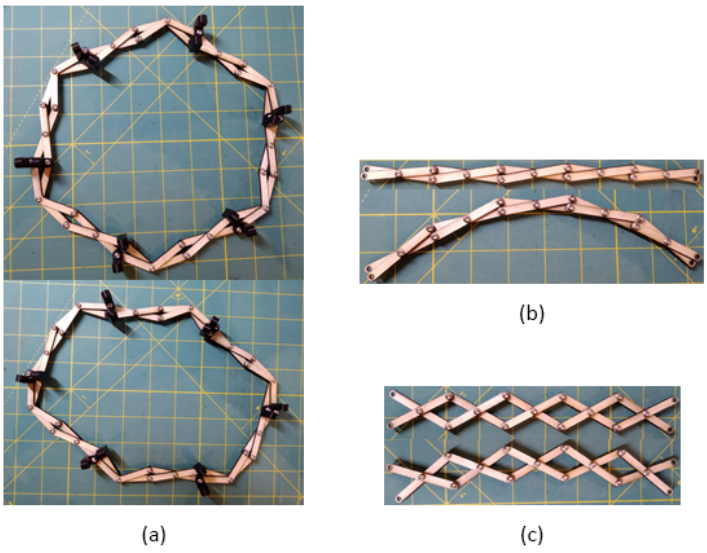

Figure 3.25: *Distorted geometries in pantographic structures in (a) radial and (b) axial grids. Limiting the maximal deployment of the grids reduces the undesired play (c). The designed geometries are the top photos, while the worst geometries are the bottom ones. [35]*

Table 3.7: *Basic comparison of the pantographic prototype and Arink's telescopic concept.[5, 35]*

	Pantographic prototype	**Arink's telescopic concept**
Shape	hexagonal prism	octagonal prism
Inner stowed diameter, mm	27	977.9
Outer stowed diameter, mm	135	1084.9
Inner deployed diameter, mm	175	1847.8
Outer deployed diameter, mm	220	2025.1
Stowed height, mm	86	933.1
Deployed height, mm	268	2746.2

Required changes

The prototype that has been introduced in the previous section forms the base of the updated pantographic design that is to be traded off with the telescopic alternative. Arink's design has some fundamental differences compared to the pantographic prototype, they are listed in Table 3.7. The shape of pantographic prototype is a hexagonal prism, while the shape of Arink's design is an octagonal prism. Both shapes are cylinders with polygonized bases with different levels of polygonization that facilitate an easier deployment by consisting of only straight sides. In the previous theses Korhonen and Arink traded off different baffle shapes in order to find the most suitable one, and from mechanical and thermal point of view the octagonal prism turned out to be the best alternative [5, 24]. The trade-off criteria included mass, stiffness, reliability (number of booms) [24], and thermal performance [5]. Their trade-off is accepted, and the shape of the baffle is changed to octagonal prism.

Furthermore, the proportions of the prototype are not suitable for the Deployable Space Telescope, therefore they need to be modified as well. The required dimensions and proportions are given as a set of geometrical constraints.

3.6.3. Constraints on the Radial Module

The spacecraft bus, the telescope components, and the requirements constrain the dimensions of the radial pantographic module both is stowed and deployed configuration. These constraints are:

1. The inner stowed diameter must be big enough so that the spacecraft bus and optical components would fit inside. These fit in a circle of diameter of 932 mm, so $D_{in}^{st} \geq 932$ mm (hard constraint);

2. In order to limit the stowed volume of the baffle, the radial size of the stowed baffle should not be greater than 1 m (diameter). This constraint originates from Arink [5], but with minimizing the axial size of the baffle the volume requirement goal of 0.75 m^3 can be achieved with greater than 1 m stowed outer diameter. Nevertheless, the constraint shows that the outer stowed diameter should be minimized, and $D_{out}^{st} \leq 1000$ mm (soft constraint);

3. In deployed configuration the internal diameter of the baffle shall be big enough to accommodate the spacecraft bus and the telescope components, and additionally it shall have 100 mm of clearance from all telescope components (requirement BAF-MEC-02-03-02). The diameter of the circumscribed circle around the deployed M1 segments is $\sqrt{1506.53^2 + 450^2} = 1572.3$ mm [5], consequently the inner deployed diameter of the baffle shall be at least 1773 mm: $D_{in}^{dep} \geq 1773$ mm (hard requirement);

4. For the outer deployed diameter there is no constraint, however, it is beneficial to keep it minimal as the atmospheric drag and the MMOI (that is important for the ADCS) increase with increasing outer diameter.

The constraints are visualized in Figure 3.26.

3.6.4. Geometrical Relationships in the Radial Module

In this section the geometrical relationships of an octagonal pantographic radial module consisting of 8 angulated - and $8n$ straight units ($n \geq 0$) are analyzed.

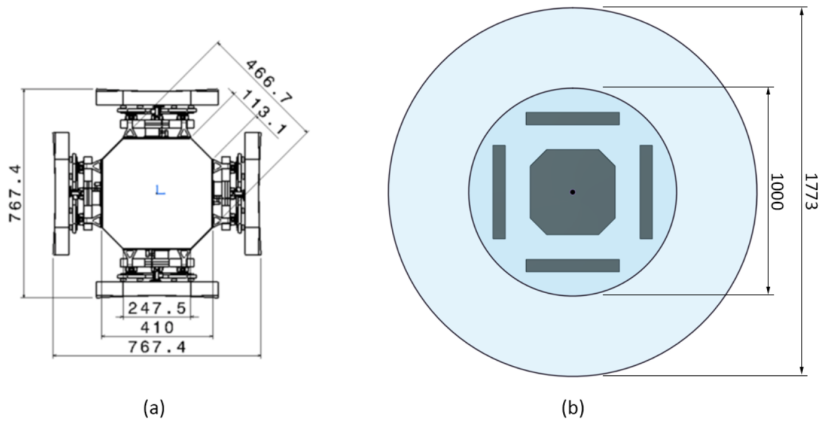

Figure 3.26: *Available space for the baffle. (a) Dimensions of the S/C bus and telescope components [5], (b) Maximal outer stowed diameter (1000 mm), and minimal inner deployed diameter (1773 mm). The perimeters of the M1 segments represent the minimal inner stowed diameter of 932 mm.*

Optimal Straight Arm Length

If the straight arm length l (Figure 3.27) is greater than the optimal straight arm length l_{opt}, the angulated units reach their stowed configuration while the straight arms are still semi-deployed, increasing the stowed diameter of the module. If $l < l_{opt}$ the straight arms reach their stowed configuration first with the angulated arms still being semi-deployed. An example of this is illustrated in Figure 3.28b. With optimal arm ratio both the straight and angulated units reach their stowed (and deployed) configuration at the same time (see Figure 3.28a), making the stowed diameter (both internal and external) minimal for a given angulated arm length L.

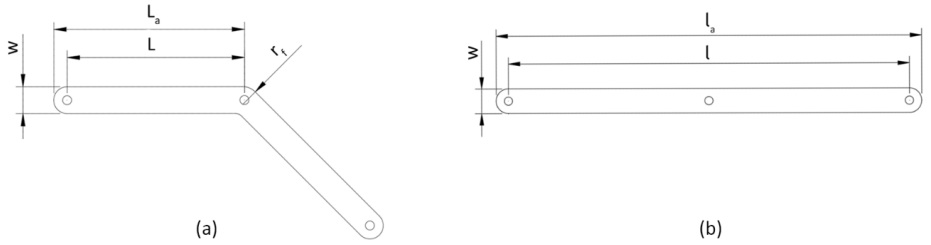

Figure 3.27: *Dimensions of the (a) angulated and (b) straight arms.*

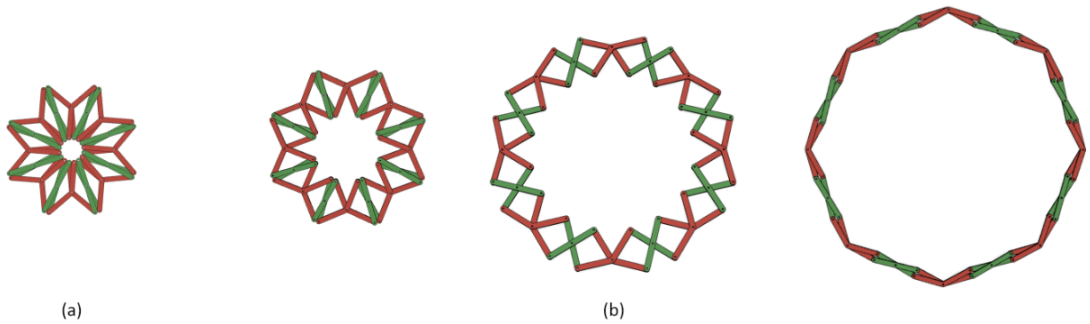

Figure 3.28: *Deployment of an octagonal scissor module consisting of one straight unit between angulated units. (a) Stowed configuration with optimal arm ratio. (b) Stowed, semi-deployed, and deployed configuration with arbitrary arm ratio.*

In order to find the relationship between L and the optimal l, the stowed configuration of such a structure (Figure 3.28a) with $n = 1$ is analyzed. The internal rotation points of the module describe a 16-gon, with the arm width w being the side length of the polygon, see Figure 3.29. The optimal straight arm length $l_{opt}(= l)$ as a function of w and L:

$$l_{opt} = \sqrt{w^2 + y^2} = \sqrt{w^2 + \left(w\cos(5\pi/8) + \sqrt{L_d^2 - w^2\sin^2(5\pi/8)}\right)^2}$$
$$l_{opt} = \sqrt{w^2 + \left(w\cos(5\pi/8) + \sqrt{(2+\sqrt{2})L^2 - w^2\sin^2(5\pi/8)}\right)^2} \tag{3.2}$$

which means l_{opt} is linearly dependent on L. Further analyses proved that the optimal arm ratio l_{opt}/L is the same for all angulated arm lengths, and it does not change with increasing number of straight units between angulated units. From now on the straight arm length is the optimal straight arm length ($l = l_{opt}$), unless specified otherwise.

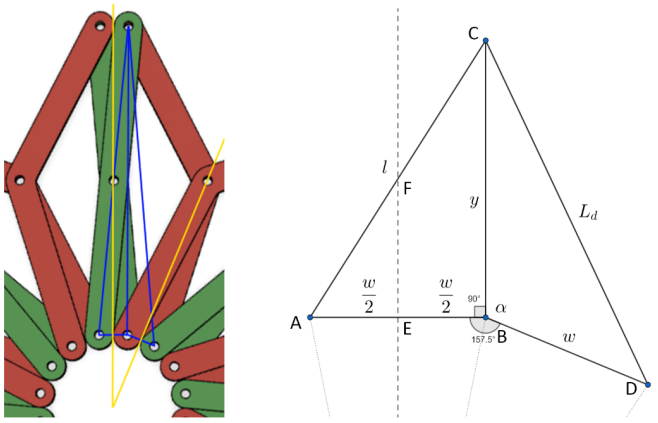

Figure 3.29: *Relationship between the angulated and optimal straight arm lengths. (a) Blue: the studied triangles, yellow: some of the mirror lines in the module. (b) Detailed drawing of the blue triangles from (a) with solid lines, and mirror lines as dashed lines.*

Inner Stowed Diameter

Based on geometrical considerations, the inner stowed diameter of an octagonal radial structure based on 8 angulated and $8n$ straight units with optimal arm ratio is:

$$D_{in}^{st} = 2r - w = \left[\frac{\left(1+\sqrt{2}\right)\left(\sqrt{2+\sqrt{2}}n+2\right)}{\sqrt{2+\sqrt{2}}} - 1\right] w \tag{3.3}$$

where $r = \left(1+\sqrt{2}\right)\left(\sqrt{2+\sqrt{2}}n+2\right) w/\left(2\sqrt{2+\sqrt{2}}\right)$ is the radius of the inscribed circle of an octagon described by the inner rotational points of the radial module with optimal arm ratio, see Figure 3.30. According to this, the inner stowed diameter only depends on the number of straight units between angulated units n and the arm width w. Equation (3.3) gives an exact result when n is even, and results in a close approximation when n is odd (the difference of the internal stowed radius and the aforementioned inscribed circle radius is not exactly $w/2$ in that case), but the difference is negligible with as long arms as the ones are considered, and for simplicity the two cases are not distinguished.

Outer Stowed Diameter

The outer stowed diameter of the octagonal radial structure is:

$$D_{out}^{st} = 2R + w = 2\sqrt{\left(r + \sqrt{l^2 - w^2}\right)^2 + \left(\frac{n}{2}w\right)^2} + w \tag{3.4}$$

where $R = \sqrt{\left(r + \sqrt{l^2 - w^2}\right)^2 + (nw/2)^2}$ is half of the greatest distance between any rotational points (diagonal) in stowed configuration, L is the angulated arm working length, l is the optimal straight arm working length (dependent on w and L, see Equation (3.2)), and r was introduced at the inner stowed diameter calculation. This also means that the outer stowed diameter is dependent on all the variables (w, n, L) that describes the radial module.

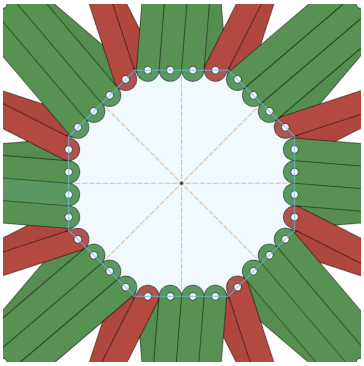

Figure 3.30: *The octagon described by the inner rotational points of the radial module with optimal arm ratio.*

Inner Deployed Diameter

The inner deployed diameter of the octagonal radial structure is:

$$D_{in}^{dep} = 2R_{in} - 2w = \left(1+\sqrt{2}\right)\left(2\sqrt{L^2 - \frac{w^2}{4}} + n\sqrt{l^2 - w^2}\right) - 2w \tag{3.5}$$

where $R_{in} = \left(1+\sqrt{2}\right)\left(2\sqrt{L^2 - w^2/4} + n\sqrt{l^2 - w^2}\right)$ is the radius of the inscribed circle of an octagon described by the middle rotational points of the angulated arms.

Outer Deployed Diameter

The outer deployed diameter of the octagonal radial structure is:

$$D_{out}^{dep} = 2R_{out} + 2b = \frac{2}{\sqrt{2-\sqrt{2}}}\left(2\sqrt{L^2 - \frac{w^2}{4}} + n\sqrt{l^2 - w^2}\right) + 2b \tag{3.6}$$

where $R_{out} = 1/\left(\sqrt{2-\sqrt{2}}\right)\left(2\sqrt{L^2 - w^2/4} + n\sqrt{l^2 - w^2}\right)$ is half of the biggest distance of any rotational points in deployed configuration (basically the circumradius of the octagon), and $b = r_f - \sqrt{2(2-\sqrt{2})}\left(r_f - w/2\right)$ is the rotational point - middle fillet distance in the angulated arm, with r_f being the fillet radius. Similarly to the outer stowed - and inner deployed diameter, the outer deployed diameter depends on all the variables (w, n, L) that describes the radial module.

Inner Diameter - Deployment Angle

To describe the inner and outer diameters of a radial module consisting of 8 angulated and n straight units between them with optimal arm ratio at any point of the deployment process, the inner and outer diameter - deployment angle relationships are derived. The inner diameter as a function of the deployment angle θ, angulated arm length L, optimal straight arm length l, arm width w, and n:

$$D_{in}(\theta) = d - w = \left(1+\sqrt{2}\right)\left(\sqrt{2(2-\sqrt{2})}\cdot 2L\sin\frac{\theta}{2} + nl\sqrt{1 - \frac{4L^2\cos^2\left(\frac{\theta}{2}+\frac{\pi}{8}\right)}{l^2}}\right) - w \tag{3.7}$$

where d is the diameter of the inscribed circle of an octagon described by the inner rotational points of the radial module. The deployment angle θ is the angle between two angulated arms as illustrated in Figure 3.31. The angle between the straight arms λ can be expressed as a function of θ:

$$\lambda = 2\cos^{-1}(2L/l \cdot \cos(\theta/2 + \pi/8)) \tag{3.8}$$

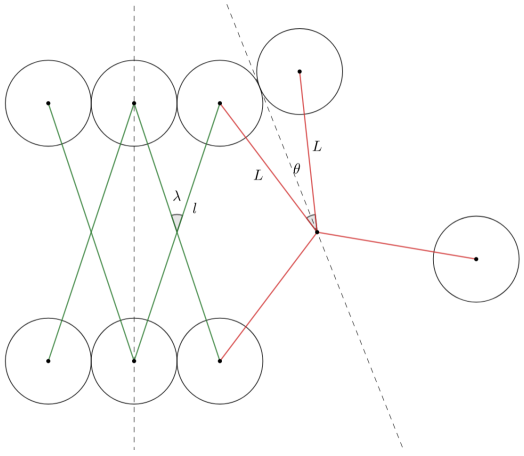

Figure 3.31: *The repeating part of an octagonal radial module with n = 2 in stowed configuration. The deployment angle θ is between the angulated units (red), while the deployment status of the straight units (green) is described by angle λ.*

Outer Diameter - Deployment Angle

In case of the outer diameter at a certain deployment angle the parts that describe the maximal diameter change, thus two outer diameters need to be defined, and at every deployment angle the higher of them needs to be considered. The outer diameter $D_{1,out}(\theta)$ is described by the opposite outer rotational points between an angulated and a straight arm (e.g. Figure 3.28b, middle):

$$D_{1,out}(\theta) = 2\sqrt{\left(\frac{d}{2} + 2L\sin\frac{3\pi/4-\theta}{2}\right)^2 + \left(n\sqrt{\left(\frac{l}{2}\right)^2 - \left(L\sin\frac{3\pi/4-\theta}{2}\right)^2}\right)^2} + w \tag{3.9}$$

while the outer diameter $D_{2,out}(\theta)$ is described by the middle rotational points of opposite angulated arms (e.g. Figure 3.28b, right):

$$D_{2,out}(\theta) = \frac{2}{\sqrt{2-\sqrt{2}}}\left(2n\sqrt{\left(\frac{l}{2}\right)^2 - \left(L\sin\frac{3\pi/4-\theta}{2}\right)^2} + 2L\cos\frac{3\pi/4-\theta}{2}\right) + 2b \tag{3.10}$$

where the first part (without $+2b$) is the diameter of the circumscribed circle of the octagon described by the middle rotational points of the angulated units, and b is the same as in Equation (3.6).

Deployment Angle Extreme Values

In stowed configuration the deployment angle θ has its minimal value:

$$\theta_{min} = 2\sin^{-1}\frac{w}{2L} \tag{3.11}$$

In deployed configuration θ reaches its maximal value:

$$\theta_{max} = \frac{3\pi}{4} - \theta_{min} = \frac{3\pi}{4} - 2\sin^{-1}\frac{w}{2L} \tag{3.12}$$

The minimal and maximal λ angles can be calculated from the extreme values of θ with Equation (3.8). The verification of the presented Equations (3.3) to (3.12) were done using 3D models and measurements, and some of them can be cross-checked with each other.

3.6.5. Radial Design Optimization

In this section the constraints introduced in Section 3.6.3 are compared against the geometrical relationships presented in Section 3.6.4.

Inner Deployed Diameter

The third constraint states that in deployed configuration the internal diameter of the baffle shall be big enough to accommodate the spacecraft bus and the telescope components, and additionally it shall have 100 mm of clearance from all telescope components: $D_{in}^{dep} \geq 1773$ mm, and it is a hard requirement. Using Equation (3.5) the minimal angulated arm lengths L are calculated for each number of straight units n to reach $D_{in}^{dep} = 1773$ mm. The resulting diameters (with arm width $w = 15$ mm) are presented in Figure 3.32 as a function of n. For any n an angulated arm length L can be found that would allow the deployed M1 (plus clearances) to fit inside the deployed baffle. The depicted solutions are the ones with minimal arm lengths so that no more mass and volume are added to the structure than what is absolutely necessary.

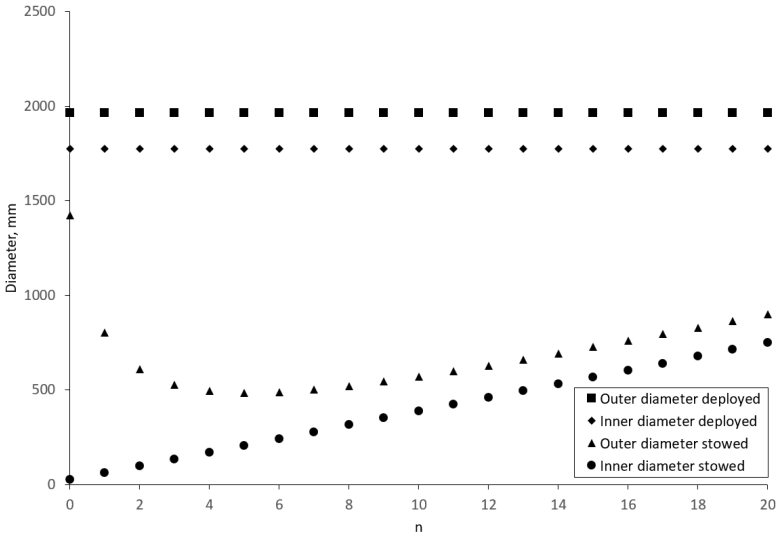

Figure 3.32: *Diameters of an octagonal pantographic structure using n straight units between angulated ones. The angulated unit lengths are chosen so that the inner deployed diameter reaches 1773 mm. $w = 15$ mm.*

Inner Stowed Diameter

The first constraint requires the inner stowed diameter to be big enough so that the spacecraft bus and optical components would fit inside: $D_{in}^{st} \geq 932$ mm, which, again, is a hard constraint. According to Figure 3.32 the inner stowed diameter linearly increases with the number of straight units n, however, not even an octagonal structure with $n = 20$ complies with the constraint. At least $n = 26$ straight units are required between the angulated ones (with $w = 15$ mm) to have an inner stowed diameter of 932 mm (derived with Equation (3.3)), which is impractical because of increased complexity and mass (including interfaces).

The options are not limited to $n \geq 26$ though. The stowed configuration of the baffle does not have to be the minimum stowed size of the pantographic structure: any angle between the minimal and maximal deployment angle can be chosen as the start configuration. Starting with the results of Figure 3.32, a deployment angle θ is selected for each n using Equation (3.7) so that the inner diameter would reach 932 mm, and this angle represents the new stowed configuration of the radial pantographic module. The results are visualized in Figure 3.33. The figure also portrays the diameters of the octagonal structure with optimal (for constraint 1 and 3) arm lengths and deployment angle in stowed configuration for each n. The depicted solutions comply with all hard constraints.

Outer Stowed Diameter

Constraint 2 aims to keep the outer stowed diameter D_{out}^{st} below 1000 mm to limit the stowed volume of the baffle, and it is a soft constraint. However, even with zero radial thickness such a baffle cannot be created. The ratio between the radii of the circumscribed and inscribed circles of an octagon is the minimal ratio that the outer and inner diameters of an octagonal pantographic module can have, see Figure 3.34. This minimal ratio is $R/r = \sqrt{4-2\sqrt{2}} \approx 1.0824$, which means that 932 mm of inner diameter forbids less than 1008.8 mm outer diameter of the pantographic structure even with zero radial thickness. This means that constraint 2 is not achievable due to constraint 1, however, one can aim to minimize the outer stowed diameter to get as close to the goal of constraint 2 (1000 mm) as possible.

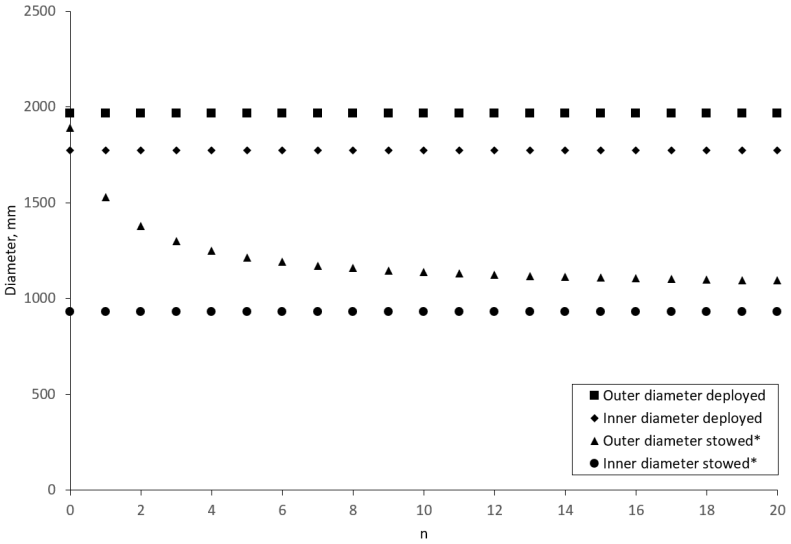

Figure 3.33: *Diameters of an octagonal pantographic structure using n straight units between angulated ones. The angulated unit lengths are chosen so that the inner deployed diameter reaches 1773 mm. The stowed deployment angle is selected so that the inner stowed diameter is 932 mm. $w = 15$ mm. The asterisk highlights that the stowed diameters are different than previously were.*

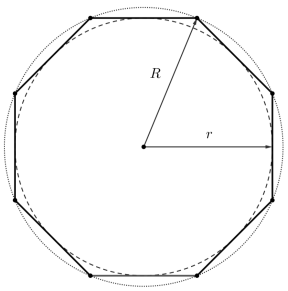

Figure 3.34: *Inscribed and circumscribed circles of an octagon with their radii r and R, respectively.*

The solutions that comply with all the hard requirements (Figure 3.33) differ in outer stowed diameter, but their other three diameters are the same. The outer stowed diameter is monotonically decreasing with increasing n, so if only this metric is considered, as high number of straight units n as possible is desirable to approach the diameter in constraint 2. However, with increasing n the complexity and mass of the radial structure increase as well, both of which shall be minimized.

Arm Width

In the previous calculations the arm width w was kept constant at 15 mm. The earlier calculations of Section 3.6.5 have been repeated with changing w, and the results are presented in Figure 3.35, which shows that the effect of changing the arm width is minimal to the outer stowed diameter, on the other hand, it is significant on the mass of the arms. Consequently, modifying the arm width w is a great tool to customize the mass of the structure with minimal effect on the diameters of the module. However, decreasing w reduces the strength of the structure, so it needs to be applied with care. At this point no further data is available to help choosing the optimal arm width, so it is kept at $w = 15$ mm for now, but it might be revisited in a later stage of the design.

Number of Straight Arm

The number of arms, interfaces (i.e. connections among arms), and the relative mass of the arms for the solutions are presented in Table 3.8. The mass of the arms slightly increases with increasing n, but the number (and consequently the mass) of the interfaces increase drastically. To find the optimal straight arm number n two conflicting metrics are to be assessed: (1) to minimize the of outer stowed diameter n should be as great as possible, and (2) to minimize the mass and complexity (evaluated as the number of interfaces) n should be minimized. There is no unequivocal solution for this optimization problem, therefore the solution contains subjective judgement. Based on the available data $n = 3$ is selected, as it already decreases the outer stowed diameter significantly (by 31.3% compared to $n = 0$), yet it keeps the number of interfaces and mass of the arms at a relatively low level.

Further Optimization

Constraint 2 minimizes the inner stowed diameter of the baffle at 932 mm, as this is the diameter of the circumscribed circle of the stowed M1. However, with an octagonal baffle structure the octagonal perimeters of the M1 can be further approached, which means that the inner stowed diameter can be decreased. The greatest distance of the sides of the octagon that the M1 segments describe is 860.8 mm, so a calculation is made to minimise the inner stowed diameter at 861 mm. The comparison between the octagonal structure design

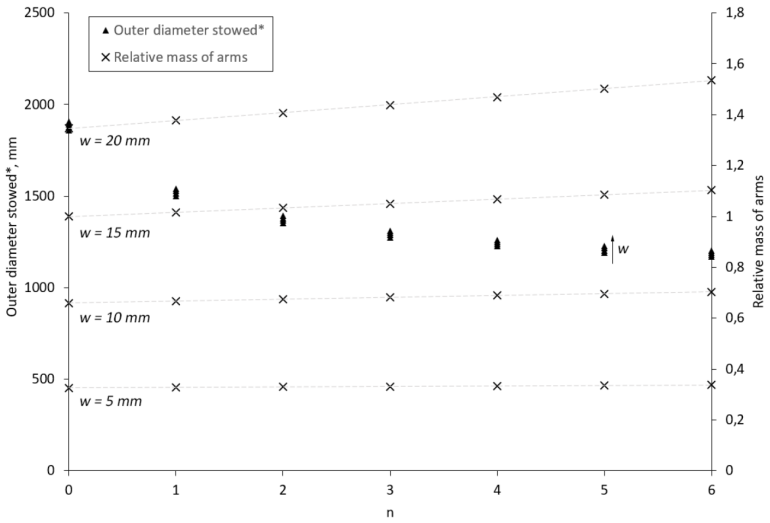

Figure 3.35: *Outer stowed diameter and mass of the octagonal module as a function of number of straight arms n and arm width w. The base of the relative mass calculation is $n = 0$, $w = 15$ mm. The angulated unit lengths are chosen so that the inner deployed diameter reaches 1773 mm. The stowed deployment angle is selected so that the inner stowed diameter is 932 mm.*

Table 3.8: *Number of arms and interfaces, and the relative mass of arms in case of different straight arm numbers n. The base of the relative mass calculation is $n = 0$, and only the mass of the arms are considered, others (e.g. mass of the interfaces) are not. Derived from the solutions of Figure 3.33.*

n	No. of arms	No. of interfaces	Relative mass of arms
0	16	24	1.00
1	32	48	1.02
2	48	72	1.03
3	64	96	1.05
4	80	120	1.07
5	96	144	1.08
6	112	168	1.10
7	128	192	1.12
8	144	216	1.14
9	160	240	1.16
10	176	264	1.18

with inner stowed diameter of 932 mm (the one selected in the previous subsection) is shown in Table 3.9. Changing the inner stowed diameter does not have an effect on the inner and outer deployed diameters, n, w, and arm lengths, as they were optimized before the inner stowed diameter. What do change though are the stowed deployment angle θ and the outer stowed diameter, and reducing the D_{out}^{st} is the real gain of decreasing the inner stowed diameter, as D_{out}^{st} further approaches the goal 1000 mm. The distance between the stowed baffle and M1 segments are negligible according to this design as no requirement prescribes this distance, but it might need to be revisited in detailed design stage.

The octagonal radial pantographic module has been optimized to comply with all the hard requirements, and to best approach the soft requirement. The properties of this design are summarized in Table 3.9 in bold, and it is illustrated in its stowed configuration in Figure 3.36.

3.6.6. Constraints on the Axial Module

The constraints for the axial modules are:

1. Previous studies showed that the stowed instrument can survive without the protection of the baffle, so no constraint is imposed on the minimal stowed height of the baffle.

2. The maximal stowed height of the baffle should be small enough so that the stowed baffle would fit into

Table 3.9: *Comparison of the properties of the octagonal modules with 932 mm and 861 mm inner stowed diameter.*

Inner diameter stowed*, mm	932	**861**
n	3	**3**
w, mm	15	**15**
L, mm	101.6	**101.6**
l, mm	182.0	**182.0**
Stowed θ, degree	41.0	**36.8**
Outer diameter stowed*, mm	1298.6	**1233.9**
Inner diameter deployed, mm	1773	**1773**
Outer diameter deployed, mm	1966.1	**1966.1**

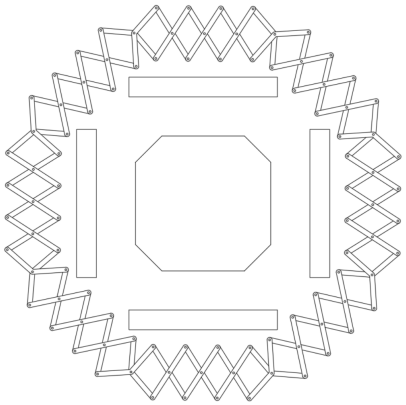

Figure 3.36: *The radial module around the spacecraft bus and M1 in stowed configuration with $n = 3$, $L = 101.6$ mm, $l = 182.0$ mm, $w = 15$ mm, $\theta = 36.8°$.*

the required volume goal 0.75 m^3, but definitely small enough so that the it would fit into the required volume threshold 1.5 m^3. With the outer stowed diameter of 1233.9 mm, the maximal stowed height goal is 0.627 m, and the threshold is 1.254 m (hard constraint). According to the 3D model of the instrument [44] the height of the telescope in stowed configuration is 999 mm (for further information see the next subsection Discussion about the SMSS). When the baffle stowed height is less than the instrument stowed height, the instrument height drives the volume calculation, so it is favorable to keep the baffle height lower than the instrument height not to further increase the volume (soft constraint).

3. The minimal deployed height of the baffle is constrained by the deployed instrument itself, as the baffle shall not be shorter than that. The deployed telescope is 2445 mm high [44], and it is a hard constraint that the baffle needs to be longer than that. Korhonen and Arink designed a 2700 mm [24] and a 2650 mm high baffle [5], respectively. To facilitate a fair trade-off, the pantographic baffle deployed height is aimed at 2650 mm, and if needed, fine-tuned in detailed design stage.

4. There is no constraint on the maximal deployed height of the baffle. Korhonen showed that higher baffle is advantageous temperature-wise [24], but it also adds mass to the system.

Discussion about the SMSS

The stowed configuration of the Secondary Mirror Support Structure has not been designed before, but it was needed for the stowed instrument height as the M2 spider is the the part that is situated at the greatest distance from the instrument housing. Therefore, a simple volumetric model of the DST was built with movable SMSS joints in order to simulate the spider distance from the instrument housing at any point of deployment. The main findings are:

- The SMSS reaches its stowed configuration when the root CORE hinges rotate approx. 86.9° from their initial axial position (the initial position is currently the deployed configuration, as it is the only one that has been designed). In this case the full height of the stowed instrument is 999 mm. Further stowage

is stopped by the top parts of the booms touching the moving cams of the root CORE hinges (see Figures 3.37 and 3.38). To reach this configuration the mid-boom integral slotted hinge (Figure 3.39) rotates 174.2°, however, it is advised to test if the cross section change of the booms because of the rotation of the hinge allows for the configuration seen in Figure 3.37 (where the cross section of the booms were left as circle for simplicity, with which the top and bottom parts of the booms intersect each other).

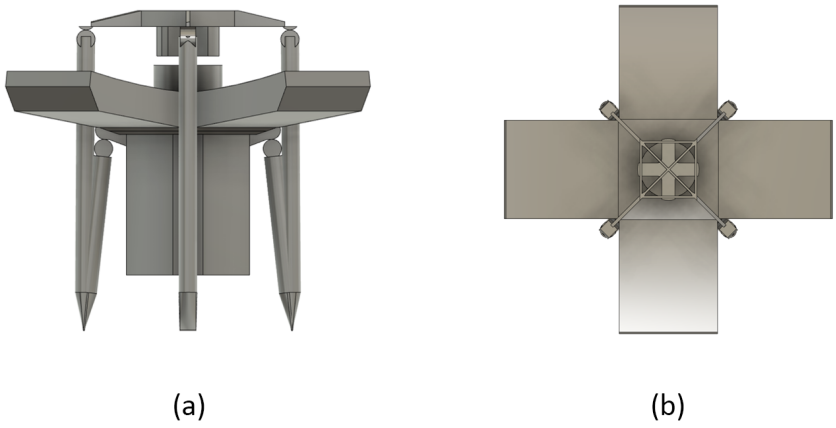

Figure 3.37: *The Secondary Mirror Support Structure (SMSS) in stowed configuration from (a) side and (b) top. The illustrations come from a simple volumetric model of the DST with movable SMSS joints.*

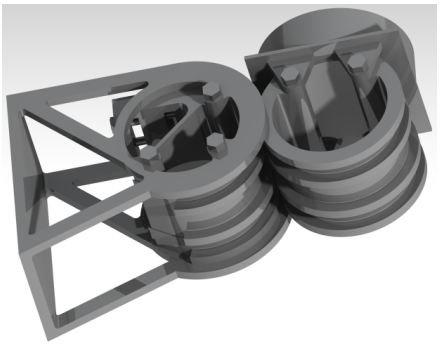

Figure 3.38: *Render of the root CORE hinge. The left cam is fixed, while the right one is moving. [25]*

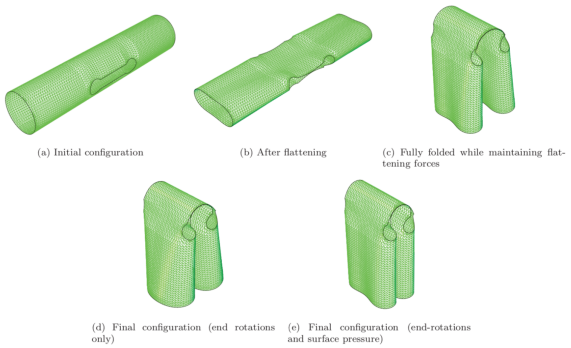

Figure 3.39: *Example of and integral slotted hinge. [5]*

- The current SMSS defines the required dimensions of the baffle both in radial and axial directions. The mid-hinges of the booms extend over the end of the instrument housing in the stowed configuration (Figure 3.37) by 211 mm, shifting the mounting position of the baffle further away from the instrument, making the required height of the baffle greater. At maximal radial extent of the SMSS booms the bottom part of the booms are in radial direction (Figure 3.40), and with the current length of the bottom part it greatly increases the required inner deployed diameter of the baffle. The diameter of circumscribed circle of the instrument in this configuration is 2115.4 mm, which means that with 100 mm clearance (requirement BAF-MEC-02-03-02) on both sides the required inner deployed diameter of the baffle would increase to 2315.4 mm from 1773 mm.
- The current SMSS was designed with only the deployed configuration in mind, meanwhile its stowed and intermediate configurations drive the baffle dimensions too much. If the inner deployed diameter of the baffle was increased to 2315.4 mm from 1773 mm (with the number of straight units n and arm width w remaining the same), the outer stowed diameter would increase by 9%, the area of the outer stowed radial cross section by 20% (proportional to stowed volume assuming fixed height), the outer deployed diameter by 30% (proportional to aerodynamic drag area), and the mass of the radial structure by 28%. These increased numbers are not justified for only one subsystem being able to deploy (once during LEOP). Furthermore, previous theses showed that the diameter of the baffle must be minimized to limit the amount of heat entering the baffle [5, 24]. Based on these reasons the current SMSS is not

considered as the driving subsystem for the baffle dimensions, and it is recommended that a new SMSS design is made which has a deployment radius (maximal radial extent) that is equal to or less than that of the primary mirror (1573 mm).

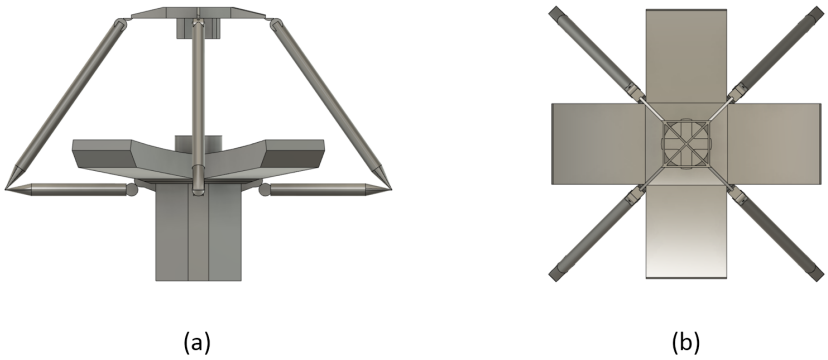

Figure 3.40: *Configuration of the SMSS at its maximal radial extent.*

3.6.7. Axial Design Options

The pantographic proof-of-concept prototype had straight axial modules that were perpendicular to the radial ones, see Figure 3.24. However, the straight axial modules were used as they were the simplest solution, and not the optimal one. The aim of this subsection is to find the optimal axial solution.

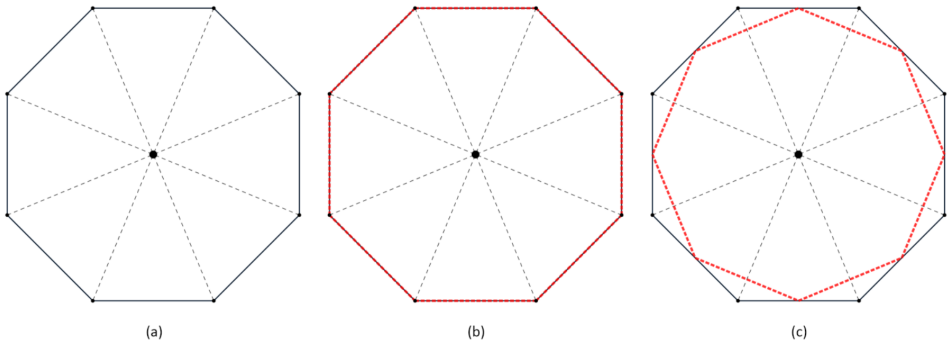

Figure 3.41: *(a) Eight rotationally symmetric segments of an octagon. Axial modules (red dashes lines) connecting (b) the neighboring vertices and (c) neighboring sides of two octagonal radial modules placed above each other, seen from the top.*

An octagon can be divided into eight rotationally symmetric segments with lines connecting the center and the vertices, see Figure 3.41a. The straight axial modules in the prototype were rotationally symmetric as well, connecting the same angulated units of the radial modules above each other. If not only straight axial modules are considered, a pantographic unit in the bottom radial module needs to be connected not to the unit directly above it, but to a neighboring one. The vertices of the octagon cannot be connected with pantographic units (as depicted in Figure 3.41b) because only mid-hinges of angulated units are situated there, and to translate deployment state between deployment planes two hinges are needed. To fully utilize the perimeter of the octagon for axial deployment, the other option is to connect the sides of the octagon with the axial modules as illustrated in Figure 3.41c. However, if the axial modules cross the border of the segments, the four endpoints of the axial module do not form a plane (see Figure 3.42), which means this kind of axial connection cannot be done with simple planar axial units. As simplicity is important in space structures, the options with axial modules crossing the segment borders are omitted.

To keep the endpoints in one plane, an axial module is limited to be situated in only one of the rotationally symmetric segments of an octagon. The two extreme solutions are straight and diagonal axial modules. As the vertices cannot be used, the best possible connection of the axial and radial modules is using the end rotational points of the angulated units within one segment. Figure 3.43 depicts the possible ways to place straight and diagonal axial units between two octagonal radial modules while staying in one segment with

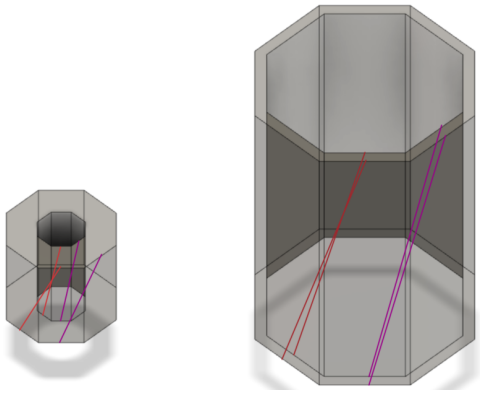

Figure 3.42: *Volumetric model of the DST baffle. Simplified axial modules (in red and violet) crossing the borders of the octagonal segments in stowed (left) and deployed (right) configuration. The four endpoints are connected to better show they are not in the same plane.*

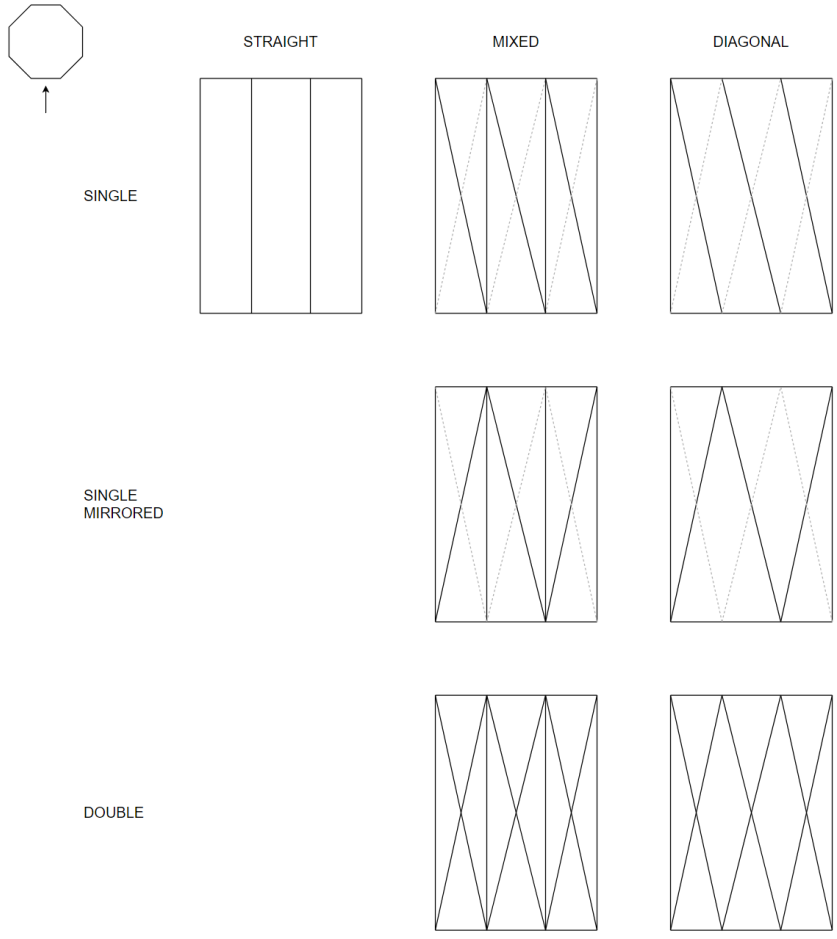

Figure 3.43: *Arrangement of the axial modules between two radial modules, seen from the side. In the first column the axial modules are straight, in the third column the axial modules are diagonal, and in the middle column the axial modules of the first and third rows are combined. In the first row the axial modules are rotationally symmetrical (45°), in the second one they are mirror symmetrical, and in the third one they are rotationally (45°) and mirror symmetrical. For simplicity, the endpoints of the axial modules are shown at the vertices of the octagons.*

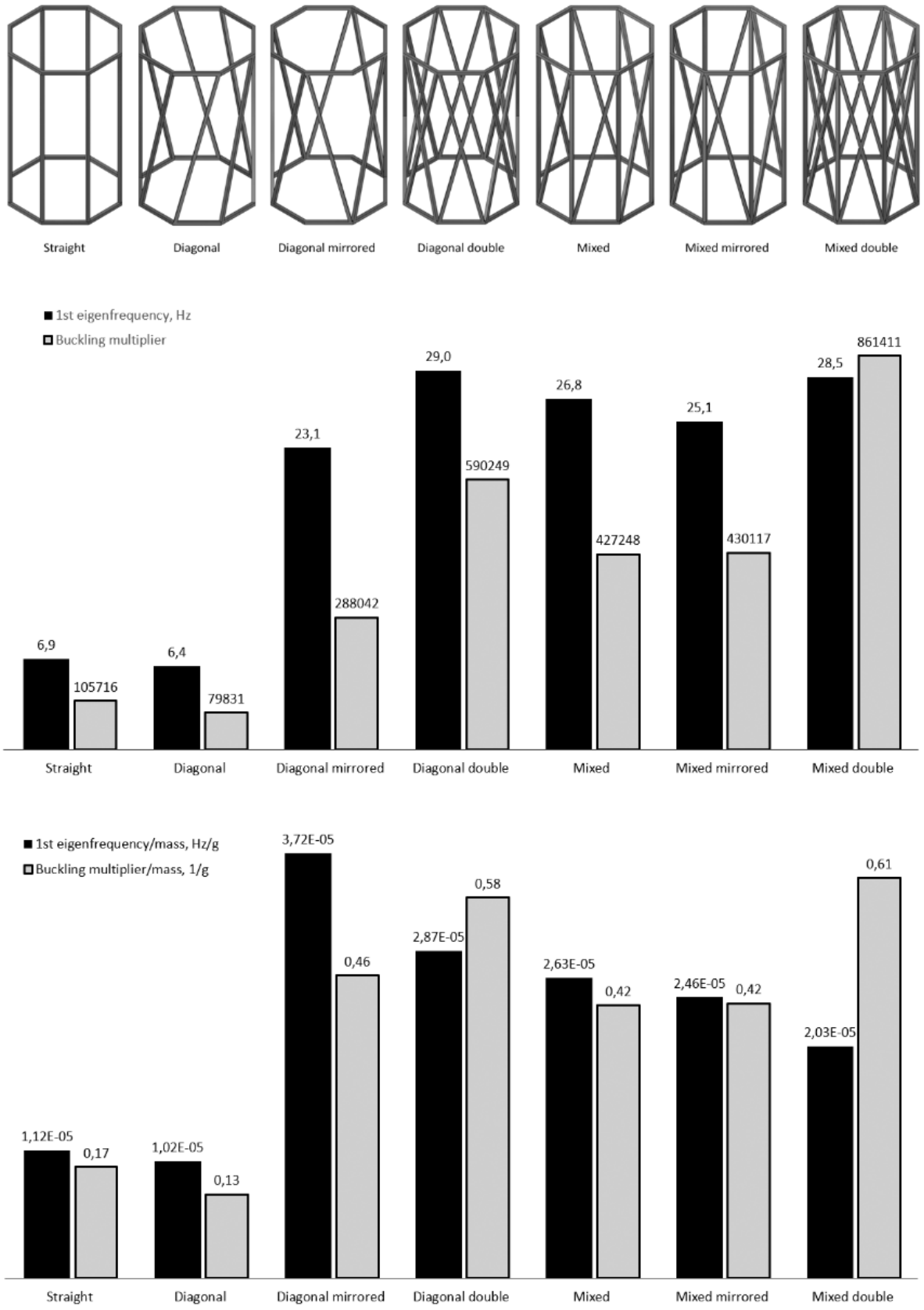

Figure 3.44: *FEM studies on seven simple models with different axial structures (top). Results of the modal and buckling analyses (middle), and the results divided by the structural mass (bottom).*

each of the axial modules. It is beneficial to increase the strength of the structure, but at the same time the mass and complexity of the baffle should be kept at minimum.

To compare the strength and load bearing capabilities of the different structures finite element method (FEM) is used. Simple models were prepared in Fusion 360 with octagonal base and straight, diagonal and mirrored diagonal axial structures to create the possible combinations presented in Figure 3.43, see Figure 3.44 first row. Both the octagons and axial structures have the same square cross section. The exact dimensions and material are irrelevant for the outcome of comparison as the relative results are enough for the decision. The simplified models are not representative for the pantographic structures, they serve as aids to decide the layout of the final structure. Similarly, the analysis results are not to be considered in an absolute sense, just to compare them with each other.

First, modal studies were performed on the models, of which the bottom faces were fixed. The first eigenfrequencies of the diagonal models, along with their specific values (by mass) are compared in Figure 3.44. The diagonal model has the lowest first eigenfrequency (6.4 Hz), followed by the straight one with 6.9 Hz, while all the others have more than three times more (between 23.1 and 29 Hz). The distribution of the specific values is quite similar, with the diagonal mirrored model having the highest eigenfrequency per unit mass. Higher first eigenfrequency means higher stiffness, and the study shows that adding extra axial structures (considering anything more complex than the diagonal mirrored model) barely increases the stiffness, but at the same time considerably increases the mass, eventually reducing the specific stiffness.

In the next study structural buckling was investigated. Buckling is a sudden deformation of the structure under load, and it is used as an example case to study the behavior of the structure under load. With the bottom faces fixed again, the same amount of compression force was applied normal to the top face of the models. The results are buckling multipliers (by what number the compression force could be multiplied before the structure fails due to buckling) and specific buckling multipliers, and are presented in Figure 3.44. The results show that it it beneficial to use double diagonal structures, and the more complex axial structures could compensate for the increased mass by the increased buckling multiplier.

The analyses were far from comprehensive, but they were intentionally kept simple as they are only used to select the best performing axial structure for the baffle. According to the studies carried out the diagonal mirrored axial structure has been selected for the following reasons:

- It has the highest specific stiffness among the tested models;
- It has the third highest specific buckling multiplier among the tested models, but the highest among the models with single axial modules (one axial module per segment);
- It has the second lowest mass among the tested models.

3.6.8. Geometrical Relationships in the Axial Modules

In this subsection the geometrical relationships of the diagonal mirrored axial modules are analyzed. The aim is to find the length p and number m of straight pantographic units that would form the the diagonal axial modules.

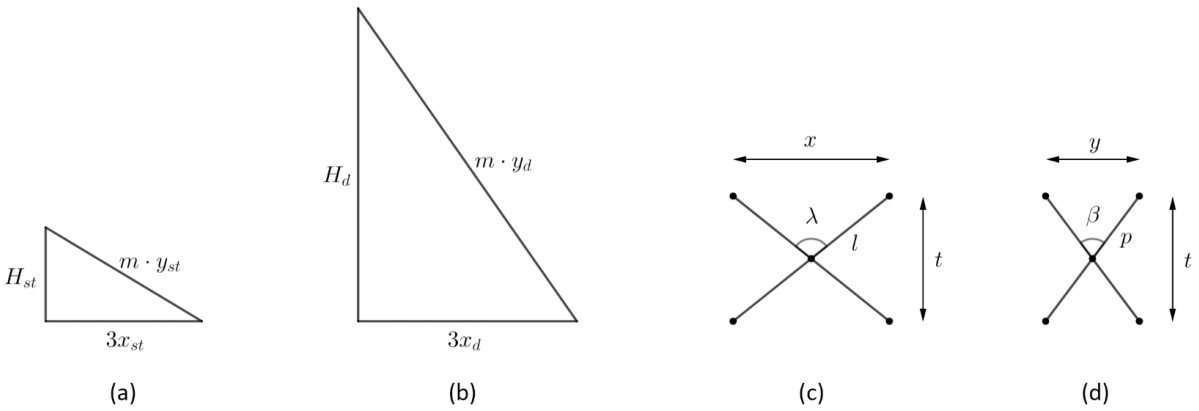

Figure 3.45: *Right triangle created by the axial module and the straight units of the radial module in (a) stowed and (b) deployed configuration. Dimensions of (c) a radial straight unit and (d) an axial straight unit.*

First, the required deployed height H_d is chosen. An axial module and the straight units of one segment

in the radial module create a right triangle, see Figure 3.45a-b. From the design of radial structure the length of a straight unit x is known in stowed (x_{st}) and deployed configuration (x_d). The deployed length of an axial straight unit y_d multiplied by the number of axial straight units m can be calculated using the Pythagorean theorem in the triangle in Figure 3.45b:

$$m \cdot y_d = \sqrt{H_d^2 + (3x_d)^2} \tag{3.13}$$

where 3 is the number of straight units n in a radial segment. With a given m y_d can be calculated. In deployed configuration the axial module is deployed as well, which means that knowing the distance of the end rotational points of the axial straight arms (that is equal to their arm width w) and their deployed length y_d the arm length p can be computed:

$$p = \sqrt{y_d^2 + w^2} \tag{3.14}$$

Next, using the known stowed radial straight unit radial thickness t_{st} and the axial straight arm length p, the stowed axial straight unit length y_{st} is:

$$y_{st} = \sqrt{p^2 - t_{st}^2} \tag{3.15}$$

The radial thickness t is the same for the radial straight and the axial straight units throughout the deployment process as they are connected by their end rotational points. Finally, according to Figure 3.45a the stowed height H_{st} can be calculated by:

$$H_{st} = \sqrt{(m \cdot y_{st})^2 - (3x_{st})^2} \tag{3.16}$$

where x_{st} is the radial straight unit length in deployed configuration.

3.6.9. Axial Design Optimization

In Equations (3.13) to (3.16) only the deployed height H_d, stowed height H_{st} and number of units in the axial module m are variables, the rest are known. With x_d = 181.37 mm, w = 15 mm, t_{st} = 153.53 mm, x_{st} = 97.8 mm Equations (3.13) to (3.16) can be simplified to:

$$H_{st} = \sqrt{209972 + H_d^2 - 23346.5m^2} \tag{3.17}$$

Figure 3.46 plots H_{st} as a function of H_d and m according to Equation (3.17), and contains the possible combinations of H_d, H_{st}, and m. The goal is to have a deployed axial height of 2650 mm, a vertical line can be drawn at 2650 mm, and where it intersects the graph curves, those are the possible solutions. Figure 3.46 shows that there is only one solution to have H_d = 2650 mm with H_{st} being lower than 999 mm (height of the stowed instrument without the baffle – soft constraint): with H_{st} = 696.7 mm and m = 17. The next solution would be with H_{st} = 1120.6 mm and m = 16, but it would increase the stowed volume of the whole instrument which is to be avoided.

If the baffle height was not fixed at 2650 mm but higher baffles would be acceptable as well, then with higher number of units (for example with m = 18, see Figure 3.46) smaller stowed height would be achievable than with m = 17. However, reducing the stowed baffle height (if it is already below 999 mm) does not provide any advantage as the instrument stowed volume is driven by the telescope stowed height, not the stowed baffle height. Furthermore, reducing the stowed baffle height would decrease the available space to store the folded MLI or other thermal protection. Consequently, the chosen axial module is the one with H_d = 2650 mm and m = 17, and its properties are summarized in Table 3.10.

Table 3.10: *Properties of the chosen axial module.*

Deployed height, mm	2650
Stowed height, mm	696.7
w, mm	15
p, mm	159.8
m	17
Stowed angle, degree	32.3

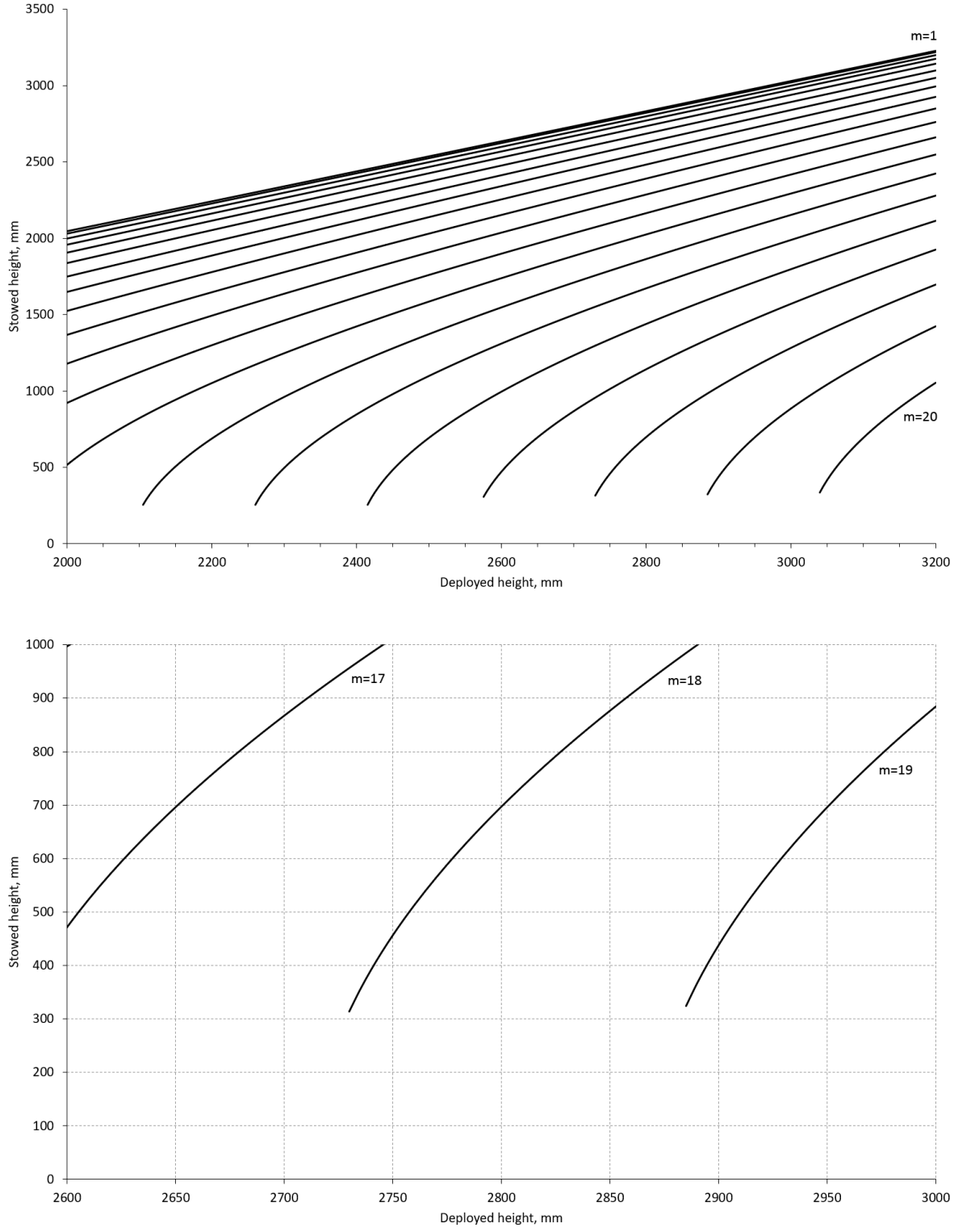

Figure 3.46: *Stowed height of the axial modules as a function of deployed height and number of units in the module m. At the bottom a part of the top diagram is enlarged to better showcase the available solutions with stowed height below 999 mm and deployed height at least 2650 mm.*

3.6.10. Arms Material Selection

There are three main criteria for the material of the pantographic arms:

1. **Space-grade.** The arms of the pantographic baffle are exposed to the harmful effects of space, including radiation and outgassing, among others. The selected material needs to perform well in those harsh conditions.
2. **Light.** The requirement of low mass is twofold: the mass is restricted by the scope of mission and the mass budget, but it is also important not to overwhelm the ADCS (Attitude Determination and Control System) of the spacecraft with massive and extensive appendages that would severely affect the MMOI (mass moment of inertia) of the spacecraft. Materials with low density (ρ) are preferred.
3. **Stiff.** To keep the eigenfrequencies of the structure high, stiff materials are required, or in other words, their flexibility should be low. Materials with high Young's modulus E are favored.

The lightness and stiffness of the material can be combined into another property: the specific stiffness (E/ρ) of the material shall be great. However, this property does not substitute its parent properties on its own.

Reinforced plastic composites are often used in industries where high specific stiffness is required as they usually combine high stiffness with low density. They consist of a polymer matrix reinforced with fibers (usually glass or carbon). The fibers provide outstanding tensile modulus to the composite, but the presence of fibers make the strength and stiffness of these composites direction sensitive, narrowing their range of usability. Furthermore, because of the unidirectional properties composite interfaces are often problematic as they are prone to cracking [17, 50]. The pantographic baffle includes more than 600 interfaces, magnifying the potential issue. Because of these reasons, the usage of composites as arms material is omitted.

Next, the group of aerospace-grade metal alloys with high specific stiffness is inspected. When low mass is required, aluminium and its alloys are preferred, and the one with the highest specific stiffness is sought. This requirement leads to the group of Al-Li (aluminium-lithium) alloys, where lower density than pure aluminium is paired with higher Young's modulus, furthermore, they have excellent fatigue and cryogenic toughness properties [41]. Al-Li 8090 stands out with its highest specific stiffness, and its mechanical properties are summarized in Table 3.11 [23, 31]. Because of its isotropic material properties, low density and high Young's modulus Al-Li 8090 is selected as the arms material.

In the selection of the arms material classical design approach and manufacturing techniques were considered. However, one might find innovative approaches that could result in a baffle with better mechanical properties while changing the material selection and the arms design. Such approaches could be 3D printing and compliant pantographic structures, among others. The study of these is left for future work.

Table 3.11: *Physical properties of Al-Li 8090 alloy (CTE: Coefficient of thermal expansion). [23, 31]*

Density	2550	kg/m^3
Young's modulus	77	GPa
Tensile strength	450	MPa
Yield strength	370	MPa
Shear strength	270	MPa
Specific stiffness	$3.0 \cdot 10^7$	m^2/s^2
CTE	21.4	µm/mK
Thermal conductivity	95.3	W/mK
Specific heat	930	J/kgK

3.6.11. Preliminary Arm Optimization

The design of the arms in the pantographic structure have consisted of simple outlines and holes for the joints so far (Figure 3.47a), but they are not necessarily the best design mass-wise. However, mass is not the only important characteristic of the structure: it is required to be lightweight and stiff at the same time, and these have opposite effects on each other. In the preliminary design the arms are modified to save some mass meanwhile retaining stiffness, but the arms designs are not optimized (to be done during detailed design).

The thickness of the arms did not play an important role in the design of the planar radial - and axial modules, and for the preliminary design it is fixed at 5 mm. The reason behind it is that according to the 3D models and analyses it results in a mass - stiffness balance, none of them is sacrificed for the other.

Without changing the general shape of the arm (that is left for the detailed design) some of the less load-bearing parts can be removed. For this two configurations were analysed, both of them practically being an H-beam, but the material is removed from different faces, see Figure 3.47b-c that show the results for the radial straight arms, but the axial straight - and the radial angulated arms are lightened likewise. The lightening was performed by leaving 1.5 mm material thickness in the H-beams, and removing the rest. 1.5 mm was chosen because it results in a proportionate structure.

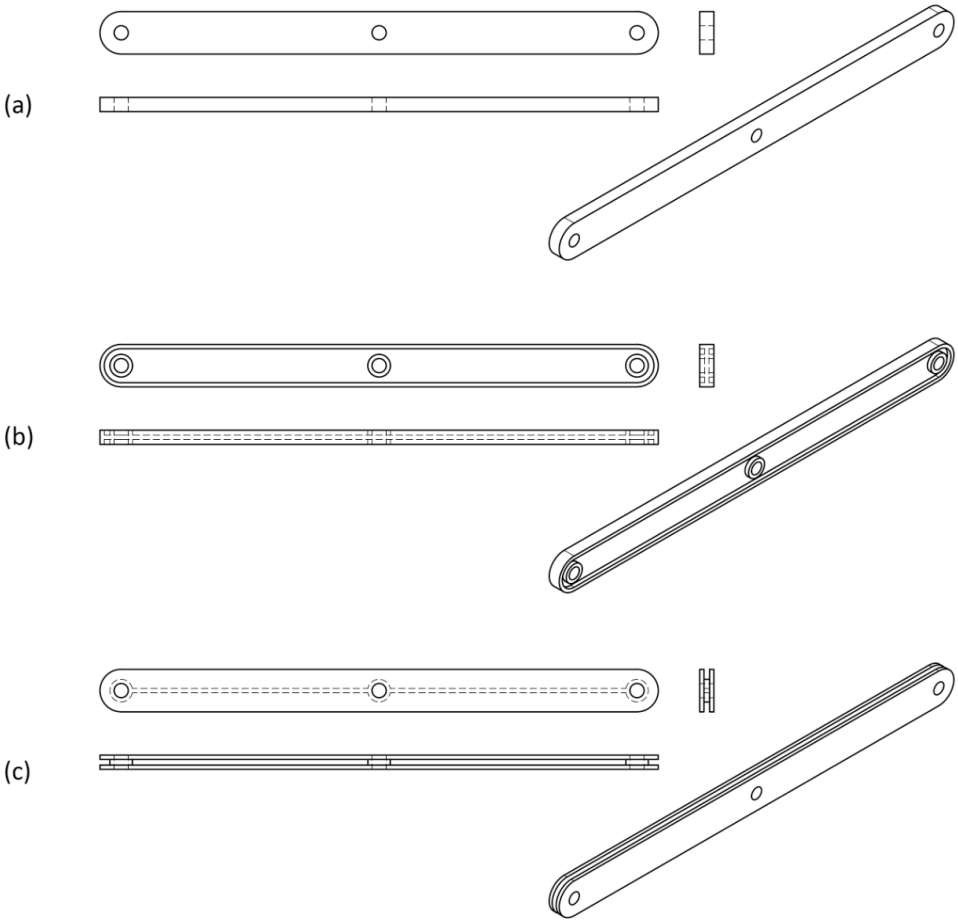

Figure 3.47: *Design of the lightened radial straight arm. (a) Original design without lightening, (b)-(c) "H-beam" lightened designs.*

Table 3.12: *Comparison of the first eigenfrequencies (f) and mass of an axial module consisting of arms of different lightened versions. The designs are aligned with the ones in Figure 3.47. Mass of the different designs are compared to design (a),*

Design	Stowed f, Hz	Deployed f, Hz	Rel. mass
(a) Original design	26.69	11.22	1
(b) Lightened design 1	7.667	13.63	0.477
(c) Lightened design 2	9.142	12.83	0.649

Axial modules consisting of 17 axial units (34 axial straight arms) with the three different lightening solutions have been designed to analyse the effect of the lightening on the stiffness and the mass of the modules. The analyses are solely for relative comparisons as they lack real-life aspects e.g. the forces exerted by the hold-down-and-release mechanisms. The modules were fixed by the four outermost holes of the structure at the two ends, and the material was set to the previously selected Al-Li 8090. The results of the finite element analyses are shown in Table 3.12. Mass-wise design (b) provides better lightening, but the first eigenfrequencies show ambivalent results: design 1 is better in deployed -, while design 2 is superior in stowed configuration. Interestingly, both lightened designs have higher first eigenfrequencies in deployed configuration than the original design, but the stowed eigenfrequencies of the lightened designs cannot reach that of the

original design. Even though design 2 is heavier than design 1, design 2 is selected because its higher stowed eigenfrequency that is a more critical requirement.

The results of the lightening show that there is room for improvement, and the arms designs are not yet optimized. While the deployed stiffness is maintained, the stowed stiffness suffers from the lightening. Currently the stowed and deployed stiffnesses are comparable to each other, but the requirements are much more stringent with the stowed one (100 Hz vs. 0.9 Hz). This gives an opportunity to create a design that selectively reinforces the stiffness in stowed configuration, even to the expense of the deployed one. This will be further analyzed in the detailed design.

The result of the preliminary design of the pantographic structure is presented in Figure 3.48.

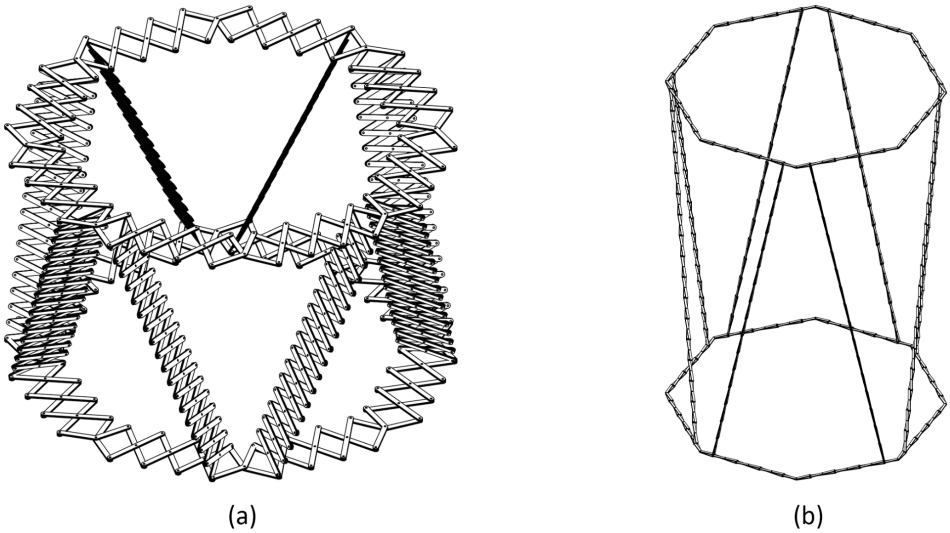

Figure 3.48: *Preliminary design of the pantographic structure in (a) stowed and (b) deployed configuration. The drawings are not to scale to each other.*

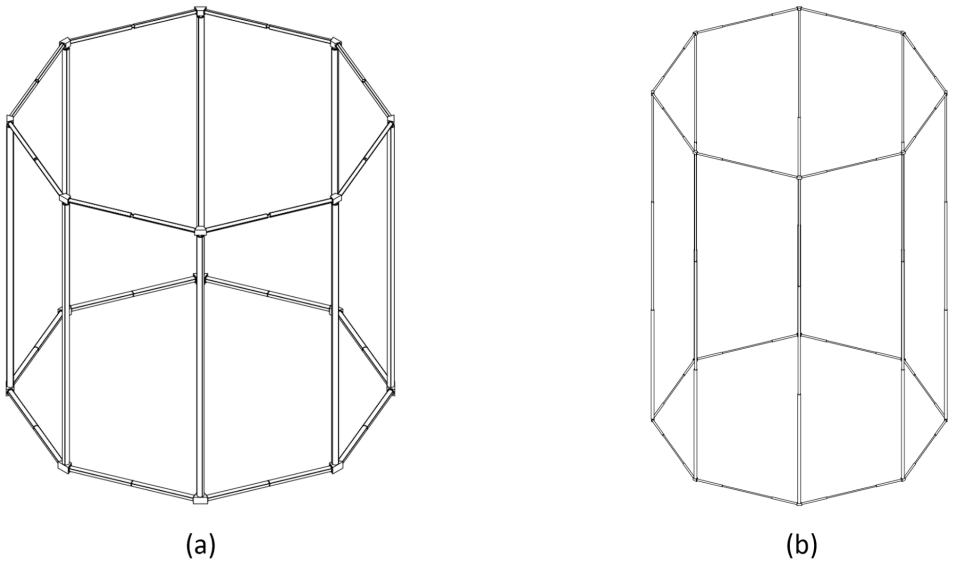

Figure 3.49: *Preliminary design of the telescopic structure in (a) stowed and (b) deployed configuration, based or Arink's work. The drawings are not to scale to each other. [5]*

3.7. Telescopic Concept Preliminary Design

The telescopic concept has been previously worked out by Arink [5] as his best design for the baffle. However, he made a mistake with the material selection that made his modal analysis results and mass extremely good.

His design and analysis files were available, so the mistake can be corrected.

In his thesis Arink concluded that aluminium alloys do not have high enough specific stiffness to make the structure rigid enough to comply with the modal requirements. Therefore, he has changed the material to "M55J which is an high-modulus epoxy CFRP" [5]. However, M55J is a high modulus fiber, not a CFRP, so practically the outstanding fiber properties (Young's modulus, density) were used in the simulations, not the composite properties [5, 47]. Moreover, the material was modelled isotropically, suggesting that the fiber has the same material properties in all directions. However, fibers have exceptional properties in one direction, while the properties in other directions are inferior to that [17].

The required properties of different M55J composites are not readily available, and properly modelling composite materials is an involved process not suited for preliminary design, therefore the material of the telescopic design is changed to the material of the pantographic structure, Al-Li 8090. This alloy has been selected for the pantographic structure as a low-density alloy with high specific stiffness, and the basic requirements for material selection are the same for the telescopic structure as well. None of the preliminary designs have been iterated to reach the required stiffness and mass, so selecting the same material for both designs does not make the trade-off unfair, as none of the designs have been optimized for the material.

As the interface between the spacecraft bus and the pantographic baffle has not been designed yet, the radial telescopic arms meant as such interfaces in Arink's design have been removed to allow for fair comparison (in terms of mass and aligned constraints). The result is shown in Figure 3.49, and it is the preliminary telescopic design.

3.8. Trade-off

The preliminary designs of the two noteworthy alternatives have been worked out, and they are graded according to the defined criteria in Section 3.3.

3.8.1. Mass

The pantographic structure consists of arms, pins, and joints. The mass of the arms is directly measurable in the 3D model, they are 8755 g. The pins are modelled as solid cylinders that connect the holes of the adjacent arms, going from the outer face of one arm to the outer face of the other arm, and having the same diameter of the holes. For simplicity the pin material is chosen to be the same as for the arms (preliminary assumption). This way one pin is 0.511 g, the 584 pins in the structure together are 298.4 g. There are 32 joints (not yet modelled) that connects the radial and the axial modules, they are assumed to have the mass of 5 pins each, resulting in a total mass of 81.76 g. The mass of the pantographic structure, including arms, pins, and joints, is 9135.2 g. The mass of the telescopic structure is 4625 g, measured in the 3D design.

There are some other elements that need to be added to both of the designs. In Arink's theses 2766 g of truncated cone, 1816 g of actuation, and 1960 g of MLI are added to the mass of the baffle frame. All of them are considered and added to the pantographic baffle as well, ignoring the possible differences (e.g. less amount of required actuators). In the telescopic design the mass of the removed radial arms for the integration of the baffle and the spacecraft bus (329.7 g) is added as well. To compensate for the heavier build, this mass is modified by the pantographic/telescopic structure mass ratio (9135.2/4625), consequently 651.3 g is considered for the integration of the pantographic structure. The resulting masses are 16328.5 g for the pantographic -, and 11496.7 g for the telescopic structure. The grades are presented in Table 3.13.

The telescopic alternative has a considerably lighter structure, but the additional parts (MLI, actuation, truncated cone) that has the same weight for both alternatives reduce the relative difference between the two designs. The telescopic one could achieve the substantially lower mass by being an already optimized design, yet for the wrong material, as previously explained. The pantographic structure is not yet optimized, and it is reflected in the high mass. It is believed that further optimizations could reduce the mass of the pantographic structure.

Table 3.13: *Grading of the alternatives for mass according to Figure 3.1. Relative grades are given so that the sum of the grades is 1.*

Alternative	Mass, kg	Grade	Rel. grade
Pantographic	16.33	4.65	0.44
Telescopic	11.50	5.93	0.56

3.8.2. Stowed Volume

The stowed volume is the volume of the bounding cylinder in which the instrument (including the baffle) fits. As the MLI and other appendages are not yet designed for both baffles, only the baffle frame is considered.

The stowed pantographic baffle fits in a cylinder with 1233.9 mm diameter and 717.2 mm height, however, the stowed instrument is 999 mm high, which means this height needs to be considered for the bounding cylinder. The stowed volume of the pantographic structure is therefore 1.19 m^3.

Arink's telescopic design has a diameter of 1085.6 mm and height of 933 mm in stowed configuration. The stowed instrument is higher than the stowed baffle, so again, the 999 mm stowed instrument height is considered. The stowed volume of the telescopic structure is 0.92 m^3. The grading is shown in Table 3.14.

During the design of the pantographic structure its considerable radial thickness in stowed configuration was highlighted. Arink's design maintains its modest radial thickness in all configurations, therefore it has a lower stowed diameter and volume.

Table 3.14: *Grading of the alternatives for stowed volume. Grading is according to Figure 3.2. Relative grades are given so that the sum of the grades is 1.*

Alternative	**St. volume,** m^3	**Grade**	**Rel. grade**
Pantographic	1.19	5.76	0.44
Telescopic	0.92	7.35	0.56

3.8.3. Stowed Stiffness

The stowed stiffness of the alternatives is determined by finite element analysis. In the analyses – to simulate the integration to the spacecraft bus – the vertices of the octagon of the bottom radial module are fixed: in the pantographic structure the bottom face of the pins in the vertices are fixed, meanwhile in the telescopic design the bottom faces of the connecting hubs in the vertices are fixed. The results of the stiffness analyses are to be used for relative comparison only, as they lack for example the incorporation of baffle elements other than the frame.

The analyses returned a first eigenfrequency of 35.59 Hz for the pantographic -, and 21.92 Hz for the telescopic structure. The grading is shown in Table 3.15.

The first eigenfrequency of stowed pantographic structure is substantially higher than that of the stowed telescopic structure, however, as they both far away from the required 100 Hz, both are given the lowest grade. The low first eigenfrequency of the stowed telescopic structure was expected, because with aluminium Arink's results were subpar, and it initiated the change for the badly defined carbon fiber [5]. The stowed pantographic structure has higher first eigenfrequency, but not high enough as it has not been optimized yet, and it is foreseen that it can be improved.

Table 3.15: *Grading of the alternatives for stowed stiffness. Grading is according to Figure 3.3. Relative grades are given so that the sum of the grades is 1.*

Alternative	**1st eigenfrequency, Hz**	**Grade**	**Rel. grade**
Pantographic	35.59	1	0.5
Telescopic	21.92	1	0.5

3.8.4. Deployed Stiffness

Similarly to the stowed stiffness, the deployed stiffness is determined by finite element analysis. Again, the results of the stiffness analyses are to be used for relative comparison only. The setup of the analyses is identical to the one with the stowed stiffness studies. The analyses returned a first eigenfrequency of 20.40 Hz for the pantographic -, and 5.54 Hz for the telescopic structure. The grading is shown in Table 3.16.

As mentioned previously, the stiffness of the axial module of the pantographic structure was outstanding in deployed configuration, and the modal analysis of the entire structure further confirms that. However, overachievement is not necessarily good as it means the mass could be reduced or rearranged to increase the stowed stiffness to the expense of the deployed stiffness. The deployed stiffness of the telescopic structure exceeds the requirement, too, but is considerably lower than the stiffness of the pantograhic structure.

Table 3.16: *Grading of the alternatives for deployed stiffness. Grading is according to Figure 3.4. Relative grades are given so that the sum of the grades is 1.*

Alternative	1st eigenfrequency, Hz	Grade	Rel. grade
Pantographic	20.40	9	0.56
Telescopic	5.54	7.04	0.44

3.8.5. Required Number of Actuators

The pantographic structure stands out of the competition with its lowest possible required number of actuators: as the whole structure is pantographically linked, with only one angle the deployment state of the entire structure can be described. This means that – theoretically – only one actuator is enough to deploy the pantographic baffle.

For the telescopic design at least two actuators are needed: one to deploy the structure radially, and another to deploy it axially [5]. The required number of actuators are valid for active (driving actuators) and passive (release actuators) deployment as well. The grading is presented in Table 3.17.

Table 3.17: *Grading of the alternatives for required number of actuators. Grading is according to Figure 3.5. Relative grades are given so that the sum of the grades is 1.*

Alternative	Required no. of actuators, pcs.	Grade	Rel. grade
Pantographic	1	9	0.59
Telescopic	2	6.33	0.41

3.8.6. Actuation Method

Both of the alternatives can deploy passively and actively, but the possibility of passive deployment is better appreciated. Pantographic structures can be modified to incorporate flexible composite hinges instead of pins, which aim to return to their minimal energy state (deployed configuration) after setting free [51]. Springs can be used to deploy the concentric elements of the telescopic booms [37]. However, the complexity of the actuation of the telescopic structure is deemed to be higher than that of the pantographic structure as in the pantographic structure the flexible composite hinges can easily replace the traditional hinges without taking up considerable extra space, meanwhile the integration of the springs into the design of the telescopic booms requires significant design changes. Regarding active actuation the alternatives are considered equal (the number of actuators is a separate criterion).

The nonquantifiable criteria that are graded directly with relative grades that add up to 1. The reason behind this is that it gives wider input options than the AHP pairwise comparison used in the criteria selection (that is limited to 50%-50% and 66.7%-33.3% with similarly achieving alternatives). The grading of the alternatives for actuation method is given as follows: 0.55 for the pantographic -, and 0.45 for the telescopic structure.

3.8.7. Integration Complexity

In the pantographic structure the integration of the shroud to the frame is regarded easier as the axial structure provides more and evenly distributed fastening possibilities, while in the telescopic structure the fastening possibilities are reduced to the bottom axial elements and the very tip of the top axial elements. Therefore for the complexity of the integration of the shroud and the frame the pantographic structure is graded with 0.6, and the telescopic one with 0.4.

The integration of the frame to the spacecraft bus is easier to solve by telescopic booms. The predefined geometrical relationships of the pantographic structure makes designing a proper boom (that supports the frame and follows its deployment) more involved. The pantographic structure is graded with 0.4, the telescopic structure is graded with 0.6 for the integration of the frame to the spacecraft bus.

When both of the integrations are considered, the averaged grades are 0.5 for both alternatives.

3.8.8. Flexibility

Both of the alternatives can be adjusted based on late requirement updates, however, the more complex geometrical relationships of the pantographic structure makes it slightly more difficult: the grades are 0.45 and 0.55 for the pantographic - and the telescopic structures, respectively.

The theoretical best design can be better followed by the pantographic structure as complex curved faces can be created with it [42], meanwhile the telescopic structure can only form straight faces. Therefore the pantographic structure is graded with 0.6, and the telescopic one with 0.4.

By averaging the grades the pantographic structure receives 0.525, and the telescopic structure is graded with 0.475.

3.8.9. Reliability

Reliability is a crucial criterion, but at this design stage the reliability of the baffle and its components are not quantifiable, and the comparison cannot be made. Consequently the grades for reliability is 0.5 for both the pantographic and the telescopic baffle.

3.8.10. Baffle Goals Compliance

The goals of the baffle include providing stable temperatures, stray-light prevention, and protection against space debris. With respect to providing stable temperatures the pantographic structure has more possibilities in stopping the heat from reaching the instrument: it has more flexibility with the truncated cones and other appendages (more fastening positions, linked deployment). Therefore, the grades are 0.55 for the pantographic baffle and 0.45 for the telescopic one.

Stay-light prevention has basically the same requirements as providing stable temperatures, so the same grading is used.

In providing protection against space debris the shroud plays the major part, thus the alternatives (which are just the baffle frames) are graded with equal numbers: 0.5 for both of them.

The averaged grades of the three goals are: 0.53 for the pantographic structure and 0.47 for the telescopic design.

3.8.11. Result

Using the priorities of the criteria and the grading of the alternatives the global preferences of the alternatives can be calculated. It results in 51.2% for the pantographic structure and 48.8% for the telescopic ones, see Figure 3.50.

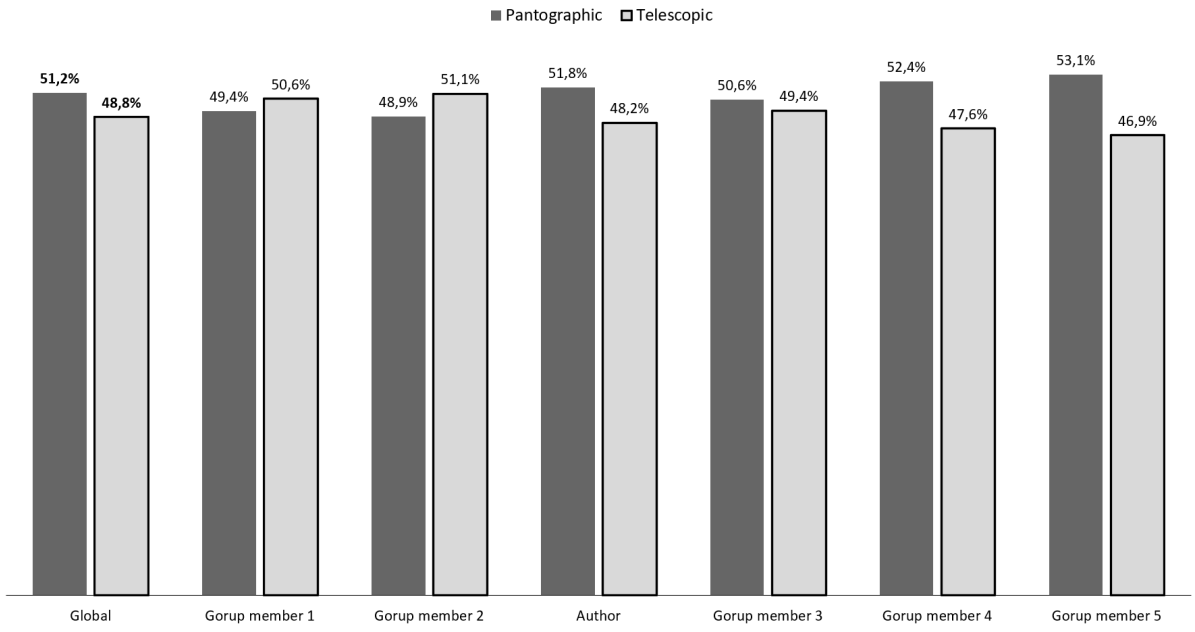

Figure 3.50: *Preferences for the alternatives. Global preferences (left) and preferences of the participants.*

3.9. Discussion & Sensitivity of the Trade-off

The trade-off results are quite close to each other, which predicts high sensitivity. Looking at the preferences of the different participants shows that four participants prefer one, and two prefer the other alternative, and the highest difference in preferences is 6.2%, see Figure 3.50. In this environment changing any criterion priority or alternative grading could potentially result in a different outcome of the trade-off. The sensitivity of the trade-off is checked by Monte Carlo simulation.

In the Monte Carlo simulation the input data of the trade-off are given uncertainties with predefined range and distribution, and the preferences are calculated using repeated random sampling of them. After numerous calculations the preferences of the alternatives show a distribution of the possible outcomes.

The uncertainties of the grading of the alternatives are presented in Table 3.18. For the criteria with predefined numerical grading the uncertainties were introduced as range of proportions of the input value. Higher uncertainties were added to criteria that include more assumption (mass, stowed stiffness, deployed stiffness), and lower to ones with more confidence in the accuracy of the values (stowed volume, required number of actuators). For the other criteria that cannot be quantified a different way was introduced to include uncertainties: they are given as allowed range of relative grade differences compared to the mean value. The sum of the relative grades of the alternatives is always one. As for the other group of criteria, lower uncertainties mean higher confidence in the accuracy of the mean value, and vice versa. Uncertainties are introduced for the global criteria weights as well according to Figure 3.7.

The criteria weights were based on group decision making, but the expected depth of understanding of the alternatives was too high to use the group method in the grading of the alternatives, too. Consequently, the grades of the criteria without predefined numerical grading are inevitably subjective. The subjectivity of the grading was considered as well while defining uncertainties.

Table 3.18: *Uncertainties of the grading of the alternatives. Grading/Proportion: for these criteria a predefined numerical grading is available, and the uncertainties are defined as a range of proportions of the grading input values. Pairwise comp./Rel. grade diff.: for these criteria no predefined grading is available, the grading is done with pairwise comparisons. The uncertainties are defined as a range of possible relative grade differences, but the sum of the relative grades is always 1. (IC: integration complexity, Flex: flexibility, BGC: baffle goals compliance)*

Criterion	Method	Pantographic	Telescopic	Uncertainties
Mass	Grading/Proportion	16.33 kg	11.50 kg	± 20%
Stowed volume	Grading/Proportion	1.19 m^3	0.92 m^3	± 5%
Stowed stiffness	Grading/Proportion	35.59 Hz	21.92 Hz	± 30%
Deployed stiffness	Grading/Proportion	20.40 Hz	5.54 Hz	± 30%
Required number of actuators	Grading/Proportion	1	2	± 0%
Actuation method	Pairwise comp./Rel. grade diff.	0.55	0.45	± 0.05
IC 1: Frame + shroud	Pairwise comp./Rel. grade diff.	0.6	0.4	± 0.1
IC 2: Frame + S/C bus	Pairwise comp./Rel. grade diff.	0.4	0.6	± 0.1
Flex 1: Follow requirement updates	Pairwise comp./Rel. grade diff.	0.45	0.55	± 0.05
Flex 2: Follow theoretical best design	Pairwise comp./Rel. grade diff.	0.6	0.4	± 0.1
Reliability	Pairwise comp./Rel. grade diff.	0.5	0.5	± 0.3
BGC 1: Stable temperature	Pairwise comp./Rel. grade diff.	0.55	0.45	± 0.05
BGC 2: Stray-light	Pairwise comp./Rel. grade diff.	0.55	0.45	± 0.05
BGC 3: Space debris	Pairwise comp./Rel. grade diff.	0.5	0.5	± 0

The distribution of the uncertainties is assumed to be normal, and the given uncertainty ranges are considered as standard deviations. The trade-off was executed one million times, and the results are presented as preference occurrence histograms in Figure 3.51. The sensitivity analysis returns the same mean preferences as Figure 3.50, however, it does show that the actual values of the grades of the alternatives within their uncertainty ranges can affect the outcome of the trade-off.

According to the trade-off and its sensitivity analysis the alternatives are similarly preferred, and there is no real winner with outstanding scores. This also means that the deployment concept of the DST baffle cannot be selected based on solely the trade-off. (Scaled) prototypes of both structures might help to gain more understanding of the capabilities and limitations of the alternatives, and reduce the uncertainties, but it is a recommendation for future work. For now, however, the research perspective is considered: combining and linking the radial and axial deployment of the baffle by the means of pantographic arms is an innovative solution that has not been done before for baffle deployment. Based on this, the pantographic design is selected to be worked out further in the detailed design.

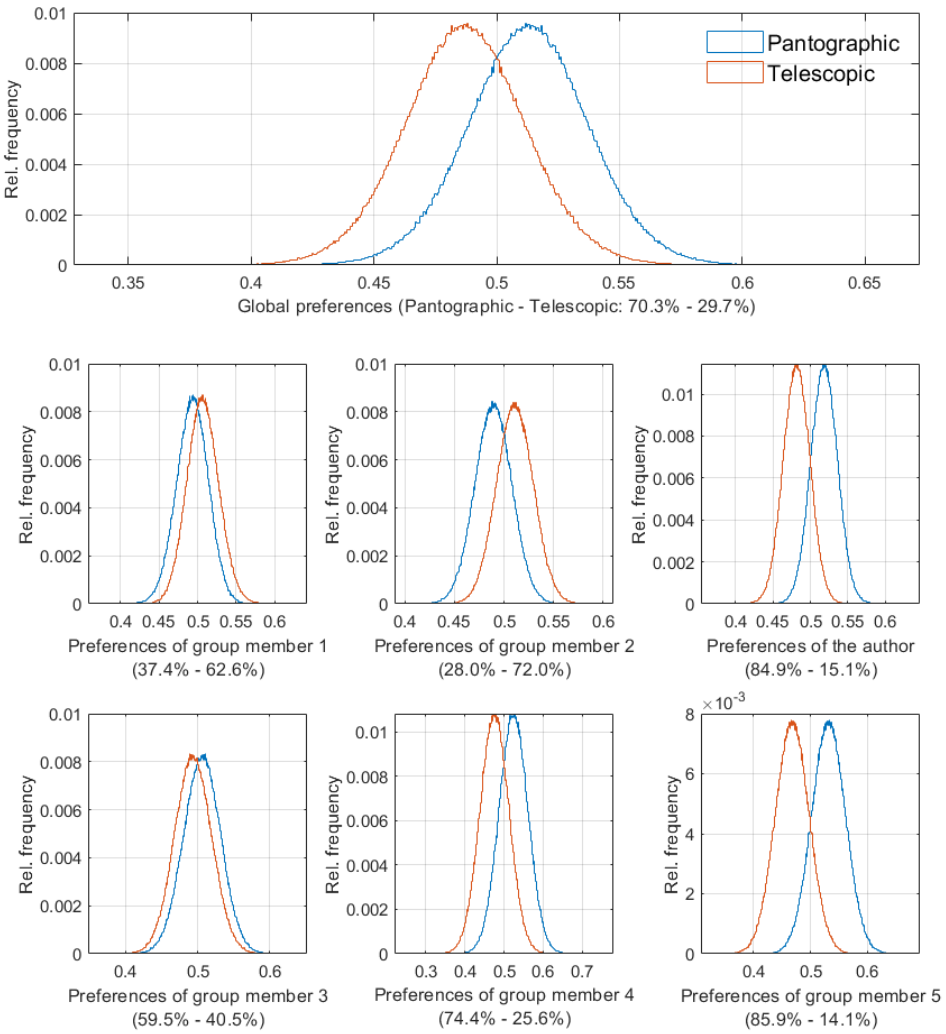

Figure 3.51: *Results of the Monte Carlo simulation for sensitivity analysis of the trade-off with normal distribution and one million runs. Top: global results, bottom: results per participant. The percentages in the labels show the winning ratios of the alternatives out of one million runs.*

4

Preliminary Thermomechanical Design

In this chapter the preliminary thermomechanical design of the deployable baffle for the Deployable Space Telescope is presented. The preliminary mechanical design of the pantographic structure is updated to the requirements of a new telescope design, and it is worked out in more details. The thermal performance of the design is checked with thermal analyses, and the results are used to iterate the design.

4.1. Change to TIR

During the work on this thesis an important decision has been made by the DST project leaders: instead of the visual spectrum, the Deployable Space Telescope shall work in the thermal infrared (TIR) spectrum. The TIR spectrum is a long-wavelength region (8-15 μm) within the infrared spectrum, and this is the characteristic region of the radiation emitted by objects on Earth [36].

4.1.1. Reasons

The reasons behind the change are threefold [7]:

1. **Interest.** There is an interest from defense for increasing TIR resolution. More interest increases the funding possibilities that are required for the project to leave "phase A".

2. **Novelty.** For the VIS, same GSD satellites already exist, and the VIS DST is a novelty only in the sense of cost reduction. However, the TIR DST would have a higher resolution than the current TIR telescopes, at least in Europe.

3. **Technical perspective.** TIR is easier from the optical alignment perspective (alignment budgets are relaxed by a factor of ~ 15). On the other hand, the probable need for cooling complicates the design for TIR, but it has been done in the past.

4.1.2. Mirrors

For the TIR spectrum the telescope needs to be redesigned from scratch. Based on the latest optical design of the TIR telescope [14] its mirror placements are presented in Figure 4.1 in contrast to the VIS telescope. The external diameter of the deployed telescope has barely changed, however, its height has been significantly reduced. This is caused by the decreased distance between M1 and M2.

4.1.3. Deployment of the Mirrors

For the baffle design the dimensions of the telescope are required in both stowed and deployed configuration. As an input only the mirror dimensions and their relative distances are available, consequently, the rest of the major components of the instrument and their deployment need to be designed. Naturally, these tasks exceed the scope of this thesis, however, they need to be done at least on a conceptual level to give an idea about the required dimensions of the baffle.

Two mirror deployment concepts have been considered initially. The first one is the replica of the VIS mirror deployment that has been adapted to the new mirror dimensions, see Figure 4.3. The second concept

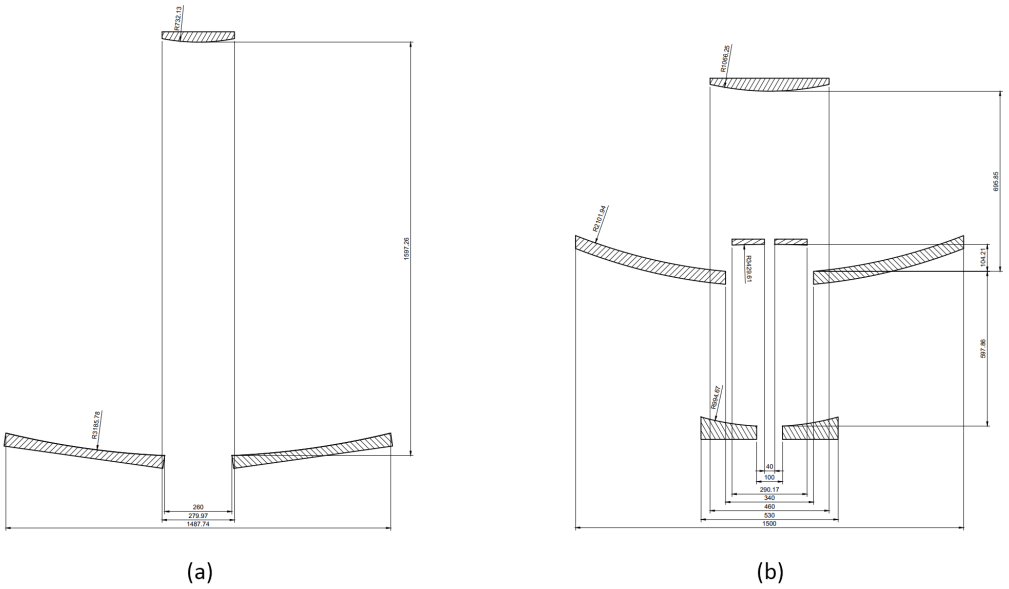

Figure 4.1: *Comparison of the mirror placements of the VIS and the TIR DST. The drawings are to scale to each other. (a) VIS design, mirrors from top to bottom: M2, M1 (the rest of the mirrors are not included in the drawing). (b) TIR design, mirrors from top to bottom: M2, M4, M1, M3. [5, 14]*

is based on the expected need of cooling of the instrument housing. Consequently, this concept leaves as much surface of the instrument housing free as possible.

The idea behind the second concept is making the M1 segments foldable upwards instead of downwards that was realized in the VIS DST. This way the baffle could be mounted to the instrument housing higher, leaving considerable amount of uncovered instrument housing surface for cooling purposes. However, folding the M1 segments upwards is more involved than folding them downwards: unless the hinge points are placed well, the folding segments collide during deployment. Based on the analysis of the possible hinge points the ones that allow for collision-free deployment are presented in Figure 4.2 above the blue line. Alternatively, a more complex M1 deployment system can be designed to avoid the interference of the parts.

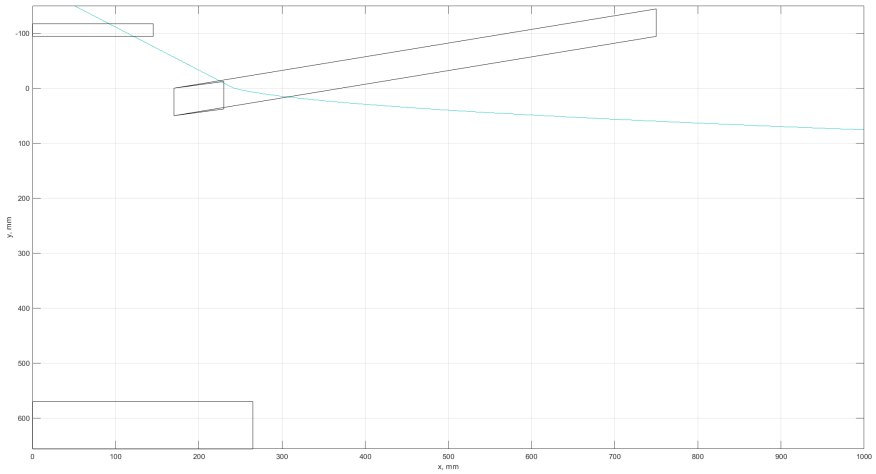

Figure 4.2: *The hinge points that allow for collision-free deployment are above the blue line. The drawn deployed mirrors (from top to bottom) are M4, one segment of M1, M3. The origin of the coordinate system is placed in the optical axis of the instrument (x=0), at the same height as the M1 segment top closest point (y=0), and the y axis is facing downwards.*

In both concepts an instrument housing was added around M3 and M4 in a manner so that there is always at least 10 mm clearance between the mirrors and the instrument housing. In the second concept the top

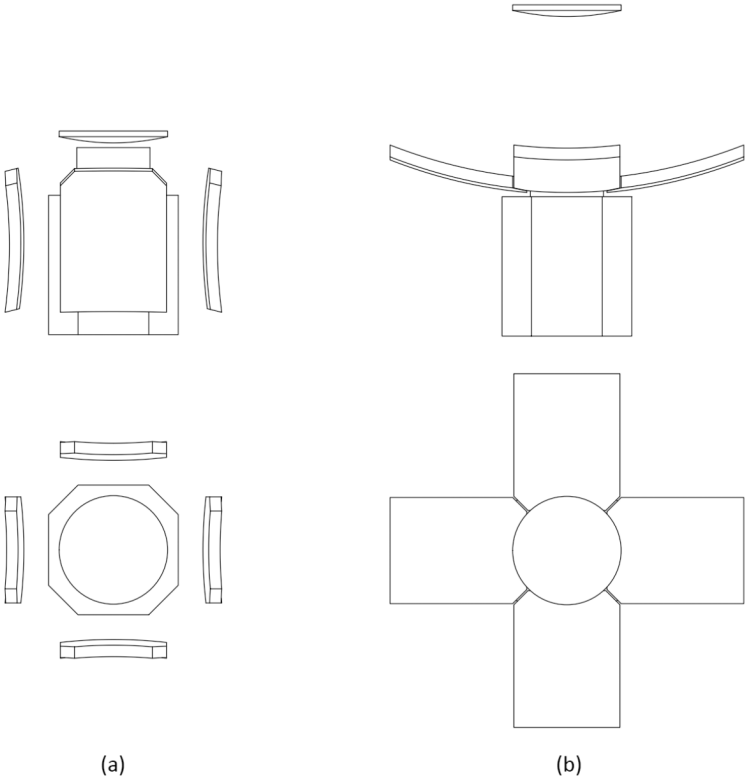

Figure 4.3: *Deployment concept adapted from the VIS DST. (a) Stowed, (b) deployed configuration.*

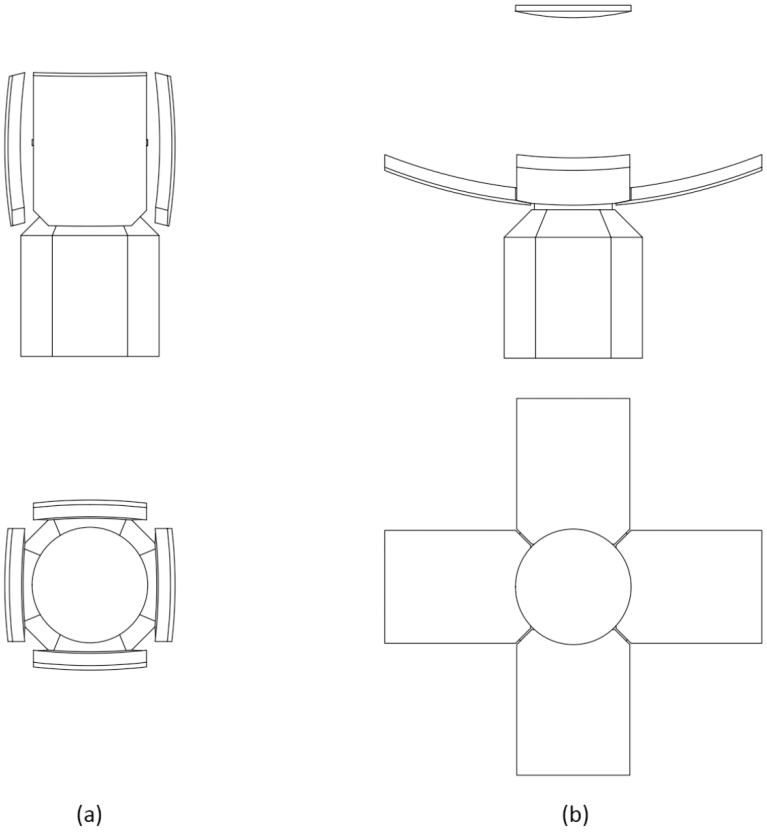

Figure 4.4: *Deployment concept to increase the free surface of the instrument housing. The hinge points of M1 segments are placed at (300,100), using the coordinate system of Figure 4.2. (a) Stowed, (b) deployed configuration.*

side of the instrument housing needed to be chamfered not to collide with the deploying M1 segments, see Figure 4.4.

Both concepts have advantages and disadvantages. The design with the upwards folding M1 segments has more instrument housing surface area for cooling, however, the stowed volume potentially increases with this design, and the legacy of years of VIS DST work is lost. The design with downwards folding M1 segments respects the VIS DST legacy with easily reusable design elements (M2 spider, M1 deployment), and could solve the cooling problem with transporting heat to another location in the spacecraft. Based on these and on feedback from the DST project team, the design with downwards folding M1 segments is selected to be further worked out.

4.1.4. Conceptual Telescope Design

In order to acquire the stowed and deployed dimensions of the TIR instrument, it requires more design details than the previously selected design concept has. To have the required details but not to spend too much time with the instrument design the VIS design elements are merged with the TIR mirrors. It means that the M2 spider, and the M1 support structure and deployment mechanisms have been added to the TIR downwards folding concept.

The M2 booms and the M2 deployment mechanism cannot be added to the TIR design because of the considerably different M1-M2 distance. Furthermore, the VIS SMSS has been proved to be incompatible with the baffle design (see Section 3.6.6), and its design was recommended to be revisited. Based on this, the TIR DST requires a new SMSS design that complies with the new M1-M2 distance and has reduced deployment radius.

The decreased M1-M2 distance however allows for linear deployment of M2, in contrast to the foldable booms used in the VIS design. Linear deployment is a solution to the problem of the high deployment radius of the VIS SMSS, and could possibly reduce the complexity of the M2 deployment system.

Based on the TIR mirrors, the adapted M2 spider and the adapted M1 support structure and deployment mechanisms, furthermore a linear M2 deployment mechanism a conceptual TIR telescope is designed that is visualized in Figure 4.5.

4.1.5. Difficulties

Changing the Deployable Space Telescope to TIR is a brave decision considering the years of work invested in the VIS design. The VIS design has already had budgets and requirements in place, and parts of the instrument worked out sometimes in multiple theses. Compared to this, the TIR design is in its infancy, however it enjoys more interest from external sources.

The lack of budgets and requirements puts the designers into a difficult position. To overcome this, wherever possible and logical, the VIS design is used as reference, and engineering intuition and common sense are utilized when coping with unknowns.

4.2. Radial Module Design

The baffle dimensions for the TIR DST need to be updated according to the TIR mirror dimensions. First, the radial module is designed, for which the calculations and design steps are analogous to the process described in Section 3.6.

Based on the dimensions of the conceptual TIR telescope design the geometrical constraints of the radial module can be revisited:

1. The spacecraft bus and the optical components of the stowed telescope fit in a circle with diameter of 1023.2 mm, but based on Section 3.6 the octagonal outline of the stowed M1 segments can be further approached. The greatest distance of the opposite sides in the octagonal outline is 968 mm. In the VIS design no clearance was defined between the stowed M1 and the stowed baffle, but for the TIR 5 mm clearance is chosen to ensure that the parts do not interfere with each other, not even during launch. 5 mm is an arbitrary number for now that is recommended to be checked in the future, or prescribed by a requirement. This means that the stowed inner diameter of the baffle must be greater than or equal to 978 mm (hard constraint).

2. In the current stage of the TIR DST project no requirement constrains the stowed volume of the baffle, but it is kept as small as reasonably possible. Consequently, there is no constraint on the outer stowed diameter.

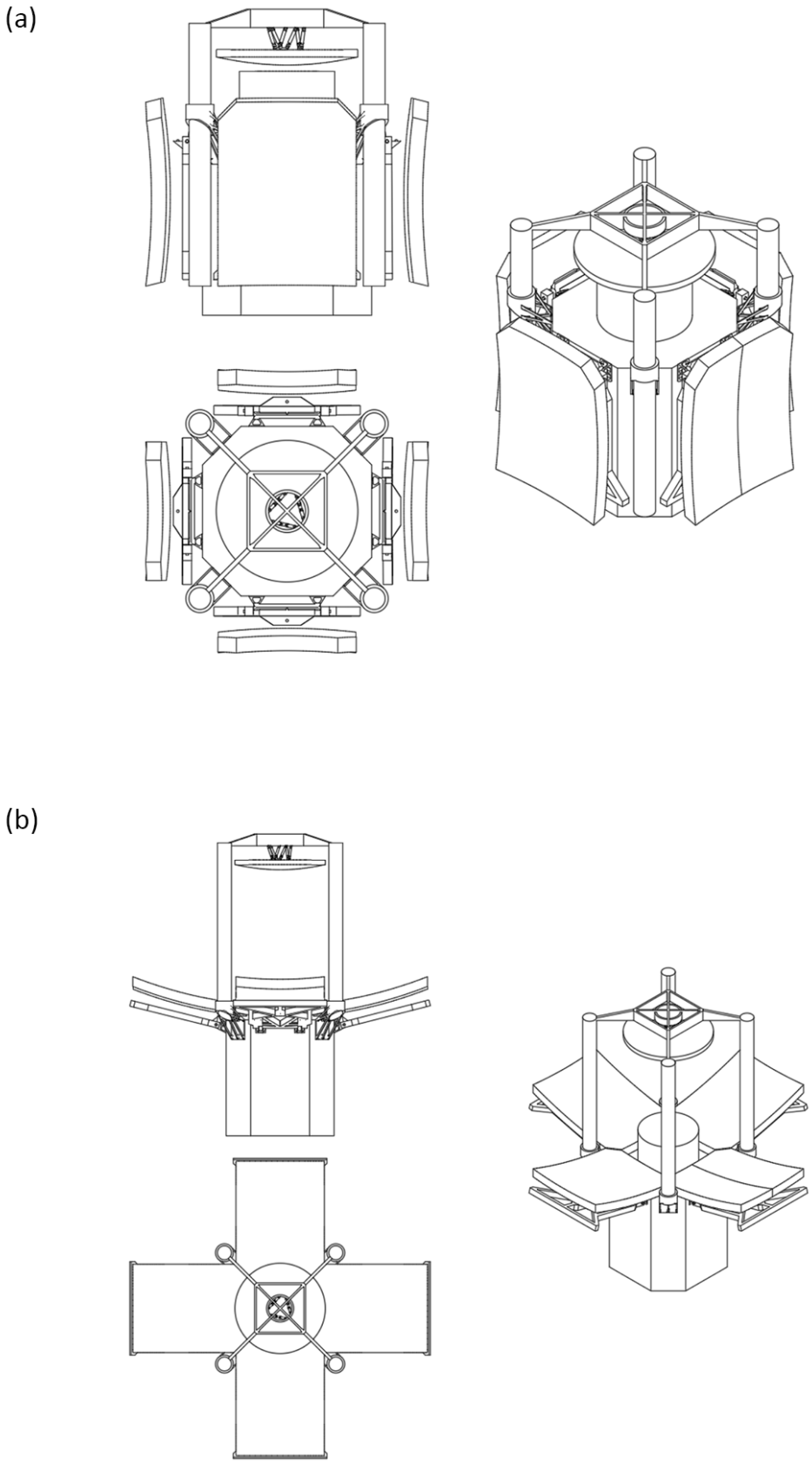

Figure 4.5: *Conceptual TIR telescope design in (a) stowed, (b) deployed configuration.*

3. The distance of the furthest sides of the deployed M1 segments is 1500 mm, to which the required 100 mm clearance (adapted from VIS) is added on both sides, which results in a minimal inner deployed diameter of 1700 mm (hard requirement).

4. For the outer deployed diameter there is no constraint, but as for the VIS, it is beneficial to keep it minimal as the atmospheric drag and the MMOI (that is important for the ADCS) increase with increasing outer diameter.

Using the updated constraints a preliminary pantographic module can be designed using the relationships presented in Section 3.6. The constraints of the VIS and the TIR DSTs are close to each other, consequently there are only minor changes in the radial modules, see Table 4.1. For the TIR preliminary design $w = 15$ mm arm width is used (same as for VIS) that is a good starting point. The arm width has only an insignificant effect on the module geometry, but plays an important role in the mass and stiffness of the structure (as presented before in Figure 3.35). At a later stage the arm width can be revisited to fine tune these two attributes. Because of the similarly sized modules, the number of straight arms remains $n = 3$.

The TIR preliminary pantographic module in its stowed and deployed configuration is visualized in Figure 4.6.

Table 4.1: *Comparison of the preliminary pantographic radial modules of VIS and TIR deployable baffles.*

	VIS	**TIR**
Inner diameter, stowed, mm	861	978
Outer diameter, stowed, mm	1233.9	1322.2
Inner diameter, deployed, mm	1773	1700
Outer diameter, deployed, mm	1966.1	1887.1
n	3	3
w, mm	15	15
L, mm	101.6	97.6
l, mm	182.0	174.7
Stowed θ, degree	36.8	46.5

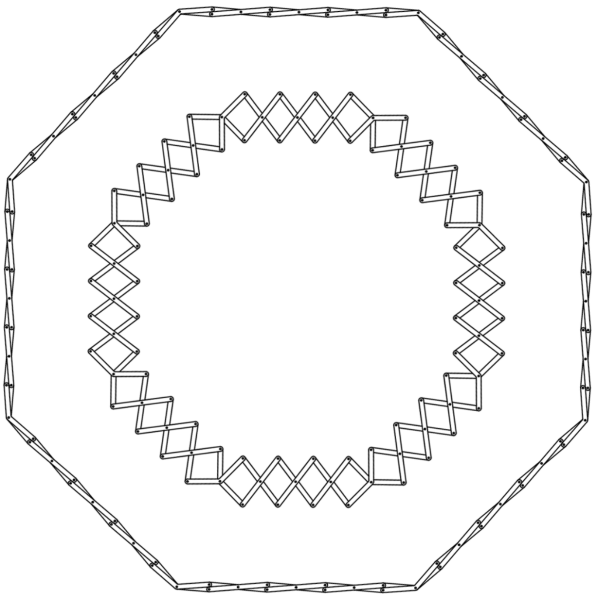

Figure 4.6: *The TIR preliminary pantographic module in its stowed (inside) and deployed configuration (outside). The configurations are to scale to each other.*

4.3. Preliminary Thermal Design

With the radial module design ready, the next step in the mechanical design of the baffle would be the design of the axial module. However, changing to TIR practically reset the available design inputs, including the required height of the baffle, without which the axial module cannot be designed. Therefore, the point of this section is to find the optimal baffle height of the TIR DST with thermal analyses. As no thermal analysis existed for the TIR design before, the preliminary thermal behavior of the TIR DST is presented as well.

4.3.1. Change to TIR

ESATAN-TMS has been used previously as the primary thermal modelling software in the DST project, and is used in this thesis as well. ESATAN-TMS offers geometric modelling, radiative coupling calculation, thermal model creation and solution in one software [29].

Previous thermal models have been available from Akkerhuis [3] that were useful for reusing certain geometries, orbital parameters, material and optical properties, among others. However, all past designs were made for the VIS DST, so even the latest design from Akkerhuis was already obsolete. On the other hand, the geometries available is the design could be modified to be corresponding to the TIR DST, meanwhile keeping the defined bulk materials and optical properties.

Changing the model to TIR brought the need for the decision what parts of the telescope to model in ESATAN. The VIS model was fairly developed, with modelled parts including M1, M2, PMSS, SMSS, instrument housing, sensor, and baffle. From these, only the mirror geometries were available for the TIR telescope. A baffle and an instrument housing are required for the appropriate modelling of the thermal environment inside the baffle. There is no information available for the PMSS ans SMSS for the TIR DST, so the decision has been made to exclude these geometries from the current TIR design as there is no point to model something that is definitely going to be redesigned later, and keep this TIR design as a preliminary thermal study that can be updated later with the redesigned additional parts.

As no material properties were available for the TIR mirrors, it is assumed that its material and overall density equals to the ones in the VIS design. Another assumption was made, namely that the TIR DST's M2 has a cross-shape similar to the one in the VIS design. Based on the latest optical design that includes ray-tracing [14], a symmetrical cross-shape with 138 mm arm width and 460 mm arm length could reflect all the expected light coming from M1. However, to ascertain whether the assumption is valid, further optical studies are recommended.

The instrument housing has been reused from the VIS design as well, but has been made larger to be able to accommodate the bigger TIR mirrors. No information was available on the size of the field stop, so as a preliminary design decision, an 80 x 80 mm rectangular cutout has been made on the top of the instrument housing, see Figure 4.7. When more information is available, this cutout needs to be redesigned.

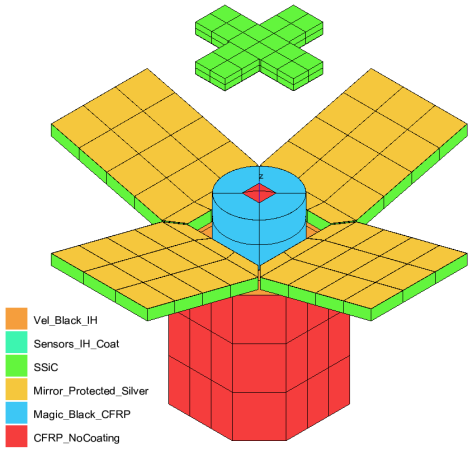

Figure 4.7: *TIR ESATAN model with the thermo-optical properties of the surfaces (without baffle).*

To mimic the real-life structure of the mirrors, the M1 and M2 geometries are modelled with 1 mm thick full-density SiC layer on the reflective sides of the mirrors, meanwhile having a reduced-density SiC layer that fills up the rest of the geometries (analogously to Akkerhuis' design [3]). The reduced-density layer accounts for the triangular cutouts in the mirrors that were made to lighten the structure. Changing the mirrors from

VIS to TIR while keeping their overall densities resulted in masses of 22.6 kg for M1 (including all four segments) and 3.9 kg for the M2. Adjustment of the masses when more information is available is recommended.

The baffle is designed as an octagonal shell in ESATAN, similarly to Akkerhuis' model [3]. The diameter of the baffle has been calculated in the previous section, and from the many diameters its external deployed diameter is used in the thermal analysis program. The height of the baffle is yet unknown, hence multiple thermal cases with different baffle heights are analyzed, and the optimal one is selected. Furthermore, thermal cases without baffle are inspected as well in order to set up a baseline for the baffle effectiveness. The optical and material properties of the baffle are kept as designed by Akkerhuis [3] as a first iteration.

4.3.2. Verification

Many changes have been applied to the VIS thermal model to create the TIR model, therefore it needs to be verified. The steps of verification are analogous to the thermal verification Akkerhuis performed [3].

Thermal calculations in ESATAN include two steps. First, the radiative case is executed, which calculates the radiative exchange factors of the different surfaces and nodes. The radiative exchange factors depend on the shape, the orientation, and the coating of the surfaces. The shapes and orientations can be checked in ESATAN's GUI, and ESATAN can display the applied coatings on the surfaces, therefore they can be visually verified, too. Arink verified that the radiative exchange factors calculated by ESATAN are analogous to the analytical calculations [5].

The second part of the thermal calculations performed by ESATAN is the analysis case. In this case the heat exchange is calculated between the nodes at every time step. The heat exchange consists of the applied heat sources, and the radiative and conductive heat exchanges, and are calculated from the radiative exchange factors, the conductive couplings, and the node temperatures. The transient solution calculates the temperatures of the nodes T_{i+1} based on their temperatures at the previous time step T_i, their net heat balance Q_i, their thermal mass (or as ESATAN calls them, capacitance) mc_p, and the time step Δt:

$$T_{i+1} = T_i + \frac{Q_i}{mc_p} \cdot \Delta t \tag{4.1}$$

The temperature profiles given by Equation (4.1) are just first-order approximations as it assumes constant heat exchange over the time period Δt, but with fine temporal resolution the results are close to real values.

The net heat balance and temperatures can be easily exported from ESATAN for any node, surface, geometry, or group, but checking the capacitances are just available on nodal basis. This makes the validation of complex geometries difficult, however, the temperate profiles exported from ESATAN can be compared against the analytically estimated temperature profiles (using Equation (4.1)), therefore validating the capacitances as well. The calculated temperature profiles use calculated capacitances from the same input data that has been given to ESATAN.

The comparison of the analytically calculated temperatures profiles and profiles exported from ESATAN is presented in Figure 4.8. The temperature profiles of the sensors practically coincide with each other, therefore verifying the sensor part of the model. For the instrument housing the profiles are similar and close to each other, and is acceptable as a first-order approximation. However, the exported and calculated temperature profiles of the mirrors are far from each other, consequently raising a flag that there is a problem with the definition of those geometries. The shapes of the exported and calculated mirror profiles are similar, indicating that the problem probably lies with the capacitances, namely ESATAN associated considerably greater capacitances to the mirrors than it was supposed to, practically minimizing the temperature change through an orbit.

The ESATAN input data has been checked multiple times, yet the source of the problem could not be found. Then, by gradually excluding every possible source of the problem, a difference has been found in the definition of the mirrors and the verified geometries (sensors, instrument housing): the verified parts are made of shell-type geometries, meanwhile the mirrors were defined as solid bodies. Akkerhuis already stated that ESATAN has problems with solid geometries, hence he modelled the rods in the SMSS as thin-walled structures (shells) [3]. However, it looks like that the rest of the geometries defined as solids has never been checked for similar issues.

In order to check if indeed the solid structure is the source of the problem, the mirrors have been remodelled as shells. There are five possible solutions to change the solid mirrors to shells, see Figure 4.9, where they are presented with an M1 segment. The solid geometry consists of one full-density top geometry, and a reduced density bottom geometry (Figure 4.9a). With two shells the solid geometry can be mimicked well,

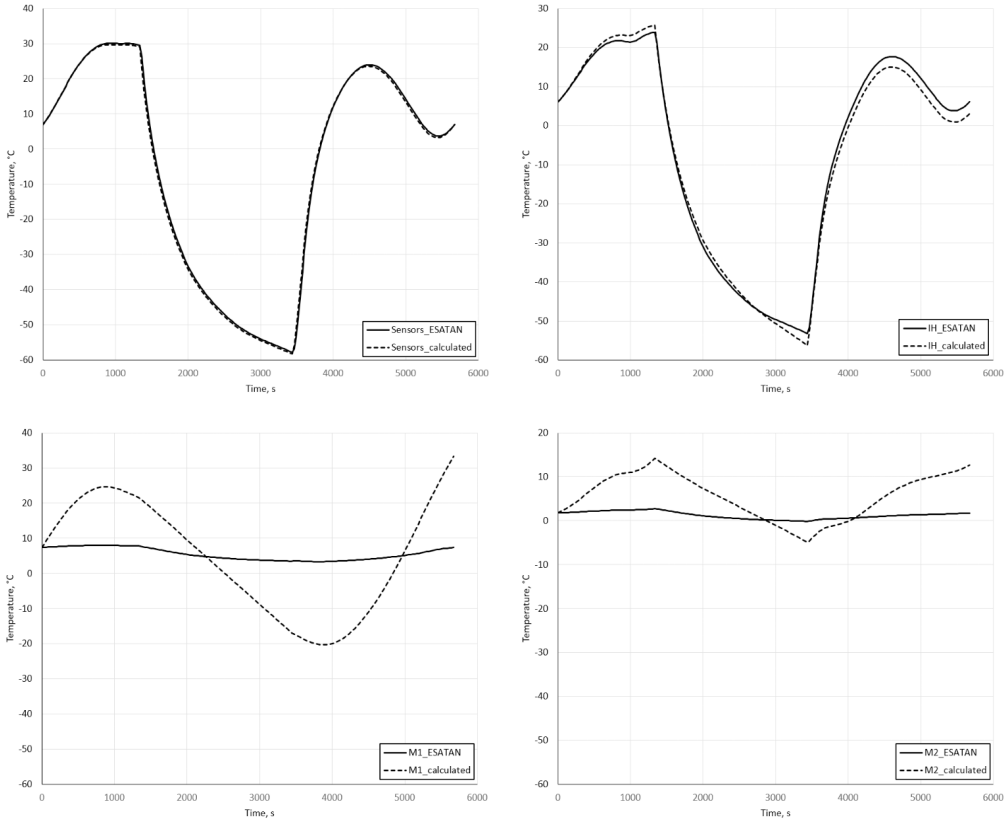

Figure 4.8: *Comparison of the exported and calculated temperatures profiles of the sensors (top left), instrument housing (top right), M1 (bottom left), and M2 (bottom right).*

with the original thicknesses of the solids given as inputs for the shell definitions. Three solutions are possible based on which surfaces are kept: in solution (b) the top and in (c) the bottom surfaces are kept, meanwhile having a small gap between the shells to avoid deceptive definitions and to define the vertical buildup. The third solution (d) keeps the top and bottom surfaces at their original locations, but has a gap between the shells that is equal to the original thickness of the mirror. With one shell two solutions are possible: to keep the original top (e) or bottom surface (f).

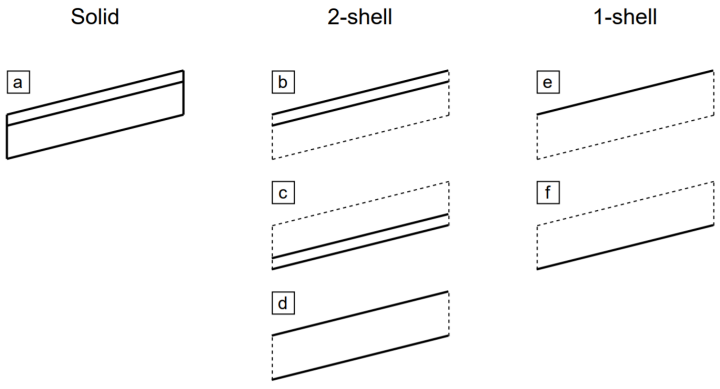

Figure 4.9: *Possible solutions of converting the solid M1 segments (a) to shells (b-f).*

The 2-shell solutions have the advantage of keeping the dual structure of the mirrors, therefore better representing the real life than the 1-shell solutions. However, having gaps between the surfaces introduces additional radiative couplings between the geometries of the instrument. Some couplings can be eliminated by defining the activity of mirror surfaces facing the gap as conductive in ESATAN, hence inhibiting them to take part in any conductive coupling, but the gap is see-through, making it available for other geometries to

form couplings through the gap. This problem is increased for solution (d). The conduction between the two shells needs to be defined with contact zones in ESATAN, with required input of contact conductance, but the value of that is unknown, therefore it introduces uncertainty to the results.

The common disadvantage of all the shell solutions but (d) that some of the original mirror surfaces are lost, hence altering the radiative couplings within the telescope. The 1-shell solutions represent the mirrors with only one shell, consequently losing the dual structure of the mirrors. The missing volume of the original mirror appears as a see-through gap, changing the couplings again.

Considering that the current thermal model is only a preliminary one, solution (e) has been selected to represent the mirrors as shells. The 1-shell structure reduces the complexity of the model, and the top surfaces (closer to Earth) of the mirrors are kept. With this solution, the shells are further out towards the opening of the baffle (compared to solution (f)), therefore accurately representing the possible Sun exposures. This is true for M1 and M2 as well. Because of the altered geometry definition, the bulk material properties and the optical properties of the geometries need to be changed. For more detailed thermal analyses it is recommended to return to this trade-off and examine the outcome with the different solutions more thoroughly.

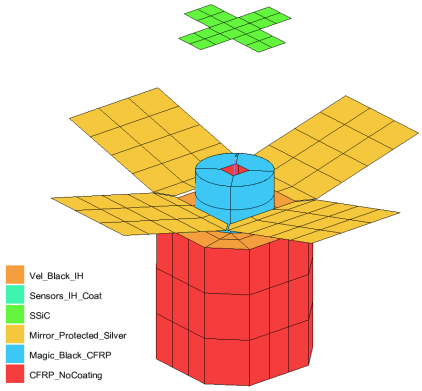

Figure 4.10: *Thermo optical properties of the surfaces of the ESATAN model with the mirrors defined as shells.*

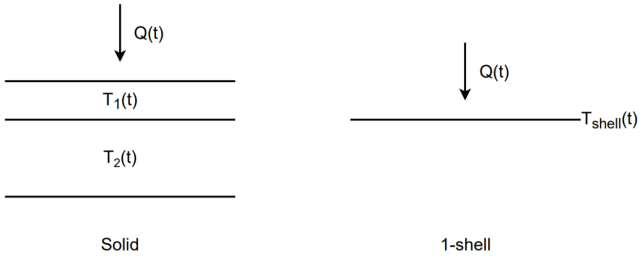

Figure 4.11: *Cross-section of the solid (left) and 1-shell (right) models for the dynamic behavior verification.*

With the mirrors redefined as shells (see Figure 4.10), the analytically calculated temperatures profiles and profiles exported from ESATAN are compared again in Figure 4.12. It shows that the updated mirror definitions solved the problem, and the M1, M2, and sensors exported temperature profiles follow the profiles produced by analytical calculations. There is a slight difference between the profiles of the instrument housing, which is the most complex geometry of all, including multiple cutouts, user defined conductors, and inactive optical surfaces. The difference between the profiles is considered negligible, therefore the thermal model is verified.

The simplification of a geometry consisting of two solids to a single shell might raise some concerns regarding its dynamic behavior to heat input, and the temporal temperature profiles of the nodes. To check the possible differences, two simple models have been defined. Both models include an infinite plane of M1 segment excited by a sinusoidal heat flux $Q(t)$ arriving perpendicular to the surface, with period of 600 s, and maximal and minimal incident heat flux of 1350 and 0 W/m^2, respectively:

$$Q(t) = \frac{1350}{2} + \frac{1350}{2} \cos \frac{2\pi t}{600}$$

The geometries are assumed to be in radiative coupling with free space on both sides of the M1 segments. The cross-sections of the segments are presented in Figure 4.11, and the material properties and thicknesses are perfectly aligned with the TIR DST solid and 1-shell models. Having only one node per geometry in the direction normal to the surface in ESATAN greatly simplified the modelling of the heat flow. The results are presented in Figure 4.13, starting from a temperature close to the quasi-equilibrium temperature of the models. The differences of temperatures between the models are negligible, and capacitance-weighted average temperature of the solid model perfectly coincides with the temperature profile of the shell. The temperature differences are negligible with other initial temperatures as well, a temperature close to the quasi-equilibrium temperate was chosen as the initial temperature solely for visualization purposes, otherwise the temperature

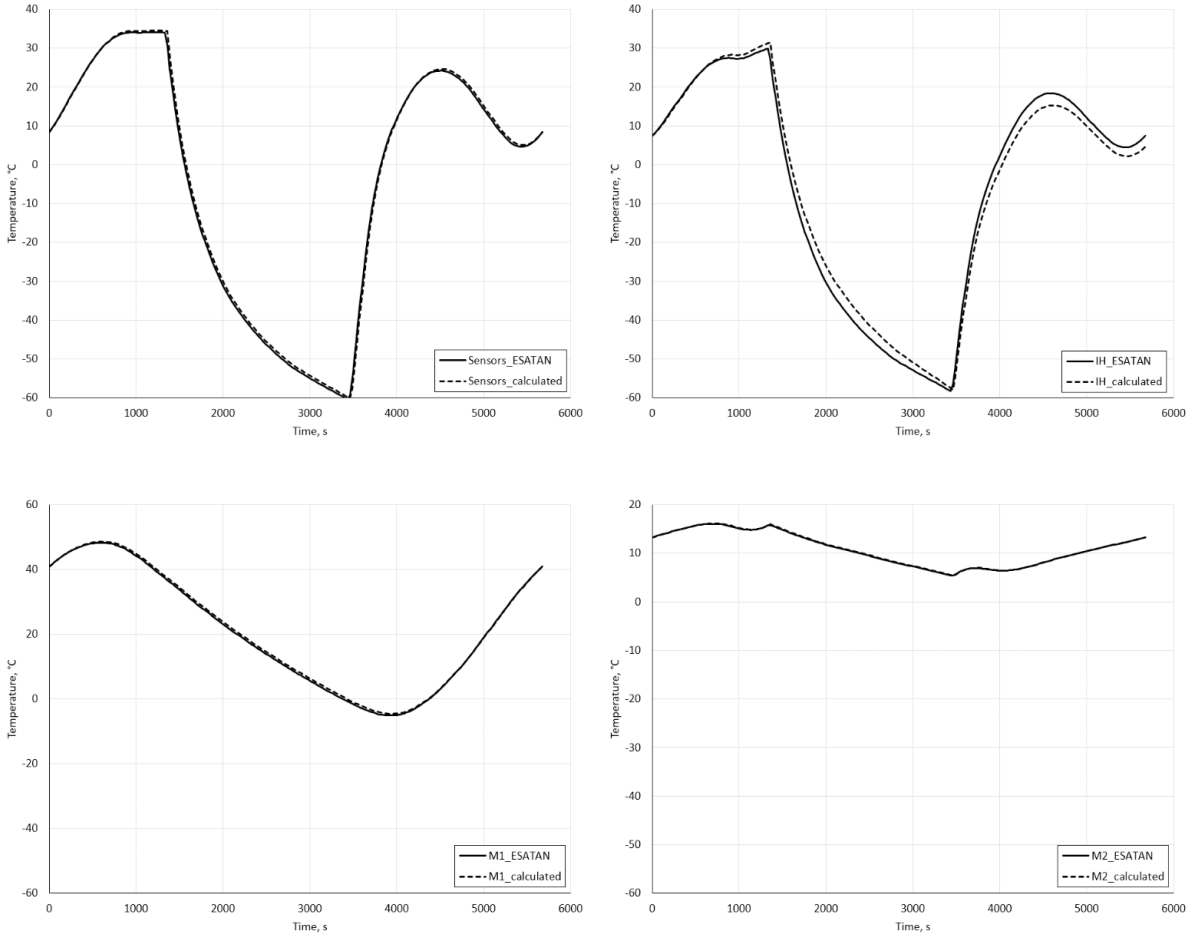

Figure 4.12: *Comparison of the exported and calculated temperature profiles of the sensors (top left), instrument housing (top right), M1 (bottom left), and M2 (bottom right), with the mirrors redefined as shells.*

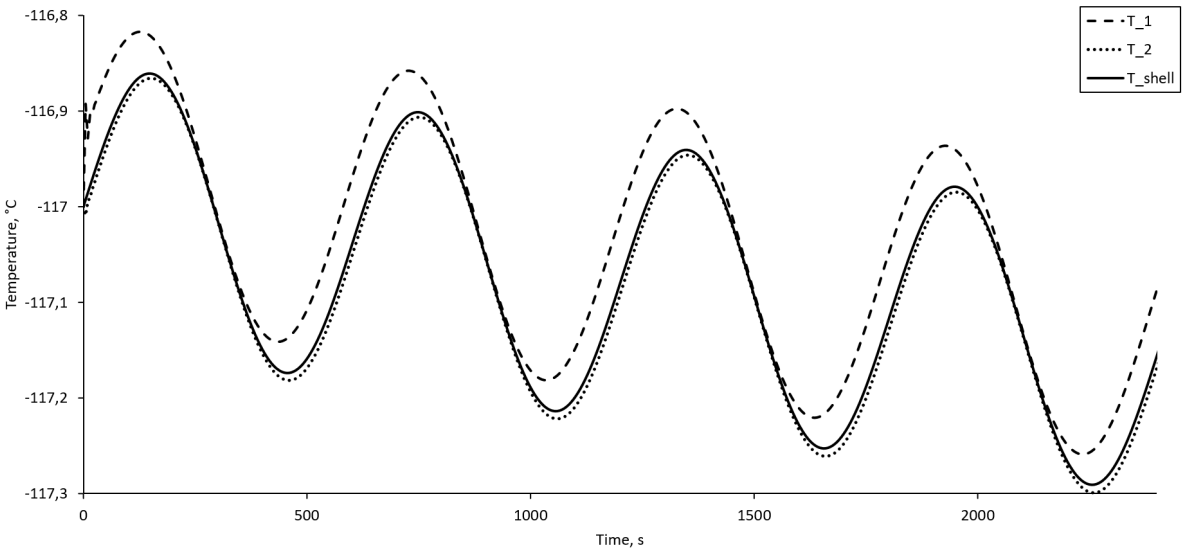

Figure 4.13: *Temperature profile of the geometries in Figure 4.11.*

Table 4.2: *Changing the emissivity and absorptivity of SSiC in the thermal model.*

	Emissivity	Absorptivity	Reference
VIS	0.05	0.234	[48]
TIR	0.7	0.8	[8, 32]

differences between the models would not have been visible. The models verify that the 1-shell simplification of the mirrors is a viable method to avoid the errors in the ESATAN solid mirror thermal calculations.

Using solid geometries in ESATAN has been found problematic not only by this study, but before in Akkerhuis' thesis as well. According to Akkerhuis a finer mesh resolution for the solid geometries solves the problem, but increases the calculation time substantially [3]. It is recommended to validate the solid geometry definitions (with particular attention to their capacitances) in all past and future studies before using the results of those studies for decision-making.

4.3.3. Summary of Changes

Apart from the changes in geometry, there has been some additional modifications while changing the VIS DST design to TIR in ESATAN. The emissivity and absorptivity of SSiC (sintered silicon carbide - bulk material of the mirrors) has been changed according to Table 4.2 to more realistic values.

The mirrors defined in ESATAN do not have the right shapes to perfectly model the real optical path, consequently the heat is not realistically distributed in the telescope. To cope with this, Akkerhuis introduced perfect black frontal surfaces to the M1 segments, and manually distributed its incoming heat among M1, M2, field stop, and sensors by defining heat sources and sinks (for further information see Section 4.2.5 in Akkerhuis' thesis [3]). For now, the coating of the active mirror surfaces is changed to protected silver (α = 0.035, ε = 0.035), the same coating that has been defined for the reflective surface of the M2 in the VIS design, and the heat sources and sinks have been disabled.

The final inputs for the shell mirrors are presented in Table 4.3. The effective bulk material properties are used to account for the lightened structure of the mirrors. The density of SSiC is 3150 kg/m^3, its thermal conductivity is 180 W/mK [32]. In Akkerhuis' model the conductivity was 142 W/mK [3]. While defining effective bulk material properties, Akkerhuis not only decreased the density and conductivity, but also the specific heat, which was a double penalization for the thermal mass (capacitance). The specific heat is kept at its original value of 680 J/kgK in the TIR design.

Table 4.3: *Bulk properties of the M1 segments and M2. The last three rows were used as ESATAN inputs.*

	M1 segment	M2
Mass, kg	5.65	3.9
Volume, m^3	0.0125	0.0054
Effective density, kg/m^3	453.72	723.21
Effective thermal conductivity, W/mK	25.93	41.33
Specific heat, J/kgK	680	680

4.3.4. Detector Heat Load

Akkerhuis introduced heat sources and sinks to redistribute the radiation impinging on the M1 segments to account for the mirror modelling errors (flat vs. spherical) [3]. Ultimately, 46.5% of the said radiation was redirected to the inside of the instrument housing as a heat source, and another 46.5% to the field stop, however, no rationale was added why the redistribution was done this way. On the other hand, there was an assumption that is questionable: "all radiation reflected by the primary mirror reaches the secondary mirror". A more realistic approach is introduced instead: the majority of the radiation that is reflected from the M1 segments and impinging on the M2 is coming from FOV of the telescope, and ultimately only the radiation from the FOV reaches the detector. This is considered to be much less than the 46.5% assumed by Akkerhuis. In this section the theoretical heat load of the detector is calculated, then based on this it is decided if heat redistribution in ESATAN is required or not.

To calculate the heat load of the detector the following are assumed:

- The calculation is made for Earth IR radiation.

- Only the radiation coming from the field of view (FOV) of the telescope reaches the detector, the rest of the Earth IR radiation is redirected elsewhere along the optical path of the telescope.
- Flat Earth is considered, with a coaxial parallel disc as the primary mirror. The flat Earth simplification introduces a maximum of 11% of view factor increase from M1 to Earth (full Earth view), but it is considerably lower when only the telescope FOV is considered [1].
- The distance between the two discs is $h = 500$ km (orbit height), the M1 disc diameter is 1.5 m, the FOV disc diameter is 5 km (swath width of the VIS DST – without precise TIR data, it is considered to be the same as VIS).
- Earth temperature is $T = 263.5$ K (highest temperature taken from Table 4.8 to account for the worst case scenario).
- Both discs are black surfaces.

The heat exchange between the Earth FOV disc and the M1 disc:

$$Q = F_{FOV-M1} \cdot A_{FOV} \cdot \sigma T^4 = 19.5\ mW \tag{4.2}$$

where F_{FOV-M1} is the view factor between the Earth FOV disc and the M1 disc [1], A_{FOV} is the surface of the Earth FOV disc, σ is the Stefan-Boltzmann constant. The resulting 19.5 mW heat load is calculated for IR radiation, and with albedo the expected result is approximately the double of it (albedo average: $0.33 \cdot 1366 = 451$ W/m^2, Earth IR average: 230 W/m^2 [16]). In the comparison average values are considered, as the extremes do not happen at the same location: high albedo happens at areas with high clouds and/or icecaps, while high Earth IR radiation originates from areas with high temperature.

Even with IR and albedo combined, and considering the introduced errors with the simplified model, the detector heat load (considered as heat load on M1 coming from the optical FOV) is well below 1 W, and considered to be negligible (the Earth IR radiation is ≈ 198 W/m^2 on average at 500 km orbit height [16], and the diameter of M1 is 1.5 m), making it undesirable to redistribute the heat as Akkerhuis did in his thesis.

4.3.5. Mirror Modelling Errors

In the previous section it has been shown that there is no need to redistribute heat to the detector in the thermal analyses to account for the right shape of the mirrors. However, the rest of the telescope, with emphasis on the baffle, is yet to be checked.

From optical point of view the shape of the mirrors play a crucial role in ensuring optimal imaging quality. On the other hand, in thermal calculations and studies it is often difficult to model the exact shape of the mirrors, introducing errors in the view factors among the telescope geometries, and altering the route of the rays. In this section the magnitude of the errors is studied introduced by replacing the spherical mirrors by flat mirrors.

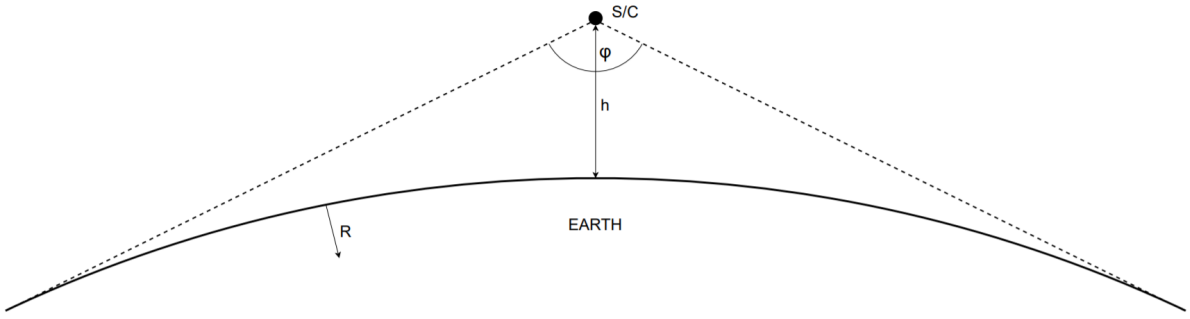

Figure 4.14: *Angular extension of Earth seen by the telescope.*

A simple 2D ray-tracing model is introduced to assess the effect of mirror shape to the baffle, see Figure 4.15a. Flat Earth assumption is used with orbit height of $h = 500$ km. The telescope is represented by the baffle with baffle height h_b and two symmetrical primary mirror segments. The origin of the reference frame is placed at the intersection of the optical axis of the telescope and the Earth surface. Because of the symmetry of the model only the positive x-coordinates are considered. The ray-tracing is done the following way: the line bound by the origin and the end of Earth at $x = 1238$ km (based on the view angle in Figure 4.14) is divided into n_x equally spaced points. From each point the bounding angles are calculated under which

the telescope is visible. Then, the angle between the bounding angles is divided into n_{rays} equally spaced angles. All the rays shot from the n_x points at their respective calculated angles hit the telescope, however, the distinction is made based on which part of the telescope they hit.

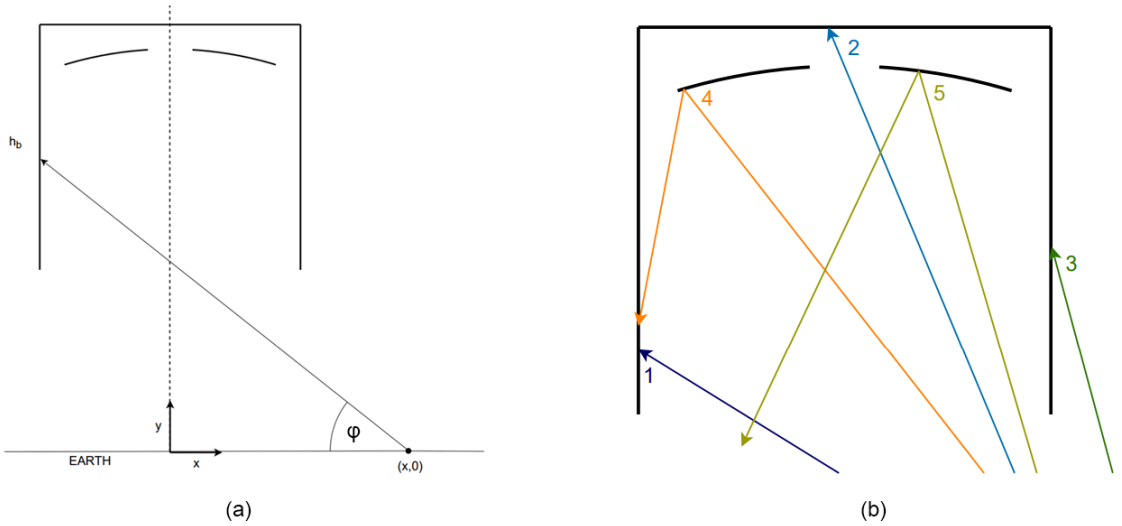

Figure 4.15: *(a) Model layout for ray-tracing. (b) Possible interactions of the rays with the telescope.*

Figure 4.15b presents the possible ways the rays can interact with the telescope, studied from the reference of the baffle:

1. A ray hits the inner side of the baffle.
2. A ray hits the bottom side of the baffle.
3. A ray hits the outer side of the baffle.
4. A ray hits the primary mirror, gets reflected, and hits the inner side of the baffle.
5. A ray hits the primary mirror, gets reflected, and leaves the telescope.

To keep the model fairly simple, reflections were only considered if the rays hit the mirror. The flat and spherical mirrors share the same endpoints in the model (coming from the optical design [14]). In the flat model the endpoints are connected with a straight line, meanwhile in the spherical model the endpoints are connected with an arc, while keeping the center of the arc on the optical axis. In a Matlab script the n_x x n_{rays} rays were traced for both models, and collected how they reacted with the telescope (based on the list above). The results are visualized in Figure 4.16 with $n_x = 1239$ Earth surface points placed on the x-axis, and the $n_{rays} = 1000$ rays on the y-axis, starting from smaller (1) to higher (1000) φ angles. To present the effect of the baffle height, the figure shows the results with $h_b = 1.5$ m and 5 m high baffles as well.

The differences between the two mirror shapes only appear at fields 4 and 5, as expected. With increasing x less and less rays get in contact with the mirrors, and after a certain distance only the baffle sides are visible (fields 1 and 3).

With the 2D half-plane ray-tracing the resulting distribution of rays is representative for the full plane as well because of the symmetry of the model. However, the 2D distribution of rays is not representative for a quasi-3D case (2D ray-tracing model revolved around the optical axis) as with increasing x distance from the origin the amount of points increase by x^2. The outcome of the 2D ray-tracing is converted into quasi-3D using the following equation, also considering that the primary mirror has cutouts:

$$N_j = \left(a \cdot \sum_{i=1}^{n_x} M_j(x_i) + (1-a) \cdot \sum_{i=1}^{n_x} L_j(x_i) \right) \cdot \left(x_i^2 - x_{i-1}^2 \right) \tag{4.3}$$

where N_j is the amount of rays hitting the telescope with j interaction in the quasi-3D model, $a = 0.6181$ is the surface ratio of the M1 with and without cutouts, $M_j(x_i)$ is the amount of rays hitting the telescope from point x_i with j interaction in the half-plane 2D model, and $L_j(x_i)$ is the amount of rays hitting the telescope from point x_i with j interaction in the half-plane 2D model without a mirror. The resulting numbers are not to be interpreted on their own, but as relative results compared to each other.

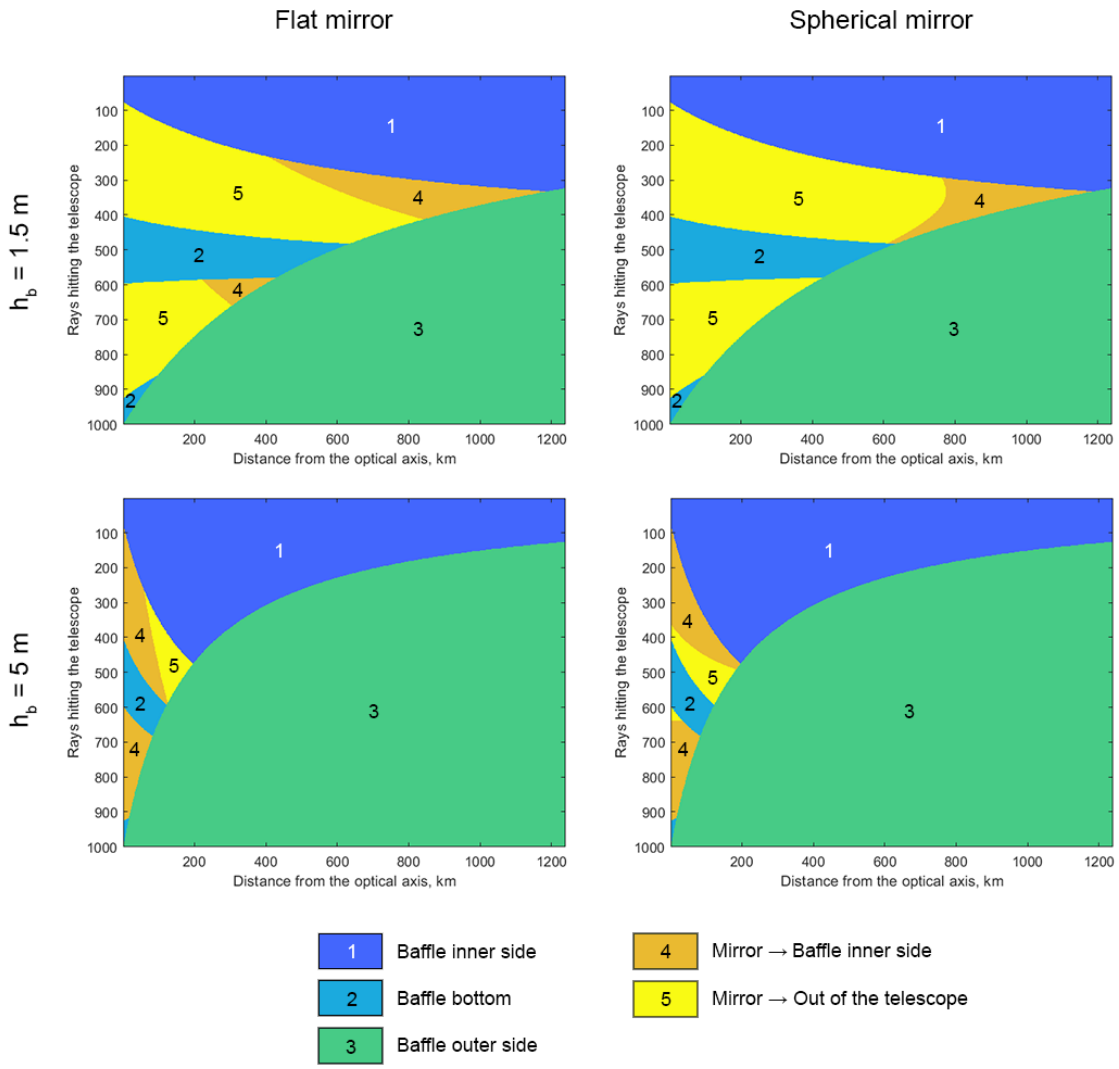

Figure 4.16: *Results of the ray-tracing model with flat and spherical mirrors, and two different baffle heights.*

Furthermore, from the baffle point of view the different interactions add different amount of heat to the baffle. The heat addition of the different interactions are shown in Table 4.4. The heat additions are based on the interacting surfaces' IR emissivity, which is the ratio of the incoming radiation that is absorbed by the surface. When a ray hits the mirror, gets reflected and then absorbed in the inner part of the baffle, $0.965 \cdot 0.84 = 0.81$ is used, where 0.965 is the reflectivity of the mirror. The emissivities and reflectivities are from Akkerhuis' design [3].

Based on these, the heat absorbed in the baffle E can be quantified:

$$E = \sum_{j=1}^{5} N_j \cdot e_j \tag{4.4}$$

where e_j is the heat addition of a j interaction, listed in Table 4.4. Table 4.5 shows the ratios of different interactions in the 2D and the quasi-3D model for $h_b = 1.5$ m, and ratio of heat additions that different interactions impart to the baffle.

Ultimately the amount of heat imparted to the baffle is the metric that counts, hence the total heat absorption of the baffle with flat and spherical mirrors are compared with different baffle heights. The results are presented in Table 4.6. With low baffle heights the amount of heat absorbed by the baffle is slightly different with spherical and flat mirrors, but as soon as a sensible (the baffle at least covers the secondary mirror: $h_b \geq\approx 1.5$ m) baffle height is reached the difference reduces to under 2%. It is foreseen that the baffle height is going to be higher than 1.5 m, therefore the differences between the flat and spherical mirrors are going

Table 4.4: *Heat addition of the rays to the baffle based on their interaction.*

No.	Description	Heat addition
1	Baffle inner side	0.84
2	Baffle bottom	0.84
3	Baffle outer side	0.14
4	Mirror → Baffle inner side	0.81
5	Mirror → Out of the telescope	0

Table 4.5: *Ratio of different interaction between the rays and the telescope (with h_b = 1.5 m) in 2D and quasi-3D models, and the ratio of the heat imparted to the baffle by different interactions.*

	2D ray-tracing		Quasi-3D ray-tracing		Heat addition	
No.	Spherical	Flat	Spherical	Flat	Spherical	Flat
1	25.2%	25.2%	32.7%	32.7%	68.8%	67.6%
2	6.1%	6.1%	3.4%	3.4%	7.1%	7.0%
3	46.1%	46.1%	56.1%	56.1%	19.7%	19.3%
4	2.5%	4.3%	2.2%	3.1%	4.5%	6.1%
5	19.9%	18.1%	5.6%	4.7%	0.0%	0.0%

to be lower than 2%. With these amount of differences the flat mirrors are safe to be used in the preliminary thermal studies instead of the spherical ones, and the flat representation of the mirrors in ESATAN does not introduce considerable inaccuracies.

Table 4.6: *Comparison of the heat imparted to the baffle in models with flat and spherical mirrors, and different baffle heights.*

Baffle height, m	1	1.25	1.5	1.75	2	2.25	2.5	2.75	3	3.25	3.5	3.75	4
E_{flat}/E_{spher}	1.0173	1.0389	1.0175	1.0153	1.0152	1.0098	1.0053	1.0028	1.0012	1.0003	0.9997	0.9995	0.9993

In this study no differentiation was made for the type of radiation coming from Earth: it can be Earth IR or albedo, as far as its properties are uniform at each Earth point. For the heat additions the IR emissivities were considered, but the applied materials' solar absorptivities are close to the used values as well. The M2 is missing from the study as it is meant to be kept as a simple ray-tracing analysis, and the M2 is not expected to change the outcome of the study substantially. The 3D study is called quasi-3D ray-tracing as it only considers rays of which the planes include the optical axis. Furthermore, this study does not differentiate on where exactly the rays hit the baffle. If exact location of the hits (for example to check the spatial distribution of the heat absorbed by the baffle) or actual 3D ray-tracing is required with more included parts, it is recommended to redo the study with a 3D model from the start, and the usage of a ray-tracing software is advised.

4.3.6. Seasonal Differences

In this section the seasonal differences in DST temperatures are checked. The seasonal changes affect the following attributes of the radiative environment:

1. **Sun angle.** The tilt of the Earth's spin axis coupled with the Earth's orbit around the Sun constantly changes the latitude of the sub-solar point. The Sun Angle changes between -23.44° and 23.44°, taking its minimal value at winter solstice, its maximal value at summer solstice, and 0° at vernal and autumnal equinox.

2. **Earth albedo.** The albedo of the Earth varies greatly with location and time, hence averaged values are used for the study. 5-year monthly datasets are used from the CERES-program, organized in 10° belts by Peyrou-Lauga [40], see Table 4.7.

3. **Earth temperature.** Similarly to albedo, Earth temperatures are used in monthly averages and 10° belts given by Peyrou-Lauga [40], see Table 4.8.

4. **Sun-Earth distance.** Because of the slightly elliptical orbit of Earth, the Sun-Earth distance constantly changes. The perihelion is in winter with 147.1 million km, and the aphelion is in summer with 152.6

million km, and during equinoxes the Earth-Sun distance is 149.6 million km. For simplicity, it is assumed that peri- and aphelion happens at solstices.

Table 4.7: *Albedo values at different latitudes in different months [40].*

Lat.	March	June	September	December
-90°	0.69	0.8	0.72	0.67
-80°	0.67	0.76	0.71	0.655
-70°	0.58	0.665	0.655	0.575
-60°	0.465	0.56	0.525	0.455
-50°	0.385	0.46	0.395	0.365
-40°	0.305	0.37	0.32	0.295
-30°	0.24	0.295	0.26	0.245
-20°	0.215	0.235	0.22	0.23
-10°	0.215	0.21	0.21	0.23
0°	0.22	0.235	0.23	0.24
10°	0.21	0.245	0.25	0.24
20°	0.225	0.235	0.245	0.255
30°	0.285	0.255	0.25	0.32
40°	0.35	0.295	0.28	0.405
50°	0.41	0.335	0.335	0.48
60°	0.485	0.365	0.395	0.55
70°	0.575	0.435	0.455	0.625
80°	0.63	0.53	0.535	0.69
90°	0.64	0.57	0.58	0.72

Table 4.8: *Temperatures (in K) at different latitudes in different months [40].*

Lat.	March	June	September	December
-90°	229	219	219	242
-80°	232	222	222.5	242.5
-70°	239.5	231	232	244.5
-60°	246	240.5	241	247.5
-50°	250.5	246.5	246.5	251
-40°	256	251.5	252	255.5
-30°	260.5	257	258.5	259
-20°	260.5	262.5	263.5	259
-10°	257	263	263	257.5
0°	256.5	257.5	258	257
10°	261.5	256	255.5	260
20°	263.5	260	259	262
30°	257.5	260.5	261.5	256.5
40°	250	257.5	259	249
50°	245.5	254.5	254	244
60°	242.5	253	250	239.5
70°	239	252	248	236.5
80°	236	251	246	235
90°	235	251	245	234

The different sun angles, Earth albedos and temperatures, and Sun-Earth distances have been used as inputs in ESATAN, and four different studies have been made: one for December, March, June, and September each. The month names actually represent the respective equinoxes and solstices. The studies were run with 1.5 m high baffle, 1 mm baffle thickness, and baffle through-conductance values inherited from Akkerhuis [3] (that is going to be revisited later).

The temperature profile of one orbit is visualized in Figure 4.17, and it shows that the seasonal profiles are similar, and have a temporal shift due to the different Sun angles. The seasonal maximums and minimums are close to each other, and the vernal and autumnal profiles are practically the same.

The results of the studies are summarized in Table 4.9 with temporal minimal and maximal temperatures considering the geometrical average temperatures and the extreme nodal temperatures (the geometrical average temperature is the mean of the nodal temperatures). The differences are limited: the maximal seasonal difference is 7.51 K in the averaged values, and 8.78 K in the nodal ones. The warmest temperatures are found in December, and the coldest ones are usually in March In the following studies the worst hot case is used.

4.3.7. Baffle Height and Cross-conductance

So far the effect of the baffle height and cross-conductance on the TIR telescope temperatures have not been studied. The point of this section is to give an overview of the effect of baffle elongation and more MLI layers on the telescope temperatures, and to help with the decision on the required baffle height and cross-conductance. The impact of the change of the two baffle parameters is studied simultaneously.

With increased baffle height the telescope is better protected from direct sunlight and from Earth IR and albedo not coming from the optical FOV. The baffle cross-conductance is one way to represent the insulating effect of the MLI layers, and it is mainly dependent on the MLI structure. In more detail, according to the Doenecke-method [13] the cross-conductance is a function of:

- Number of MLI layers,
- Perforations,
- MLI area,
- MLI mean temperature.

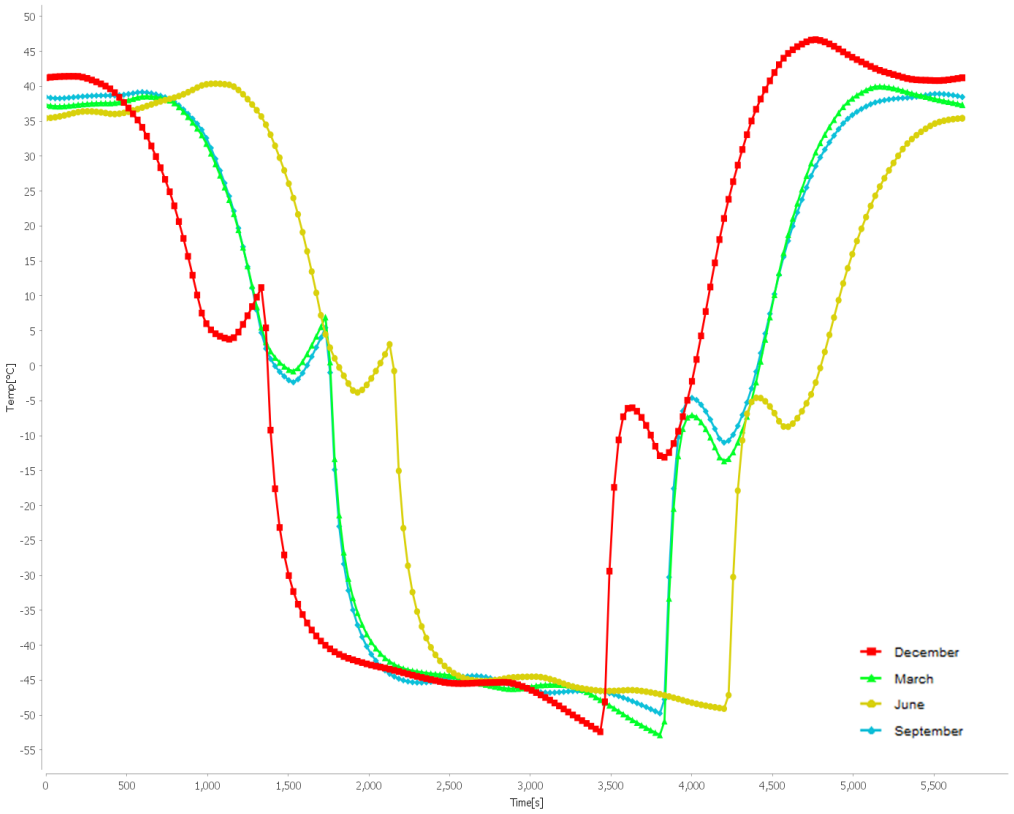

Figure 4.17: *Geometrical average temperatures of the baffle in December, March, June, and September.*

Table 4.9: *Seasonal variation of the minimal and maximal temperatures (in °C) of the TIR DST geometries. IH: instrument housing.*

		December	March	June	September
Baffle	Avg. - MIN	-52.38	-52.84	-49.08	-49.75
	Avg. - MAX	46.68	40.00	40.38	39.17
	Node - MIN	-88.46	-89.17	-88.10	-88.24
	Node - MAX	150.41	142.84	141.63	144.41
M1	Avg. - MIN	4.16	2.09	2.31	2.46
	Avg. - MAX	14.81	11.64	11.68	11.89
	Node - MIN	3.89	1.74	2.00	2.12
	Node - MAX	15.09	12.11	12.17	12.37
M2	Avg. - MIN	15.10	11.65	11.40	11.61
	Avg. - MAX	17.82	14.07	13.75	13.98
	Node - MIN	15.10	11.65	11.40	11.61
	Node - MAX	17.83	14.08	13.77	13.99
IH	Avg. - MIN	-10.54	-11.63	-10.38	-10.06
	Avg. - MAX	26.55	22.32	24.54	22.98
	Node - MIN	-18.93	-19.46	-16.15	-16.06
	Node - MAX	31.52	25.24	28.35	25.91

To keep the study fairly simple, the cross-conductance of the baffle is given fixed values, practically decoupling it from the baffle parameters above. In the detailed design stage it is recommended to redo the study with the coupled baffle parameters in accordance with the Doenecke-method. According to Arink [5] the effective conductance of a cylindrical baffle is 0.1651 W/m^{2}K with 2 MLI layers, and 0.0952 W/m^{2}K with 6 layers. This gives ballpark numbers for the analysis, in which the conductance values are selected to be between 0.05 and 0.17 W/m^{2}K with 0.03 W/m^{2}K increments (5 study points).

The baffle height is set to be between 1.5 and 2.5 m with 0.25 m increments (5 study points). The 1.5 m high baffle barely covers the M2, and the 2.5 m length threshold is selected as it is unlikely that a baffle length longer than that is chosen because of mass and volume considerations. All baffle conductance and height values are cross-tested with each other, making the final study number 5x5=25. The results are presented in Figure 4.19.

The extreme temperatures of outer side of the baffle are unaffected by the height of the baffle, but increasing baffle conductance increases the minimal temperatures. The extreme temperatures of the baffle inner side are practically independent of the baffle height, but with increasing conductance the minimal temperatures decrease and the maximal ones increase slightly. The baffle conductance slightly affects the extreme temperatures of the secondary mirror, with increasing conductance the M2 temperatures decrease. With increasing baffle height the M2 temperatures increase slightly first, peaking at 1.75 m height, then decrease. The primary mirror temperatures decrease with increasing baffle height, the minimal temperatures decrease and the maximal temperatures increase with increasing cross-conductance. The instrument housing maximal temperatures decrease and the minimal temperatures slightly increase with increasing baffle height, while the maximal temperatures of the IH slightly increase, and the minimal temperatures decrease with baffle conductance.

With increasing baffle conductance the temperatures of the inner and outer sides of the baffle approach each other, as it is expected. The initial increase in the temperatures of the M2 with increasing baffle height is surprising, and can probably be traced back to the increasing view factor to the warmer interior of the baffle and the minimally decreasing heat load from Earth, however, the reasons need further study. The primary mirror temperature extremes follow the temperature change of the baffle inner side, and the instrument housing generally does the same. This means that the temperatures the telescope parts further away from the opening of the baffle are dominated by the baffle inner temperature. The telescope parts closer to the baffle opening suffer more from the thermal effects of space and Earth.

According to the study, the baffle parameters hardly affect the telescope temperatures. The biggest effect is observable in the baffle outer side (19.3 K), but this temperature is irrelevant for the telescope. The biggest difference in the inner part of the baffle is 7 K, in the M2 it is 6.1 K, in the M1 it is 2.1 K, and in the instrument housing it is 5.5 K.

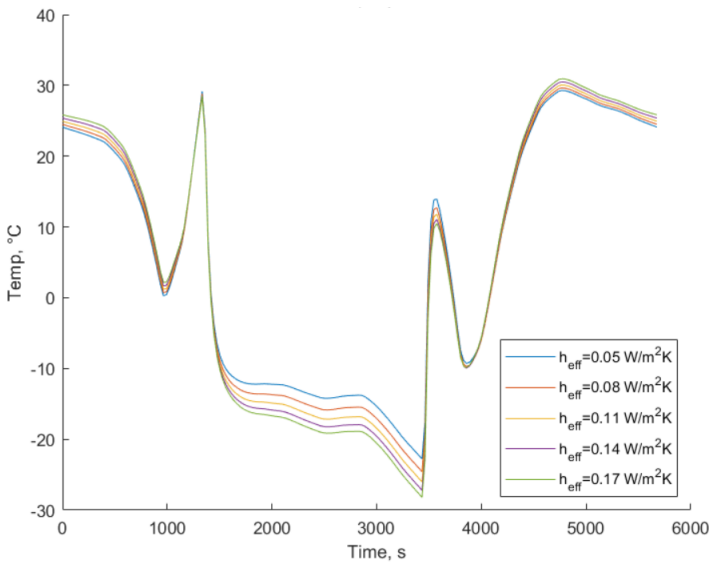

Figure 4.18: *Temperature of the baffle inner side as a function of baffle cross-conductance with $h_b = 1.5$ m.*

Figure 4.18 shows the temperature profiles of the baffle inner side with 1.5 m baffle height. With chang-

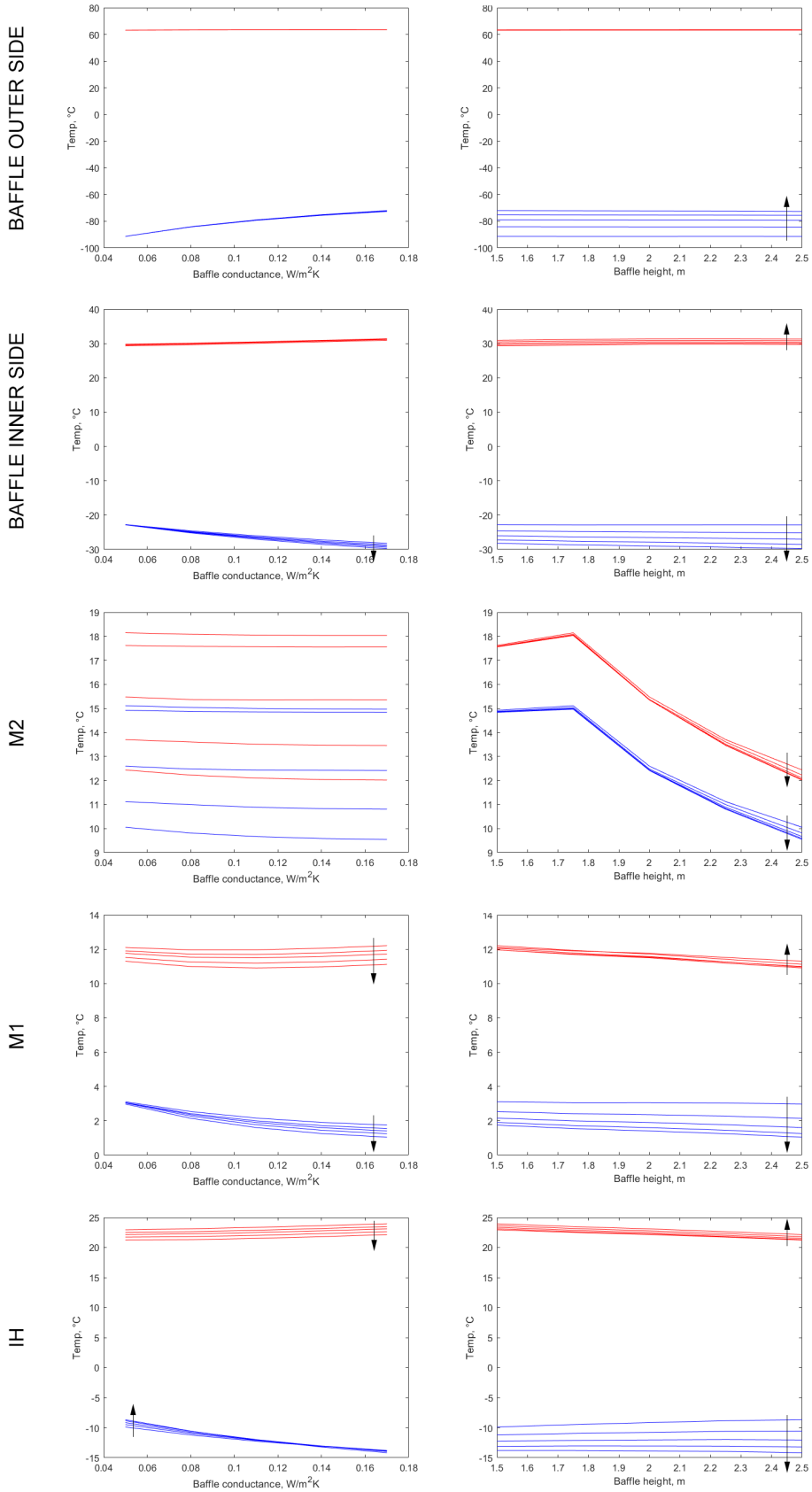

Figure 4.19: *Telescope geometrically averaged minimum (in blue) and maximum (in red) temperatures as a function of baffle conductance and height. The black arrows show the direction in which the other variable (that is not on the x-axis) increases.*

ing the baffle height or cross-conductance, the shape of the profile does not change, only the distance of the extreme temperatures, but even this change is limited. The temperature of the baffle inner side is the thermal environment that plays an important role in the temperature profiles of the other telescope parts, consequently this also means that the possibilities are quite restricted to significantly affect the telescope temperatures by altering solely the baffle height and cross-conductance. To shift the temperature profiles higher or lower a solution could be changing the optical properties of telescope parts, thus affecting their absorbed and emitted radiation.

For a TIR telescope it is foreseen that colder temperatures are desirable to limit the IR self-emission of the telescope parts, furthermore, the temperature variances of the telescope parts should be limited. Based on the results of this study, with increasing baffle height only marginal improvement is achievable in the telescope temperatures, therefore the recommended baffle height is the minimal baffle height that already shields the secondary mirror, as any further height addition would increase the mass and volume of the baffle with negligible thermal benefits. Based on 3D models and orbit analysis, with at least 1.9 m high baffle the secondary mirror is protected from direct sunlight at any point of the orbit, consequently the chosen baffle height is 1.9 m.

The effect of lowering the cross-conductance is more noteworthy, however, still limited. Considering only the results of this study it is favorable to reduce the the baffle cross-conductance as much as possible, nevertheless, if more variables were introduced, the trade-off would probably be more complicated with a less certain outcome.

To test if the model accurately represents the cross-conductance of the baffle and its effects, it is raised to a high value: $h_{eff} = 2000$ W/m^{2}K. With a value this high the baffle inner and outer side is expected to have the same temperatures, as the insulating effect of the MLI layers has been eliminated. The simulated result of such a high cross-conductance is presented in Figure 4.20, which verifies cross-conductance behavior of the model. The same result has been achieved with only one layer of baffle by fusing the outer and inner side together. These studies show that although increasing the number of MLI layers have marginal impact, the presence of (even minimal amount of) insulation between the baffle sides is definitely needed to limit the temperature variance within the baffle.

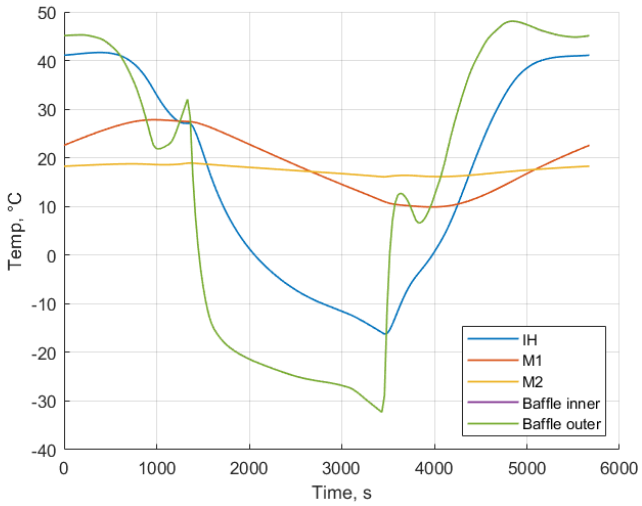

Figure 4.20: *Temperature of the telescope elements with $h_{eff} = 2000$ W/m^{2}K and $h_b = 1.9$ m. The lines of Baffle inner and Baffle outer side completely overlap each other.*

The study in this section kept the baffle inner and outer optical properties constant, and the mass of the baffle has not been changed by changing its cross-conductance. If it has been modelled, decreasing cross-conductance would have increased the baffle mass, therefore its capacitance as well, that would have resulted in reduction in further temperature variations. As mentioned previously, the baffle cross-conductance is dependent on its mean temperature as well, which has not been included in this study.

4.3.8. Thermo-optical Properties of the Baffle

In this section the effect of thermo-optical properties of the baffle on the temperature of the telescope parts is checked. As this work focusses on the baffle, only the baffle optical properties are studied, and the rest of the telescope is left for subsequent studies. The optical properties of the telescope parts are inherited from Akkerhuis' work [3] unless otherwise specified in Section 4.3.3.

The inner side of the baffle was covered with Magic Black coating ($\alpha = 0.93$, $\varepsilon = 0.84$) in the previous works to limit stray-light [5]. The same coating was used as a baseline for the studies, along with 1.9 m baffle height and 0.05 W/m^{2}K cross-conductance.

In the first studies the emissivity of the inner side of the baffle is changed from 0.84 to a) $\varepsilon = 0.95$ and b) $\varepsilon = 0.7$, keeping the rest of the parameters unchanged. The results of the ESATAN simulations are presented in Figure 4.21. In case a) the temperature of inner side of the baffle slightly decreases during sunlit periods, the rest of the temperatures remain unchanged. In case b) the temperature of the baffle inner side slightly increases during sunlit periods, so does the temperature of the instrument housing. The temperature changes is cases a) and b) are directly connected to the change of the dissipated IR radiation of the inner side of the baffle (as a results of the altered emissivity).

In case c) the emissivity of the baffle inner side is kept at $\varepsilon = 0.84$, but the absorptivity is decreased to $\alpha = 0.7$. The temperature profile results show decreased temperatures of the baffle inner side in sunlit periods, which is expected due to the decreased absorbed solar radiation because of the reduced absorptivity. These studies show that altering the optical properties of the inner side of the baffle returns minimal benefit, although – if the optical requirements allow – reducing the absorptivity decreases the most of the maximal temperature of the inner side of the baffle, so it is worth considering. In the studies only the thermal consequences of the change of optical properties were inspected, the optical consequences were left out. If more optical requirements are available, the study should be repeated with the allowed range of optical properties.

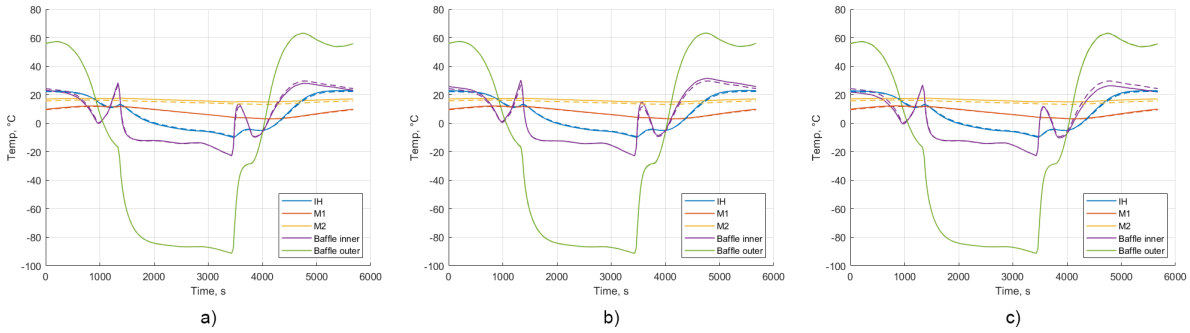

Figure 4.21: *Temperature profile of the telescope parts with optical properties of a)* $\alpha = 0.93$, $\varepsilon = 0.95$. *b)* $\alpha = 0.93$, $\varepsilon = 0.7$, *c)* $\alpha = 0.7$, $\varepsilon = 0.84$ *of the inner side of the baffle. The dashed lines represent the baseline profiles.*

The second set of studies concerned the outer side of the baffle. The results are still compared to the same baseline, with $\alpha = 0.19$ and $\varepsilon = 0.14$ being the optical properties of the outer side of the baffle. The result of the studies are shown in Figure 4.22. In case a) the emissivity and absorptivity are decreased to 0.1, and in case d) to 0.05. The reduced heat absorption (in sunlight) and dissipation (in eclipse) is instantly visible on the temperature profiles of the baffle outer side, reducing the extreme temperatures. However, because of the insulating effect of the baffle, the effect is negligible on the inner side of the baffle.

In cases c) and d) a new approach has been tried out. In order to decrease the temperature of the baffle, its heat dissipation needs to be increased if limiting the heat absorption is not enough (as it has been seen with cases a) and b)). Heat dissipation can be increased by increasing the emissivity of the outer side of the baffle. As the outer side of the baffle has a large view factor to space, the increased emissivity results in increased heat dissipation. Meanwhile, the absorptivity needs to be kept as low as possible to limit the solar heat absorption. Such hardware that fulfills these criteria are known as Optical Solar Reflectors (OSRs), but they are mostly rigid. A flexible MLI outer coating that has similar properties has been used in the Bepi-Colombo mission to Mercury [4]. Typical OSR optical properties has been added to the outer side of the baffle ($\alpha = 0.09$, $\varepsilon = 0.76$) in cases c) and d), and their effect in reducing the baffle outer temperatures is impressive. The effect on the inner side is reduced, but still considerable compared to the previous cases. In order to increase the effect of the OSR-like coating on the inner side, the baffle cross-conductance is increased from 0.05 to 0.17 W/m^{2}K in case d) (that roughly translates to 6 and 2 layers of MLI, respectively [5]). Case d) re-

duces the minimal and maximal temperatures of most of the telescope parts jointly: the temperatures of the instrument housing are reduced by 14 K, the M1 by 15 K, the inner side of the baffle by 15 K, and the maximum temperature of the baffle outer side by 117 K, and the minimum by 13 K. The temperatures of the M2 are practically unchanged. Based on the results OSR-like coatings do not reduce the temperature gradients or variances inside the baffle, however, they do reduce the overall temperatures substantially, which might be useful if the optical requirements call for reduced telescope temperatures to limit self-IR emission.

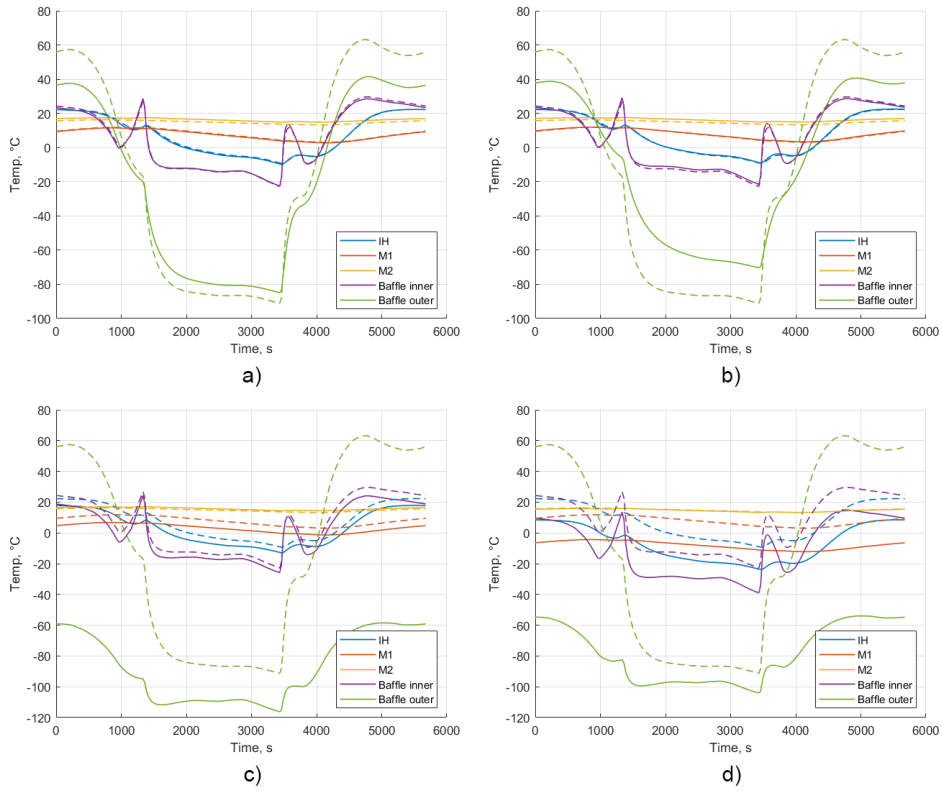

Figure 4.22: *Temperature profile of the telescope parts with optical properties of a) $\alpha = 0.1$, $\varepsilon = 0.1$. b) $\alpha = 0.05$, $\varepsilon = 0.05$, c) $\alpha = 0.09$, $\varepsilon = 0.76$ of the outer side of the baffle. Case d) similarly has $\alpha = 0.09$, $\varepsilon = 0.76$, but the baffle cross-conductance is increased from 0.05 to 0.17 W/m^2 K. The dashed lines represent the baseline profiles.*

4.3.9. Truncated Cone

The idea of the truncated cone was first introduced to the VIS DST by van Wees [48], and was further elaborated by Arink [5]. Closing the top part of the baffle (but still not limiting the field of view of the telescope) reduces stray-light and the heat entering the baffle. Therefore, its utility is checked for the TIR telescope as well.

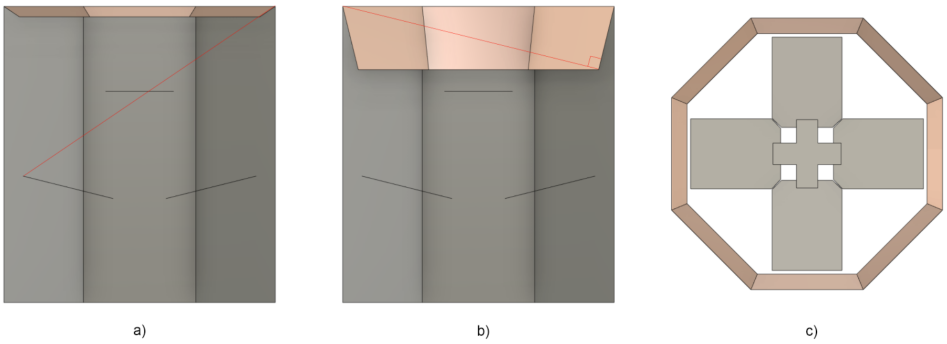

Figure 4.23: *a)-b) Different truncated cone solutions presented in longitudinally cut baffles. c) Top view of the two truncated cone designs (same).*

First, a truncated cone with 100 mm radial thickness is studied, see Figure 4.23a,c. 100 mm was selected to cover the extra space between the primary mirror and the baffle as much as possible without limiting the field of view of the telescope. Furthermore, the angle between the truncated cone and the vertical axis (56.1°) has been chosen not to allow any reflected light from the truncated cone top side to directly reach the primary mirror. For the preliminary design, the thickness of the truncated cone is considered to be 0.5 mm, its material is Al-Li 8090, the same material that has been selected for the frame of the baffle for its low density and high strength. The top side of the truncated cone is coated with the same reflecting layer as the MLI ($\alpha = 0.19$, $\varepsilon = 0.14$), the bottom side is coated with Magic Black ($\alpha = 0.93$, $\varepsilon = 0.84$) as the rest of the inner side of the baffle to avoid stray-light. The temperature results are presented in Figure 4.24. The truncated cone has effect only on the baffle inner side, with slightly reducing the temperature gradients, but the extreme temperatures remained unchanged.

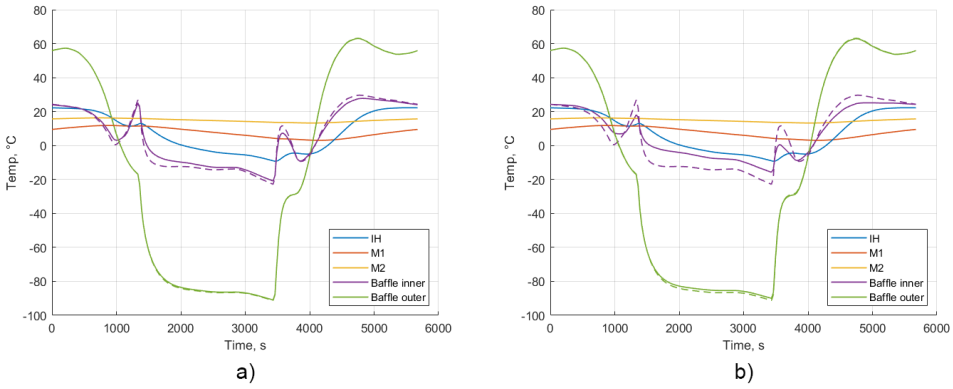

Figure 4.24: *Temperature profile of the telescope parts with truncated cones a) and b). The dashed lines represent the baseline profiles.*

Based on the results, a second configuration of the truncated cone is studied: the radial thickness remains 100 mm, but its angle is modified (13.8°) so that the truncated cone covers more of the inner side of the baffle than the previous case, but does not allow the direct sunlight to be reflected to inside of the baffle, see Figure 4.23b-c. This way it provides more protection from the direct sunlight that would reach the inner side of the baffle at eclipse ingress and egress. The material and the bottom coating remains unchanged, but the top side is given a more reflective coating: vapor deposited silver ($\alpha = 0.04$, $\varepsilon = 0.02$). The effect of the truncated cone is now more perceptible with increased minimum temperature of the baffle inner side, and reduced eclipse ingress and egress spikes, as shown in Figure 4.24b. Although the effect on other telescope parts is negligible, the thermal environment inside the baffle is mainly determined by the temperature of the baffle, thus the truncated cone can help limit the thermal gradients of the yet unmodelled parts with lower thermal mass. On the other hand, the reflective surfaces within the baffle might cause problems to the optical performance of the telescope. Similar truncated cones with low angles have been modelled for the VIS telescope, and optical studies showed that the optical performance (Point Source Transmittance) of the telescope is not degraded substantially by the introduction of the truncated cone [20]. However, the optical studies need to be repeated for the TIR telescope as well to ascertain there is no considerable degradation in the optical performance.

4.3.10. Summary - Baffle Thermal Properties

Many combinations of the baffle properties have been studied in the previous sections. The goal of this section is to find the best combination of them, and to discuss the achievable telescope temperatures.

The best set of optical properties of the baffle was OSR-like coating ($\alpha = 0.09$, $\varepsilon = 0.76$) on the outside, and the inner side coating did not affect the telescope temperatures considerably, thus it is left with the Magic Black coating ($\alpha = 0.93$, $\varepsilon = 0.84$). The most effective truncated cone design proved to be the one in Figure 4.23b, and it is also included in the final design. The joint effect of the said coatings and truncated cone is presented in Figure 4.25 with two different cross-conductances: 0.05 and 0.17 W/m^{2}K.

Without clear thermal goals and requirements it is difficult to select the best design, as both of them excels at different properties. The case with $h_{eff} = 0.17$ W/m^{2}K has generally lower temperatures, which is useful for limiting the self-IR emission. On the other hand, the case with $h_{eff} = 0.05$ W/m^{2}K has lower temperature variance in the inner side of the baffle (see Table 4.10), which is advantageous for the subsystems that are

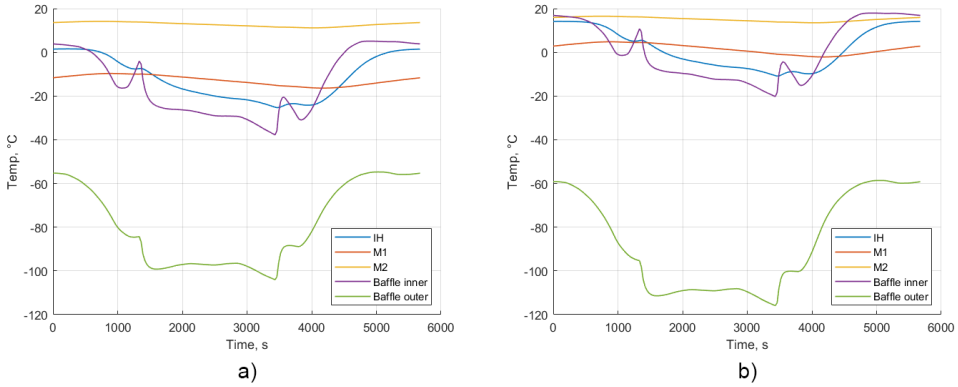

Figure 4.25: *Temperature profile of the telescope parts with truncated cone from Figure 4.23b, OSR-like baffle outer coating ($\alpha = 0.09$, $\varepsilon = 0.76$), and Magic Black inner coating ($\alpha = 0.93$, $\varepsilon = 0.84$). The cross-conductance of the baffle is a) 0.17 W/m^{2}K, b) 0.05 W/m^{2}K.*

Table 4.10: *Geometrically averaged minimum and maximum temperatures of the telescope parts in case a) and b), along with the differences between the extremes.*

	Max, °C		Min, °C		Delta, K	
Telescope part	Case a)	Case b)	Case a)	Case b)	Case a)	Case b)
IH	1.6	14.2	-25.3	-10.9	26.9	25.0
M1	-9.7	4.8	-16.4	-2.1	6.7	6.9
M2	14.2	16.5	11.2	13.5	3.0	3.0
Baffle inner	5.1	17.9	-37.8	-20.3	42.9	38.2

yet to be designed and might suffer from thermal expansion and/or hysteresis effects due to temperature gradients (e.g. SMSS). For now, the design with lower temperatures (and with $h_{eff} = 0.17$ W/m^{2}K) is selected as the lower self-emission seems more important currently than the slightly better temperature variance. However, a more detailed trade-off needs to be done as soon as the optical and thermal requirements are available.

The thermal design of the baffle is left at preliminary design stage, and needs to be revisited when more details and requirements are available. It is likely that the current design needs fine-tuning, which can be done by modifying the following properties of the baffle (with the achieved effect):

1. **Baffle height.** Decreasing the baffle height is not advised with the current baffle geometry as it would allow for the solar exposure of the secondary mirror during eclipse ingress and egress. Increasing the baffle height slightly decreases the temperature variances of the telescope parts, but the effect is negligible, see Figure 4.19.

2. **Baffle cross-conductance.** With increased cross-conductance the temperature difference between the baffle inner and outer side decreases, and the temperature variations of the outer side are better represented in the inner side, see Figure 4.19. With decreased cross-conductance the insulating effect of the baffle is more prominent, and the temperature of the inner side of the baffle is more effectively decoupled from the outer side. However, having a higher cross-conductance is not necessarily disadvantageous, see the temperature profile of the selected design in Figure 4.25a. In the detailed design stage it is recommended to use a cross-conductance model that considers number of the MLI layers, perforations, area, and mean temperature. Furthermore, changes in the cross-conductance affect the baffle mass and thermal mass as well, which is not yet modelled.

3. **Absorptance and emissivity – inner side.** The thermo-optical properties of the baffle inner side is mainly controlled by the optical requirements, i.e. mitigating stray-light. The thermal designer's work is constrained in this sense, and they can only select coatings that conform the optical requirements. Increasing the emissivity of the inner coating slightly decreases the maximum temperature of the baffle inner side, decreasing the emissivity achieves the reversed effect. Decreasing the absorptance de-

creases the maximum temperature of the baffle inner side. The relationships are presented in Figure 4.21.

4. **Absorptance and emissivity – outer side.** Reducing the emissivity and absorptance of the baffle outer side reduces the temperature variations of the outer side, making the maximum temperature lower and the minimum higher. On the other hand, this effect is barely translated to the temperature of inner side, although a higher cross-conductance would facilitate it. A much more perceptible change can be achieved in the temperature profiles of the telescope parts if the absorptance is kept at minimum, but the emissivity is increased considerably. This way the temperature of the baffle is shifted towards the colder regions, and its temperature variance decreases as well (see Figure 4.22), both of which is an advantage for a TIR telescope. The results can be fine-tuned with coatings with different α/ε ratios.

5. **Truncated cone.** A truncated cone can help limit the solar illumination of the inner side of the baffle during eclipse ingress and egress. The thermal designer needs to balance again between the thermal advantages and the optical disadvantages of their work, as reflective surfaces are introduced to the inner side of the baffle. With a truncated cone the temperature peaks in the baffle inner side during eclipse ingress and egress can be reduced, and the minimal temperatures be increased (see Figure 4.24), which are both advantageous for a TIR telescope. The designer have the freedom to customize the geometry, material, and the thermo-optical properties of the truncated cone. However, it is recommended to check if the truncated cone decreases the optical performance of the telescope.

4.3.11. Baffle Cooling

TIR telescopes are generally sensitive to the temperature of their parts, and often they are actively cooled. In this section it is preliminarily studied how much temperature change can be achieved with coolers attached to the inner side of the baffle.

As the thermal goals and temperature limits of the TIR DST parts are not yet known, instead of designing a cooling solution that can satisfy the thermal requirements (top-down approach), it is checked with different amounts of cooling power how much temperature change can be achieved (bottom-up approach). Consequently, the result of this section is not a working cooling solution, but a guideline for the future thermal designers of the DST what can be achieved by cooling the inner side of the baffle.

Furthermore, this study does not differentiate between active or passive cooling, but focusses on the result of the cooling. The analysis is done in ESATAN-TMS, similarly to the previous thermal studies, but the program has its shortcomings with cooler modelling. The coolers are modelled as heat load boundary conditions with negative values, which work fine as far as they are always on. However, when a thermostat function is selected, the switch on and switch off temperatures of the thermostat are working only for heaters, and not for coolers, as the on and off temperatures are reversed in that case. Consequently, only always on coolers are modelled for now.

There are several ways to cool the telescope. Some solutions focus on certain parts of the telescope that have strict thermal requirements, others cool bigger parts of the telescope. The solution presented in this section belongs to the second group. The entire inner side of the baffle is cooled uniformly, and a fixed amount of (negative) heat load is distributed along its area. Cooling the inner side of the baffle is expected to lower the temperature of the whole telescope, however, the magnitude of the effect is different on all parts. The feasibility of this solution is not studied.

As a baseline the selected preliminary thermal design is used (Figure 4.25a). Then, ten different cooling loads are applied uniformly on the inner side of the baffle, ranging from 10 W to 100 W. The results are presented in Figure 4.26. The applied cooling load linearly decreases the minimum and maximum temperatures of the primary mirror, the instrument housing, and the inner side of the baffle. The secondary mirror and the outer side of the baffle are practically unaffected by the cooler. The temperature range of the instrument housing and the primary and secondary mirror remain the same regardless of the cooling load, meanwhile the temperature range of the baffle inner and outer side increase linearly with cooling load. Cooling of the inner side of the baffle shifts the temperature profiles towards cooler temperatures, the shapes of the profiles are unaffected. The achievable temperature difference in case of 100 W (compared to the baseline) is shown in Table 4.11. The most significant effect is on the minimum temperature of the inner side of the baffle: 18 K temperature reduction, and the effect is smaller on the rest of the telescope parts.

Always on coolers on the inner side of the baffle barely affect the temperature variance inside the baffle, and do not cool effectively the telescope parts, as the achieved temperature shift is rather limited. Similar results have been achieved by modifying the coating of the baffle outer side, which appears to be an easier

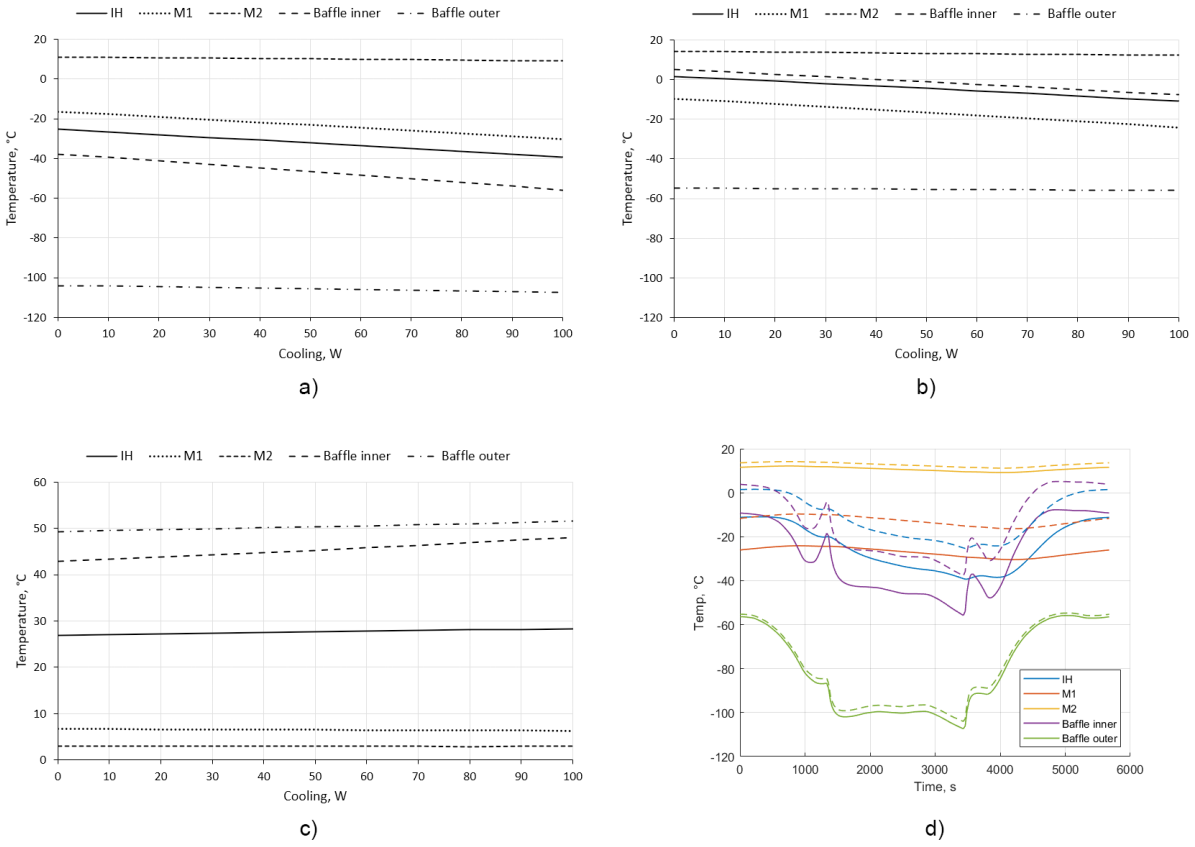

Figure 4.26: *Geometrically averaged a) minimum and b) maximum temperatures with different amount of cooling applied uniformly to the inner side of the baffle. c) Temperature range ($T_{max} - T_{min}$) as a function of cooling load. d) Temperature profiles with 0 (dashed lines) and 100 W cooling power (solid lines).*

Table 4.11: *Difference of the minimum and maximum temperatures of the telescope parts with 0 and 100 W cooling load.*

	ΔT_{min}, K	ΔT_{max}, K
IH	-14,0	-12,5
M1	-14,1	-14,4
M2	-2,0	-2,0
Baffle inner side	-18,0	-12,9
Baffle outer side	-3,3	-1,1

solution to realize. However, this is just a preliminary result, and it is recommended to check the achievable benefits of coolers with thermostat, and study different cooling arrangement and solutions.

4.4. Axial Module Design

The radial module design determined the diameters of the deployed baffle, the preliminary thermal design resulted in a selected baffle height, and based on them, the axial modules of the pantographic structure can be designed.

4.4.1. Design Based on VIS Legacy

The previously defined geometrical relationships between the axial and radial modules (Equations (3.13) to (3.16)) are still valid. With x_d = 174.01 mm, w = 15 mm, t_{st} = 136.20 mm, x_{st} = 109.33 mm they can be simplified to:

$$H_{st} = \sqrt{164938 + H_d^2 - 18325.7m^2} \tag{4.5}$$

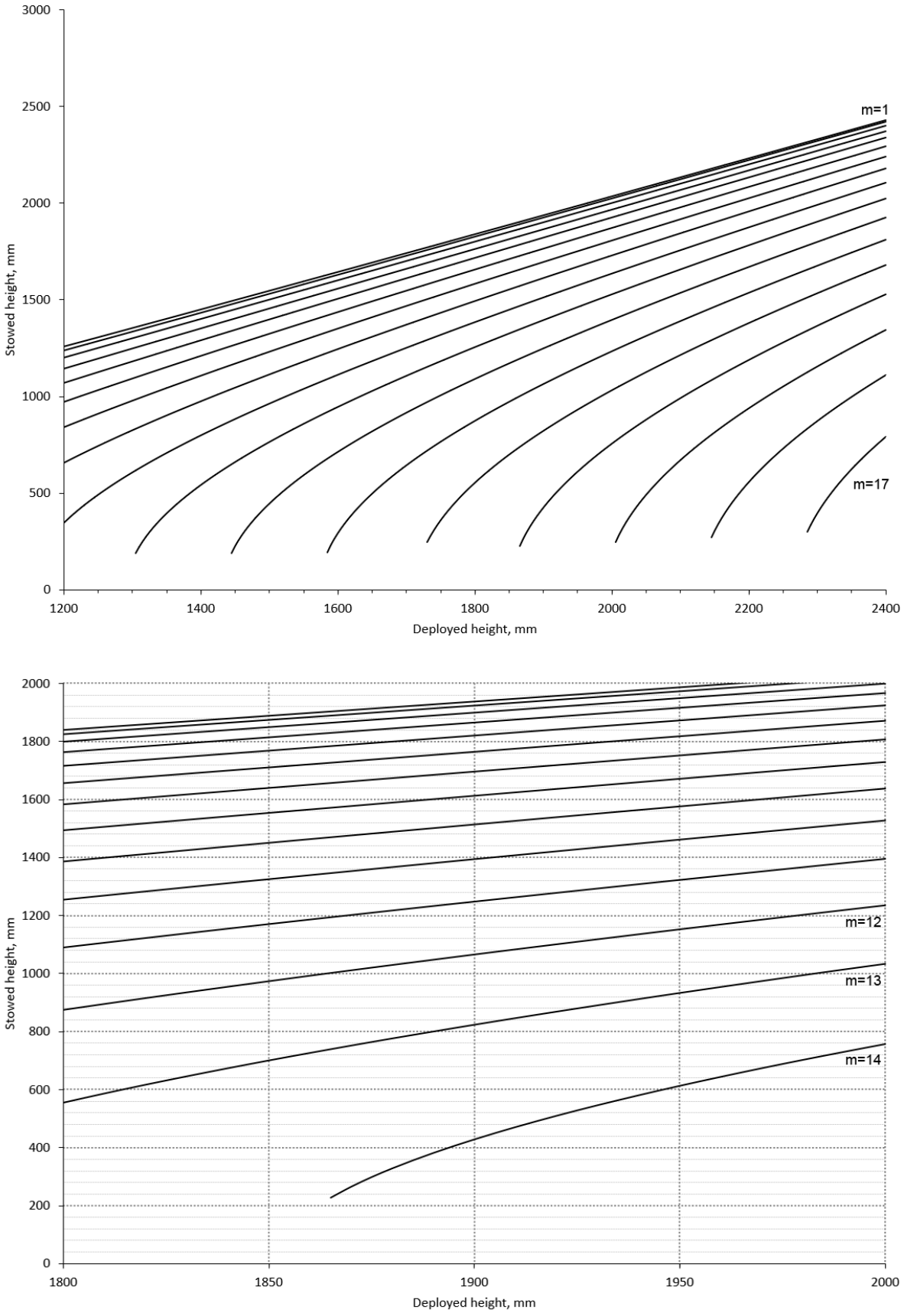

Figure 4.27: *Stowed height of the axial modules as a function of deployed height and number of units in the module m. At the bottom a part of the top diagram is enlarged to better showcase the available solutions with deployed height of 1900 mm.*

Table 4.12: *Comparison of the properties of the chosen axial modules for the VIS and TIR DST.*

	VIS	**TIR**
Deployed height, mm	2650	1900
Stowed height, mm	696.7	823.3
w, mm	15	15
p, mm	159.8	152.3
m	17	13
Stowed angle, degree	32.3	53.2

and Figure 3.46 can be updated. The results are shown in Figure 4.27, that suggest that deployed height H_d of 1900 mm can be achieved with any number of units in the axial module below 15. However, the stowed height H_{st} of the instrument (without the baffle, and according to the conceptual deployment design shown in Figure 4.5, which can change later) is 995.2 mm, and a higher stowed baffle than this would drive the stowed height of the telescope, and therefore should be avoided. Stowed height of the baffle that is lower than 995.2 mm can only be achieved with $m = 13$ or 14, which would result in stowed height of 823.3 and 427.9 mm, respectively. Higher stowed baffle offers more space for the stowed shroud, and lower number of units in the module reduces the complexity of the baffle. Currently no use of the extra space in case of $H_{st} = 427.9$ mm is foreseen. Based on these $m = 13$ is a better solution, consequently the selected number of units in the axial module is 13, that results in a stowed height of 823.3 mm. The full list of axial module properties is shown in Table 4.12. As a reference, the properties of the chosen VIS axial module are indicated there as well.

4.4.2. Design with Constant Angle

The geometry and proportions of the TIR baffle allow for another, special design of the axial structure that was unavailable for the VIS baffle. In the VIS baffle structure the angle between the radial and axial modules constantly changes during deployment (see Figure 3.48) as the deployment ratio of the radial and axial straight modules are unequal. In theory it is not a problem, but if a structure like this needs to be realized, additional degree of freedom is to be granted for the aforementioned angle to change. This would further increase the complexity of the already complex structure, which could be avoided if the angle was constant.

The angle remains constant during deployment if the deployment ratios of the radial and axial straight modules are equal. In the VIS baffle it was unrealizable as the deployment ratios were so different. With the TIR baffle, however, the deployment ratios are closer to each other, therefore it is checked if a structure with constant angle between the modules is achievable, considering the geometrical constraints of the telescope.

The radial structure is left untouched, only new axial modules are designed. Based on Figure 3.45 the deployment ratio of the straight modules need to be:

$$\frac{y_d}{y_{st}} = \frac{H_d}{H_{st}} = \frac{x_d}{x_{st}} = 1.592 \tag{4.6}$$

The deployment ratio can be expressed with Equation (4.5) as well:

$$\frac{H_d}{H_{st}} = \frac{H_d}{\sqrt{164938 + H_d^2 - 18325.7m^2}} = 1.592 \tag{4.7}$$

From which the deployed height as a function of m:

$$H_d = \frac{3979\sqrt{-1649380 + 183257m^2}}{\sqrt{95824410}} \tag{4.8}$$

Using Equation (4.8) and Equation (4.5) the achievable deployed and stowed height pairs are shown in Table 4.13. From these, 1841.5 mm deployed height is the closest to the required 1900 mm, with $m = 11$. The slightly lower height is not a problem as the radial module thickness and the height of the radial-axial module connection joints can compensate for the missing 58.5 mm. On the other hand, the prescribed stowed height of this arrangement is 1157 mm, which is higher than the stowed instrument (995.2 mm).

4.4.3. Decision

The two solutions for the TIR axial modules presented previously have both advantages and disadvantages. The one with constant angle offers a simpler mechanism to the detriment of the stowed height. The solution

Table 4.13: *Achievable deployed and stowed height pairs with equal radial and axial straight unit deployment ratio as a function of m.*

m	H_d, mm	H_{st}, mm
4	460.4	289.2
5	696.0	437.3
6	904.2	568.1
7	1100.5	691.4
8	1290.5	810.8
9	1476.5	927.7
10	1659.9	1042.9
11	1841.5	1157.0
12	2021.8	1270.3
13	2201.0	1382.9
14	2379.5	1495.0
15	2557.4	1606.8

Table 4.14: *Comparison of the properties of the chosen axial modules for TIR with changing (TIR 1) and constant angle (TIR 2) between the radial and axial modules during deployment.*

	TIR 1	**TIR 2**
Deployed height, mm	1900	1841.5
Stowed height, mm	823.3	1157.0
w, mm	15	15
p, mm	152.3	172.9
m	13	11
Stowed angle, degree	53.2	76.1

with changing angle has a lower stowed height, on the other hand the mechanism has to provide extra degrees of freedom to allow for the angle between the modules to change. To quantify the difference, 32 extra hinges (or equivalent) are required for the alternative with changing angle. A comparison table between the two TIR axial structure designs is presented in Table 4.14.

As no volume budget exists at the time of writing, it cannot be decided how severe the effect of exceedance is in case of the design with constant angle. A trade-off weighing the positive effect of the simplified structure and the negative impact of the increased stowed height is inherently sensitive without the finished set of requirements and budgets available for the TIR baffle.

In order to better understand the effect of the stowed baffle dimensions on the whole telescope, the stowed cylindrical volumes are compared to the cylindrical volume of a theoretical fixed baffle for the same telescope. This way, the utility of a deployable telescope is checked, and then the utility of the two alternatives can be compared. The comparison is presented in Table 4.15, and it shows that the volume ratios (the respective TIR deployable designs compared to a theoretical fixed baffle) change from 0.29 to 0.34, which is a 17% increase. In that sense, the increase is not significant, but the simplification of the mechanism is considerable, therefore, the design with constant angles between modules (TIR 2) is selected to continue with.

Table 4.15: *Comparison of the utility of the baffle design with changing (TIR 1) and constant (TIR 2) angle between the modules. The utility is expressed as the ratio between the volume of the respective TIR deployable design and a theoretical fixed baffle design. As a reference, the volume of the stowed TIR instrument without the baffle is included as well.*

	Diameter, m	Height, m	Volume, m^3	Ratio
Fixed	1.766	1.9	4.654	
TIR 1	1.322	0.995	1.366	0.29
TIR 2	1.322	1.157	1.588	0.34
TIR (no baffle)	1.023	0.995	0.818	0.18

5

Detailed Mechanical Design

In the previous chapters the preliminary thermal and mechanical design of the TIR pantographic baffle has been prepared. In this chapter the design process continues with the detailed mechanical design of the pantographic structure. First, the integration of the baffle to the instrument housing is discussed, then the integration of the radial and axial modules to each other. After that, the final shapes of the pantographic arms are defined, then the deployment actuation is designed. Finally, the shroud and its integration are discussed, and the final mechanical design is verified.

5.1. Baffle - Instrument Housing Integration

The baffle has been designed as the mantle of a deployable octagonal prism, but one of its bases is missing, which also serves as the mechanism to integrate the baffle to the instrument housing. This chapter concerns the design process of this mechanism.

5.1.1. Introduction

According to the baffle design it surrounds the telescope (including the instrument housing), and the base of the baffle coincides with the base of the instrument housing. The attachment mechanism cannot be placed to the bottom side of the instrument housing as the telescope-spacecraft bus integration is expected to take place there. The mechanism is therefore placed at the very bottom of the sides of instrument housing (mantle). For simplicity, this attachment mechanism is abbreviated as B2IH (Baffle to Instrument Housing) from now on. In the design process the following are considered:

1. **Multiple-point attachment.** The baffle is to be attached to the instrument housing at multiple (>1) points to facilitate load distribution.

2. **Symmetric attachment.** The baffle is to be attached to the instrument housing in a rotationally symmetric way to avoid the structure to be weaker in certain directions.

3. **Support in all configurations.** B2IH is to support the baffle in all deployment configurations.

4. **Allow for deployment.** B2IH is to allow for the deployment of the baffle, and at the same time, the B2IH needs to be deployable as well.

5. **Interference-free.** B2IH is to allow for an interference-free deployment, namely B2IH is not to collide with itself, the baffle structure, instrument housing, or the baffle shroud.

6. **Light and stiff.** B2IH is to be light to save mass, and have high stiffness to resist deformation.

Integrating the B2IH to the pantographic baffle structure is more difficult than to alternatives with different deployment mechanisms (e.g. to Arink's telescopic baffle [5]) as all the arms translate and rotate with respect to the instrument housing during deployment. Based on the deployment technique of the B2IH, two types can be distinguished:

1. **Conventional.** As discussed, the moving arms make it difficult to integrate the B2IH to the baffle, however, the vertices of the octagonal base, namely the middle rotational points of the angulated arms in the bottom radial module offer a usable alternative, as they are moving away from the center of the baffle during deployment in a radial line. Deployment mechanisms that are not specific to pantographic units can be utilized to radially connect the vertex points to the instrument housing (e.g. with telescopic booms).

2. **Pantographic-specific.** In this case the B2IH utilizes the uniqueness of the pantographic structure. An example for such mechanism is shown in Figure 5.1.

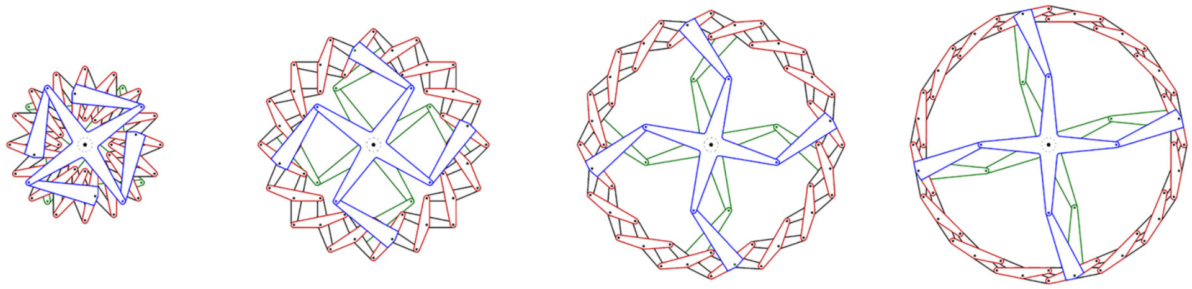

Figure 5.1: *Deployment sequence of an expandable ring of angulated scissor arms (example). [26]*

Pantographic-specific B2IHs are more interesting for the pantographic baffle, therefore their possibilities are examined first. If they turn out to be problematic, one can still revert to conventional B2IHs.

5.1.2. Pantographic-specific B2IH

A deployable pantographic baffle is a new idea, consequently its literature is scarce. The only similar application that was found and could work as a B2IH (with some modifications) is presented in Figure 5.1. Its radial module is deployed via two central crosses that rotate in opposite directions. The crosses are connected to the radial module with arms fixed to angulated units. This mechanism cannot be used for the DST as it is right now, as it needs to fit around the instrument housing. A solution could be to replace the crosses with central hubs that have large circular openings in the middle, but can perform the same task as the crosses. An example of the possible central hubs are presented in Figure 5.2.

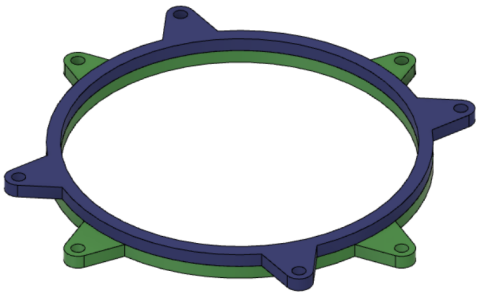

Figure 5.2: *Central hubs. A solution to fit the mechanism shown in Figure 5.1 around the instrument housing.*

The solution with central hubs might work, although it introduces the central hubs that are large and heavy, and would increase the total mass of the baffle substantially. Because of this, the idea of the central hubs is dropped.

However, it is further investigated if a mechanism similar to Figure 5.1 can be modified to eliminate the need for a central rotating element. The easiest way to integrate the deployed baffle to the instrument housing is to connect the vertices of the octagonal radial structure to the instrument housing radially, as presented in Figure 5.3b. If these radial booms are fixed to angulated arms (to utilize the pantographic deployment), they follow the rotation of the respective angulated arms during deployment. Consequently, some kind of hinge is required in the booms to keep the attachment points (between the booms and the instrument housing) at unchanged positions (see Figure 5.3a).

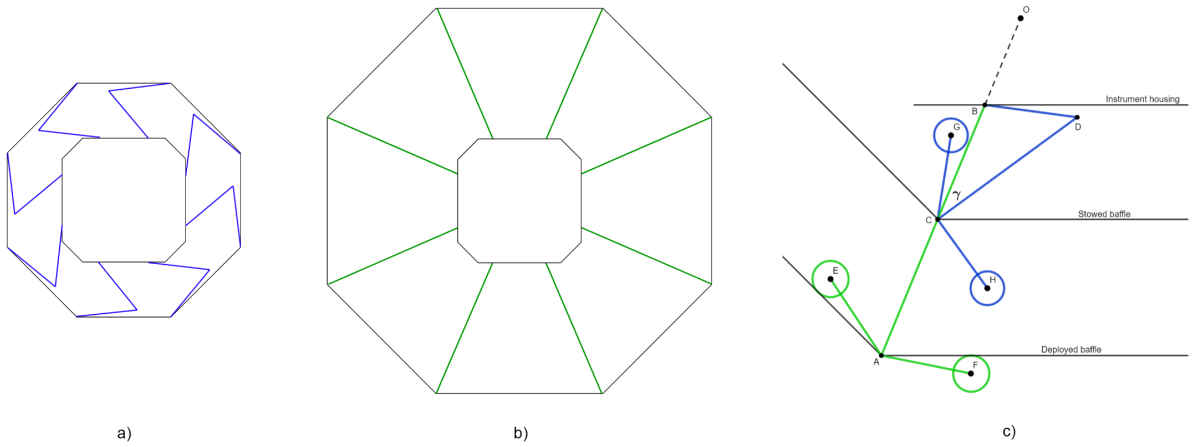

Figure 5.3: *A solution for B2IH with radial connection between the instrument housing and the baffle in a) stowed and b) deployed configuration, where the central octagon represents the instrument housing, while the outer regular octagons represent the baffle. c) Geometry of the B2IH mechanism in stowed (blue) and deployed (green) configuration (not to scale).*

The position of the hinge within the boom is calculated next, with the help of Figure 5.3c. The boom in deployed configuration is segment $\overline{AB}$, and collinear with segment $\overline{AO}$, with O being the geometrical centre of the radial module viewed from the top. The broken line $\overline{EAF}$ represents the segments connecting the rotational points of an angulated unit, while the circles around points E and F depict the arm thickness. The angles between segment $\overline{AB}$ and broken line $\overline{EAF}$ are fixed. In the stowed configuration the angulated arm takes a different position and orientation defined by the geometry of the radial module: deployed configuration's broken line $\overline{EAF}$ becomes broken line $\overline{GCH}$. The boom is divided into two segments:

$$\overline{AB} = \overline{CD} + \overline{DB} \tag{5.1}$$

From the baffle geometry $\overline{AO}$ = 936.27 mm, $\overline{CO}$ = 611.12 mm, $\overline{BO}$ = 297.66 mm, and $\gamma = \angle BCD = 39.86°$. The law of cosines can be applied to $\triangle BCD$:

$$\overline{BD}^2 = \overline{CD}^2 + \overline{CB}^2 - 2 \cdot \overline{CD} \cdot \overline{CB} \cdot \cos\gamma \tag{5.2}$$

Using Equations (5.1) to (5.2) and the baffle measurements the boom segment lengths can be calculated: $\overline{CD}$ = 388.92 mm, $\overline{DB}$ = 249.69 mm. The hinge needs to be at this exact position, otherwise the mechanism does not work.

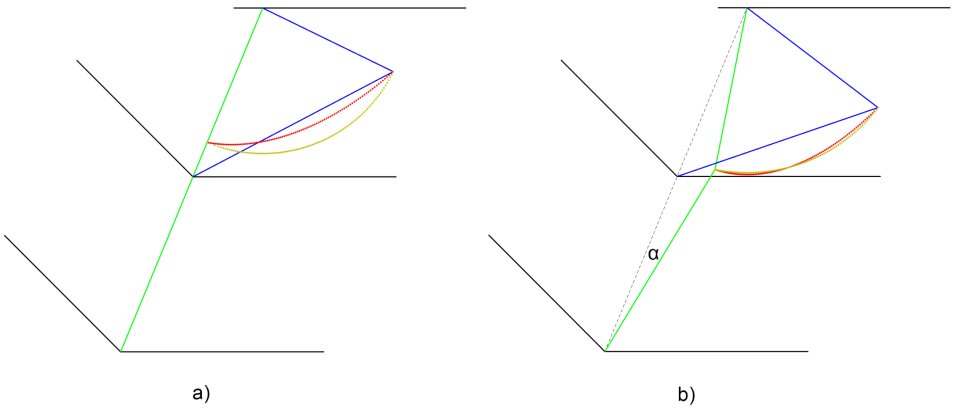

Figure 5.4: *B2IH in different configurations. The stowed configuration is shown in blue, the deployed one in green. The positions the B2IH hinge take during deployment are shown with dotted lines. The red dotted line shows the calculated positions from perspective of the radial module (with attached and fixed B2IH boom). The mustard colored dotted line shows the positions from the perspective of the B2IH. a) The deployed boom (green) is straight and radial, b) The deployed boom (green) is angled.*

However, there is another condition the B2IH needs to meet in order to be deemed usable: B2IH and the radial module of the baffle need to be geometrically compatible, which means in every configuration

they need to fit together without deformations [42]. To check that, the geometry of the two mechanisms are compared during deployment. The positions the B2IH hinge takes during deployment are checked from the perspective of the baffle radial module and of the B2IH. The comparative results are shown in Figure 5.4a. The figure proves that the mechanisms are compatible with each other in stowed and deployed configurations (as they were designed), on the other hand, during deployment the compatibility requirement is not met. Because of the hinge position difference the deployment cannot be realized without deformations, and the required deformation is considerably high (maximum 31 mm difference in Figure 5.4a).

The geometrical constraints can be loosened if a perfectly radial deployed B2IH boom is not prescribed, but the boom can be angled as well, described with angle α in Figure 5.4b. The deployment compatibility of the radial module and the B2IH has been checked with all possible α values, but no perfect compatibility has been found. The closest solution is with $\alpha = 8.753°$, and this solution is shown in Figure 5.4b, with maximal difference of 5.2 mm. The required deformation has been considerably reduced compared to the previous case, but still, some deformation is required from the B2IH to be deployable. There might be a mechanism that would allow for such deformation, but it is not studied further in this thesis.

A hinged connection between the B2IH booms and the baffle (instead of a fixed one) might help with the compatibility issues during deployment, however, the extra degrees of freedom the new hinges introduce to the mechanism would make it indeterminate. This is an issue that would need to be mitigated with additional elements, that would necessarily increase its complexity.

Another solution for B2IH needs to be found.

5.1.3. Telescopic B2IH

A couple of pantographic-specific B2IHs has been studied, and the results have been unsatisfactory, either because of the sizable additional parts the B2IHs introduced, or due to compatibility issues. Therefore, the focus is shifted to conventional B2IHs hereinafter. There is a B2IH mechanism that have been already designed for the VIS DST, and could be easily updated to be compatible with the TIR baffle, namely the radial part of Arink's telescopic baffle [5], shown in Figure 5.5.

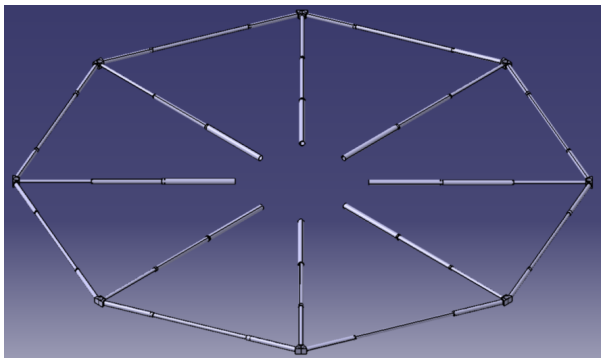

Figure 5.5: *The radial part of Arink's telescopic baffle. [5]*

Arink's radial telescopic design consists of 8 telescopic booms with deployment ratio of 3, and the initial hollow cylindrical cross-section has been modified to hollow square cross-section to achieve higher strength-to-weight ratio [5].

Some design elements from Arink's design is reused:

- The cross-section is kept as square to utilize its higher strength-to-weight ratio.
- 8 telescopic booms are used to connect all vertices of the octagonal baffle.
- The bigger boom segment's outer side length is kept at $b_{1,out} = 20$ mm.

The following have been changed:

- All 8 booms are of equal length, and they are rotated by 22.5° about the longitudinal axis of the telescope. This is necessary because the octagonal baffle is rotated as well to save volume.
- The wall thickness of the telescopic segments are 1 mm, which is an increase from Arink's design (1: 0.55 mm, 2: 0.54 mm, 3: 0.885 mm [5]).

- The deployment ratio is closer to 2 than 3, therefore two telescopic segments are preferred, which would decrease complexity.
- The clearance between telescopic segments is reduced to 1 mm (compared to 1.45 and 1.46 mm [5]).

The values above serve as initial inputs, and if needed, can be changed during iterative design. The simplified configuration of the radial telescopic booms are presented in Figure 5.6. Based on the baffle and instrument housing geometry, l_{st} = 313.5 mm and l_d = 638.6 mm, and the deployment ratio is l_d/l_{st} = 2.04. This is very close to 2 but still greater than that, which means a telescopic boom consisting of 2 segments cannot be designed with these input data, but designing one with 3 segments seems disproportionate and would introduce unnecessary complexity.

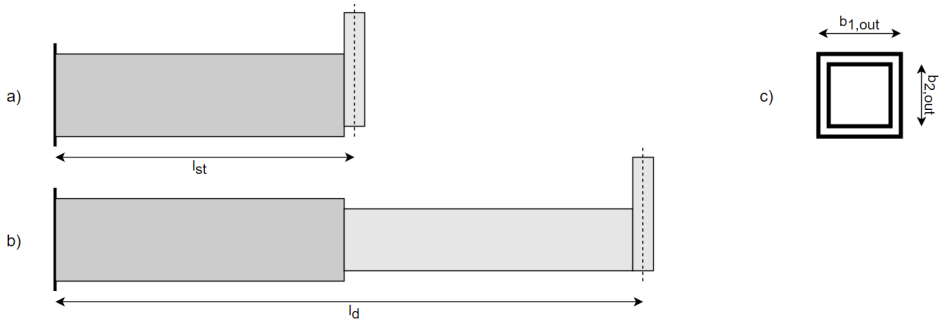

Figure 5.6: *Simplified configuration of the telescopic booms in a) stowed and b) deployed configuration, and c) its cross-section. l_{st} and l_d: stowed and deployed length, $b_{1,out}$ and $b_{2,out}$: outer side length of the outer and inner segments.*

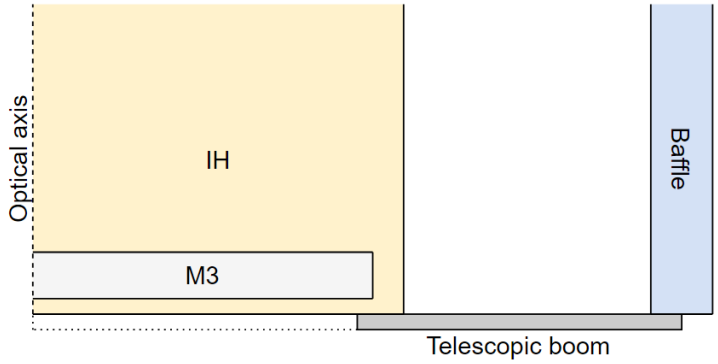

Figure 5.7: *Simplified side view of the telescope with telescopic B2IH mechanism.*

The solution to reach a deployment ratio of lower than or equal to two is to increase the length, for example by utilizing the space between the sides of the instrument housing and M3. However, as the space is limited there (32.7 mm radial distance), another solution is to move the telescopic B2IH mechanism below the instrument housing (see Figure 5.7), and this way the baffle structure remains at its predefined position (its bottom is coincident with the original bottom of the IH). The instrument housing (that is currently in its preliminary design stage) can be elongated to include the height of the telescopic booms (dotted lines in Figure 5.7). This would increase the telescope height by 20 mm, which is a 2% increase to the stowed height and volume, and considered to be acceptable. The radial intrusion of the telescopic booms into the instrument housing is limited, therefore it is not expected to affect the integration of the telescope to the spacecraft bus.

With 345.15 mm long telescopic segments, the required deployment can be realized with 34.19 mm radial intrusion to the the instrument housing (see Figure 5.8a-b), and with 20 mm deployed common length that ensures the rigidity of the boom. That 20 mm common length is shared between the outer and inner segment, with 2x10mm long contact surfaces (see Figure 5.8c) on both segments. During deployment and stowage only these surfaces are in contact with the other segment. To increase the deployed stiffness and prevent boom retraction, a latch-pin system is added to the sides of the booms, shown simplified in Figure 5.8c. The latch-pin design is similar to the one in Figure 5.9, but a simpler solution is enough as there is no third telescopic segment that needs to be kept in space until the middle one latches.

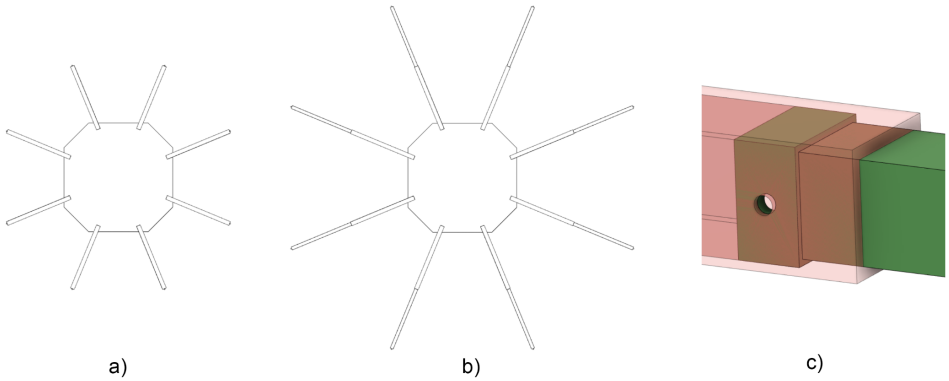

Figure 5.8: *Telescopic B2IH mechanism in a) stowed and b) deployed configuration, shown from the bottom. c) The common part of the two segments in deployed configuration, with holes for a latch-pin.*

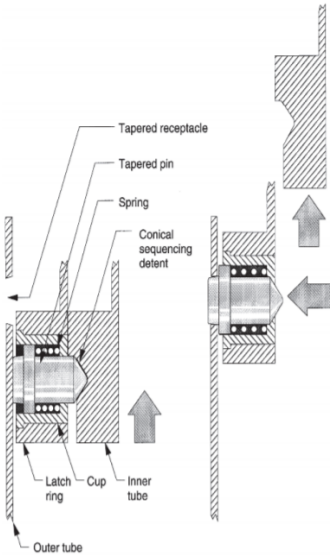

Figure 5.9: *Example of tapered pins used for latching. [33]*

The B2IH attaches to the angulated arms' middle rotational points with a simple pin, around which the angulated units can rotate. The pins at the end of the telescopic booms are depicted in Figure 5.6.

Al-Li 8090 is selected for the material of the booms. This material has been chosen for the pantographic arms because of its high specific stiffness and low density, and these material properties are desirable for the telescopic booms as well. Where sliding contact surfaces are situated, it is recommended to decrease the coefficient of friction. Linear bearings might as well be used, however, there is a much simpler solution. By coating the sliding surfaces with PTFE the coefficient of friction is reduced greatly, and no extra components are required (Al on Al, clear and dry, $\mu_{static} = 1.05-1.35$. PTFE on steel, clean and dry, $\mu_{static} = 0.05-0.2$ [46]. Only static coefficient of friction was available for both material pairs, and steel was the only metal available with PTFE.) PTFE is a synthetic polymer that is widely used on Earth and in space for its low coefficient of friction [10]. It withstands temperatures from cryogenic to 260 °C [10], which range is not expected to be exceeded within the DST baffle. The two 10 mm long sliding surfaces are enough to be coated by PTFE, as it slides well on metals (given an adequate surface preparation). The usual coating thickness (typical: 1 mil = 0.0254 mm [9]) does not affect the bulk material properties. The pins at the end of the telescopic booms are also coated with PTFE as the angulated units rotate around it.

The designed telescopic B2IH mechanism attaches the baffle to the instrument housing, and supports it in stowed and deployed configuration, and during deployment. The B2IH is interfaced with the baffle at the bottom radial module's vertices (middle rotational points of the angulated arms), thus there is no possibility for the baffle and the B2IH to be incompatible.

Because of the deformation-free deployment the telescopic B2IH is selected. A hybrid solution might be

counter-intuitive first, but they complement each other: a pantographic baffle with telescopic B2IH preserves all the positive properties a pantographic structure offers (synchronous deployment, minimum number of actuators: 1), and the baffle mechanism can deploy the B2IH (and vice versa) if needed. The telescopic B2IH offers a deformation-free deployment, and is preferred for its simplicity.

5.2. Radial - Axial Module Integration

The integration between the radial and axial modules needs to be solved in a manner that supports both compatible deployment and stiff connection. The relative orientation of the modules are shown in Figure 3.48. In the TIR axial module design in Section 4.4 it has been decided to keep the angle between the radial and axial modules constant, therefore making their integration easier. Ultimately, the connection needs to be made between the end rotational points of the axial modules and the end rotational points of the angulated arms in the radial structure. For a deployable pantographic cylinder prototype [35] a simple joint has been developed for the integration of the radial and axial modules, see Figure 3.23.

When designing such joints, one should consider that the arms have tangible volume, and they are no more represented by lines and the joints by dots. The joints "have to to interconnect a spatial configuration of multiple scissor units and enable the correct rotational motion of each unit, usually about different rotational axes" [42]. The spacial configuration of the modules are presented in Figure 5.10. The 74.173° angle between the axial and radial modules is prescribed by the axial module design. In the figure the arms have thicknesses, and the end rotational points are represented as rectangles. If the modules didn't have thicknesses, the axial module could directly attach to the radial module, and the red dotted line would go through the intersection of the blue and green dotted lines. But the modules do have thicknesses, and the arms cannot coincide. Therefore, the axial module needs to be moved higher (as shown in Figure 5.10), and the connection between the end rotation rectangles (instead of points) need to be facilitated. Moving the axial module higher does not affect the global geometry or kinematics of the structure, but it introduces eccentricities that should be kept at minimum from structural point of view [42]. Consequently, the two rotational rectangles should be as close to each other as possible.

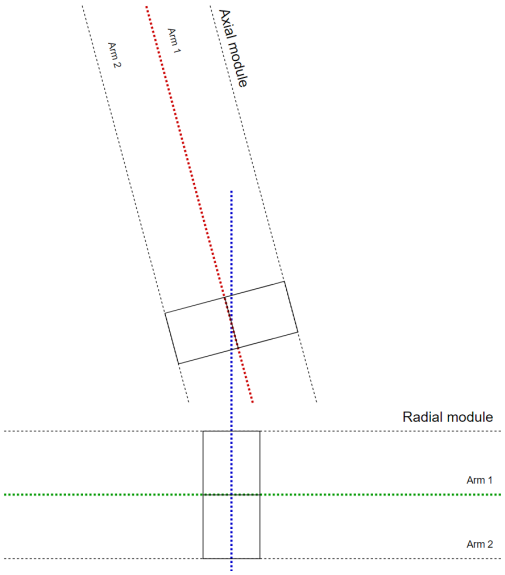

Figure 5.10: *Conceptual side view of the integration of the radial and axial pantographic units.*

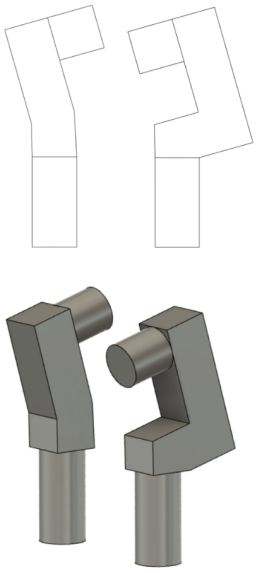

Figure 5.11: *Simple joints to connect the axial and radial modules. Top: 2D, bottom: 3D view.*

The simplest geometries that could connect the end rotation rectangles are shown in Figure 5.11. Two different joints are required to connect the axial module to the radial module because of the asymmetries introduced by the angled axial module, see Figure 5.12. If the design was symmetrical (right angle between the modules), the same joints could have been used.

For now, the joint thickness is considered to be 5 mm (same as the thickness of the arms), and the material is considered to be the Al-Li 8090, the same material that is used for the arms. If later structure analyses prove the thickness to be insufficient, it can be changed in a later stage. As sliding surfaces are required, the

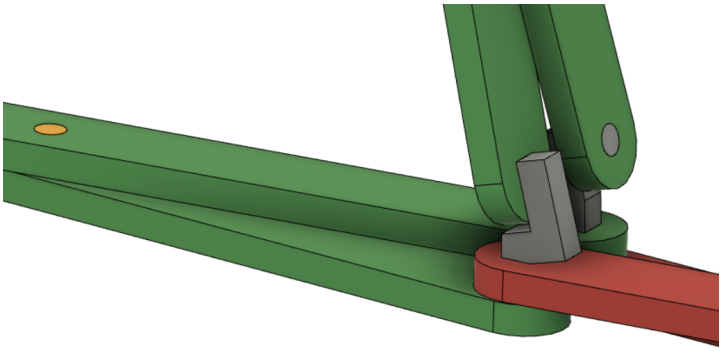

Figure 5.12: *Joints (grey) connecting the axial and radial modules, and pins (yellow) connecting the pantographic arms.*

cylindrical parts of the joints – that serve as rotational pins for the arms – are coated with PTFE.

Similarly to this, the rest of the rotational joints in the structure are connected with Al-Li 8090 pins, with the sliding surfaces coated with PTFE, see Figure 5.12.

At this point of design nothing stops the joints and pins to slide out of the holes of the pantographic arms. This is accepted for now, but it is necessary to update their design in the future. The updated joints and pins are not foreseen to have considerably increased mass compared to the current designs.

5.3. Design Optimization

The pantographic arms and other parts of the structure have been treated as functional parts with fixed geometries so far, however, their geometries have not been optimized. In this section an iterative optimization of the baffle elements is presented.

5.3.1. Initial Setup

Based on the previously designed parts (pantographic arms, joints, and B2IH mechanism) the 3D design of the baffle is built. The mass of structure is summarized in Table 5.1, and the baffle in stowed and deployed configuration is presented in Figure 5.13.

Table 5.1: *Mass of the initial (unoptimized) setup of the baffle.*

Part	Mass/piece, g	Quantity	Total mass, kg
Radial - angulated arm	38.802	32	1.242
Radial - straight arm	34.905	96	3.351
Axial - straight arm	34.578	176	6.086
R2A joint - bigger	2.119	32	0.068
R2A joint - smaller	1.751	32	0.056
B2IH - inner tube	54.438	8	0.436
B2IH - outer tube	66.861	8	0.535
Pin	0.511	392	0.200
Total			**11.973**

Modal analyses have been performed on the initial setup in both configurations, and its results are shown in Table 5.2. The legacy stiffness requirements from the TIR DST state that the first eigenfrequency in deployed configuration shall be at least 0.9 Hz, and in stowed configuration at least 100 Hz. It is foreseen that

Table 5.2: *Eigenfrequencies of the initial setup.*

	1st eigenfrequency, Hz	2nd eigenfrequency, Hz	3rd eigenfrequency, Hz
Stowed	25.1	33.4	35.9
Deployed	13.8	24.9	26.4

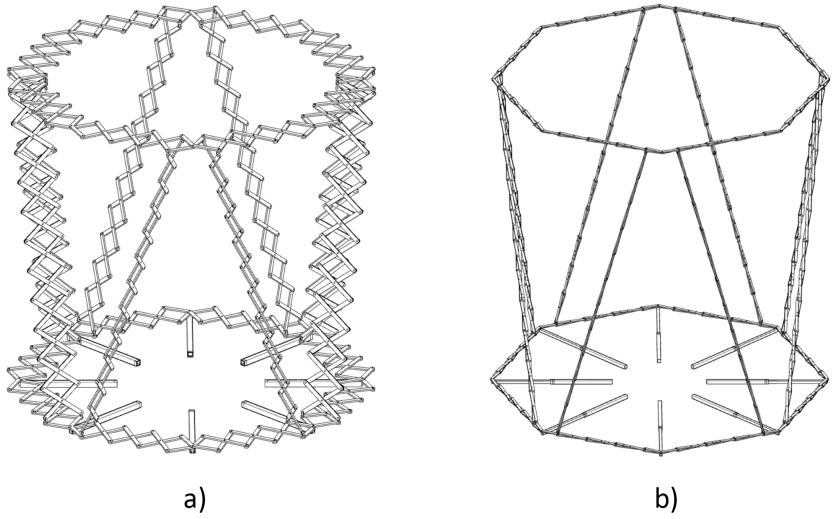

Figure 5.13: *Initial (unoptimized) setup of the baffle in a) stowed and b) deployed configuration (scale to each other: 1:1.47).*

these requirements do not change with the change to the TIR telescope. The deployed eigenfrequency requirement is easily met (13.8 Hz), however, the first eigenfrequency is stowed configuration (25.1 Hz) fails to meet the requirement. Consequently, optimization is required: the first eigenfrequency in stowed configuration needs to be increased, and the one in deployed configuration can be reduced, as overachieving the requirement does not bring any advantage to the design, but it usually means that there might be an opportunity to reduce the mass of the structure.

5.3.2. Iterative Optimization

The eigenfrequency of a spring-mass system is calculated the following way:

$$f_0 = \frac{1}{2\pi}\sqrt{\frac{k}{m}} \tag{5.3}$$

where k is the stiffness of the spring, and m is the mass. Generally, the mass and stiffness of a structure affects the eigenfrequency in a similar manner:

$$f_0 \propto \sqrt{\frac{\text{stiffness}}{\text{mass}}} \tag{5.4}$$

Based on Equation (5.4) there are two ways to increase the eigenfrequencies: by increasing the stiffness of a structure, and by reducing its mass. The two methods often affect each other (e.g. stiffness can be increased by adding mass to the structure), so the optimization needs to be done in a way that the greatest stiffness increase is achieved with least added mass, or the maximal mass reduction is achieved with the least expense to the stiffness.

The eigenfrequency requirement is not met in stowed configuration, therefore the studies focus on this configuration. Different parts of the structure are analyzed individually to better understand the effect of certain changes, and to accelerate the FEM iteration cycles.

Axial Module

First the axial module was analyzed. Its long and thin construction makes it susceptible to low eigenfrequency. The stowed axial module, consisting of 11 pantographic arm pairs, was fixed by the two end rotational holes on one end of the structure. The modal analysis has been performed, and the results are shown in Table 5.3. Then, several iterative steps have been made to improve the eigenfrequencies. The iterations focused on increasing the stiffness of the structure normal to the module plane, while reducing the arm width, as in that direction the structure proved to be much stiffer, and the material usage could be reduced there. The iteration results are presented in Figure 5.14, which shows the axial straight arm that proved to have the highest eigenfrequency (when the axial module is built out of them). The following properties of the arm have been empirically optimized, with the final values in parentheses:

- Radius of the arm lightening cutout (smallest arm thickness: 4 mm),
- Thickness of the top reinforcement (3.5 mm),
- Maximum height of the top reinforcement (5.5 mm).

Only one side of the arm could be altered thickness-wise, as the other side is in contact with the connecting pantographic arms. The hole diameters and arm thicknesses around them have been left untouched in order not to change the pantographic module global properties.

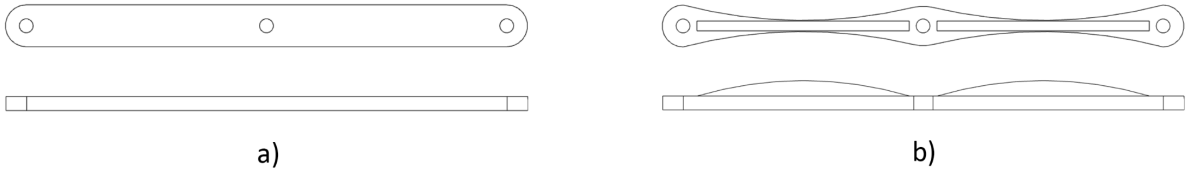

Figure 5.14: *a) Initial and b) optimized design of the axial straight arm.*

Table 5.3: *Mass of an arm and the first three eigenfrequencies of axial straight module with initial and optimized arm design.*

	Mass (one arm), g	1st eigenfreq., Hz	2nd eigenfreq., Hz	3rd eigenfreq., Hz
Initial	34.58	45.48	66.02	135.3
Optimized	23.36	54.49	60.27	115.8

The comparison between the initial and the optimized design is shown in Table 5.3. 20% increase in the first eigenfrequency has been achieved while reducing the mass of the arms by 32%. The optimization also showed that although the first eigenfrequency has been increased, but not to a large extent.

Radial Module

The radial module consists of angulated and straight arms, connects the baffle to the B2IH mechanism, and supports the axial module (through the joints) as well, which makes its optimization more complicated. To limit the model complexity (to improve simulation duration), a reduced radial module shown in Figure 5.15 is used. The structure is fixed at the middle rotational holes of the angulated units, and the proportional mass of the rest of the baffle (top radial module and 8 axial modules) is divided among the end rotational holes of the angulated arms as point masses.

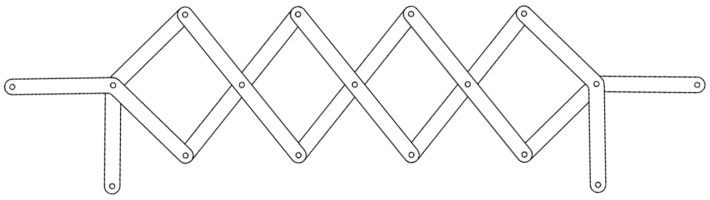

Figure 5.15: *Reduced radial structure for optimization iterations.*

The optimization process started with the straight arms, in which the experiences with the axial straight arms proved to be helpful. The process was identical to the previous one, therefore only the results are presented in Figure 5.16b.

Based on the initial first eigenfrequency and the mode shapes, the angulated arms were the weakest link in the structure. These are the ones that connect the baffle to the B2IH mechanisms, and these support the axial modules. During the iterative process it has been proven that the angulated arms need to be stronger and more massive than the rest of the arms to successfully fulfill the mentioned tasks. Several different design variations have been analyzed, which ultimately resulted in the final design shown in Figure 5.16d. The end rotational holes needed to be kept at the initial thickness to maintain its compatibility with the rest of the baffle. The thickest part of the arm is 10.5 mm, the same as the greatest thickness of the rest of the optimized arms.

With the presented modifications in the radial module, the masses of the arms and the change of eigenfrequencies are shown in Table 5.4. The 91% increase in the mass of the angulated arm is expected after making

it stronger, but with making the straight arms 32% lighter, the mass of the bottom radial module (made of 16 angulated and 48 straight arms) has increased only by 1.4%. The eigenfrequencies of the reduced radial structure are not representative for the entire baffle, but they are useful to compare the different iterations: the optimized design more than doubled its first eigenfrequency.

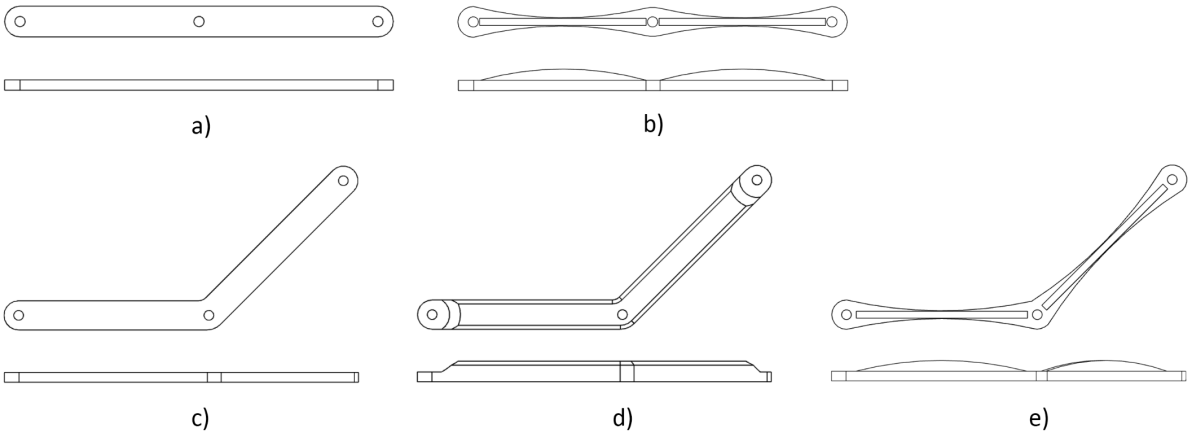

Figure 5.16: *a) Initial and b) optimized design of the radial straight arm. c) Initial design of the radial angulated arm, and its optimized version for d) the bottom and e) top radial module.*

Table 5.4: *Mass of one radial angulated and straight arms and the first three eigenfrequencies of the reduced radial structure shown in Figure 5.15 with initial and optimized arm design.*

	Mass (one ang. arm), g	Mass (one str. arm), g	1st eigenfr., Hz	2nd eigenfr., Hz	3rd eigenfr., Hz
Initial	38.80	34.91	3.08	5.55	14.43
Optimized	74.04	23.82	6.39	14.45	19.92

The presented angulated arm is a necessary upgrade for the bottom radial module, but it is futile for the top one, moreover, the added mass makes it even harmful. Therefore, another angulated arm design has been prepared for the top radial module, which bears similar design traits as the straight arms, see Figure 5.16e.

B2IH

The telescopic segments of the B2IH mechanism were originally 1 mm thick, but the first modal analysis including the entire baffle and B2IH showed that the rigidity of the B2IH needs to be improved: vertical bending of the B2IH was the first mode shape. In deployed configuration the initial design was overperforming, which suggested that the B2IH is good enough in deployed configuration. Therefore, the B2IH needs to be reinforced only for stowed configuration, and more specifically, the outer segment needs to be strengthened for the following reasons:

- The inner segment is surrounded by the outer segment, and extra mass added to the outer side of the structure is more effective to achieve higher rigidity,
- The inner segment moves away from the fixed side of the B2IH during deployment, and if extra mass was given to it, the eigenfrequencies in deployed configuration would be reduced.

In the modal analysis the stowed configuration of the B2IH is modelled with the outer segment's side facing the instrument housing fixed, and 1/8 of the baffle mass placed on the end pin as a point mass. The initial configuration is shown in Figure 5.17a. During the iterations the geometry of the outer segment is modified until the first vertical mode shape with eigenfrequency of 100 Hz is achieved in a mass-efficient way. The horizontal mode shapes are expected to gain higher eigenfrequencies when the whole baffle is modelled because of the horizontal support of the radial module. 100 Hz eigenfrequency is not expected to be translated to 100 Hz in the model with the entire structure, but it served as a semi-arbitrary goal for the optimization.

The optimized result is illustrated in Figure 5.17b, while the achieved eigenfrequencies and masses are shown in Table 5.5. The additional reinforcement hollow square tube attaches to the side of instrument hous-

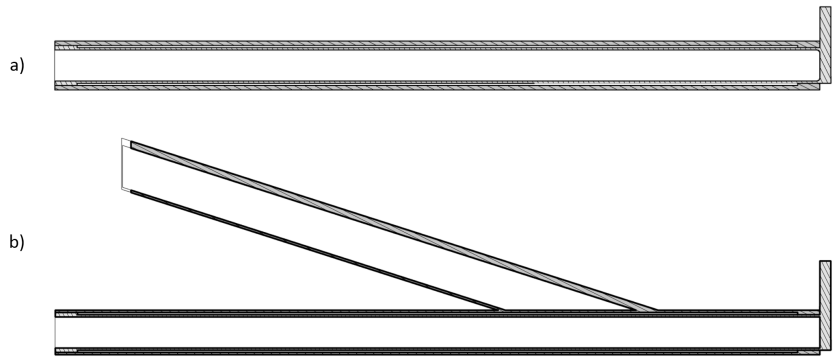

Figure 5.17: *a) Initial and b) optimized design of B2IH mechanism (section view).*

ing. The eigenfrequency with the first vertical mode (initial: 1st, optimized: 2nd eigenfrequency) has been increased by 163%, while the mass of the outer section has been decreased by 6%.

Table 5.5: *Mass of the outer section and the first three eigenfrequencies of the B2IH mechanism with initial and optimized design.*

	Mass (outer section), g	**1st eigenfr., Hz**	**2nd eigenfr., Hz**	**3rd eigenfr., Hz**
Initial	142.56	38.3	42.1	199.9
Optimized	134.18	36.7	100.7	180.7

5.3.3. Discussion

The optimized setup of the baffle is illustrated in Figure 5.18.

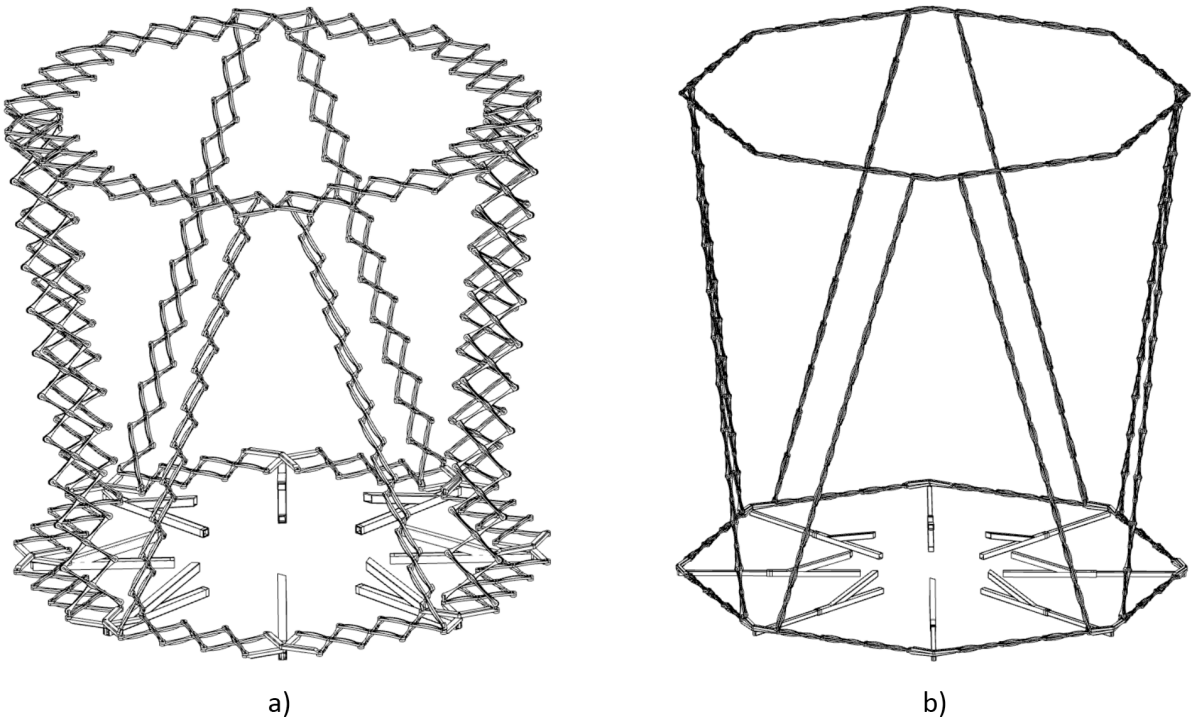

Figure 5.18: *Optimized setup of the baffle in a) stowed and b) deployed configuration (scale to each other: 1:1.47).*

With the presented optimizations the eigenfrequencies shown in Tables 5.6 to 5.7 have been achieved. 63% increase has been achieved in stowed configuration, which is considerable, but still not good enough for the 100 Hz requirement. The optimization process brought the increase of the deployed eigenfrequencies as

well, which now overachieves the 0.9 Hz requirement 20 times.

Table 5.6: *Eigenfrequencies of the optimized structure and the optimized structure supplemented with point masses and hold down constraints in stowed configuration.*

	1st eigenfr., Hz	2nd eigenfr., Hz	3rd eigenfr., Hz
Initial	25.1	33.4	35.9
Optimized	41.0	42.7	54.4
Optimized + point masses + constraints	103.2	108.7	109.7

Table 5.7: *Eigenfrequencies of the optimized structure and the optimized structure supplemented with point masses in deployed configuration.*

	1st eigenfr., Hz	2nd eigenfr., Hz	3rd eigenfr., Hz
Initial	13.8	24.9	26.4
Optimized	18.0	33.0	34.8
Optimized + point masses	16.2	24.6	25.7

The masses of the optimized structure is shown in Table 5.8. Compared to the initial baffle design a substantial 16.4% reduction has been achieved (1.9 kg).

Table 5.8: *Mass of the optimized setup of the baffle frame.*

Part	Mass/piece, g	Quantity	Total mass, kg
Radial - angulated arm (top)	26.28	16	0.42
Radial - angulated arm (bottom)	73.24	16	1.17
Radial - straight arm	25.58	96	2.46
Axial - straight arm	23.36	176	4.11
R2A joint - bigger	2.12	32	0.07
R2Ajoint - smaller	1.74	32	0.06
B2IH - inner tube	56.59	8	0.45
B2IH - outer tube	134.18	8	1.07
Pin	0.51	392	0.20
Total			**10.01**

After adding the shroud, the truncated cone, the actuation, and final locking mechanisms as point masses and the initial locking as constraints (see Sections 5.4 to 5.6) to the modal analysis, the eigenfrequencies have increased in stowed -, and decreased in deployed configuration, as shown in Tables 5.6 to 5.7.

The pantographic baffle has been designed in such a way that its designated stowed configuration is not its smallest size, but rather a semi-deployed state. The pantographic arms could be modified (addition of interfering surfaces) to prevent the baffle size to be smaller than its stowed configuration. This modification is not foreseen to affect the mass of the arms significantly, but is recommended to make the stowed and held down structure stiffer. It is considered in this thesis that the baffle cannot get into a configuration that is smaller than its stowed configuration.

5.4. Actuation

In this section the deployment actuators are selected, along with the mechanisms that lock the structure in place in stowed and deployed configurations.

5.4.1. Deployment Actuation

One of the advantages of the pantographic structure is that if one of its angles or joint distances change, it affects the rest of the angles and joint distances of the structure in the same way. The addition of the B2IH mechanism does not change this behavior, it is integrated to the baffle in a way that even if just a telescopic

arm in the B2IH is moved, the entire structure follows. Because of this, only one actuator is enough to deploy the whole baffle. However, additional actuator(s) need to be added for redundancy. Multiple distributed actuators are advantageous to reduce internal stresses during deployment as well.

The deployment force that the actuators provide needs to overcome the friction in the joints and between the contacting arm surfaces. These joints and surfaces are coated with PTFE to reduce the required force. The determination of the required force is not part of this thesis, but it is recommended to be checked analytically and with a (scaled) prototype in the future.

The deployment actuation can be passive or active. Active deployment actuation techniques include:

- **Linear actuators.** The group involves all kind of actuators that provide linear motion, including for example a lead screw - nut combination. The common working principle of these actuators is that they adduct two adjacent unconnected joints, as it is shown in Figure 5.19.

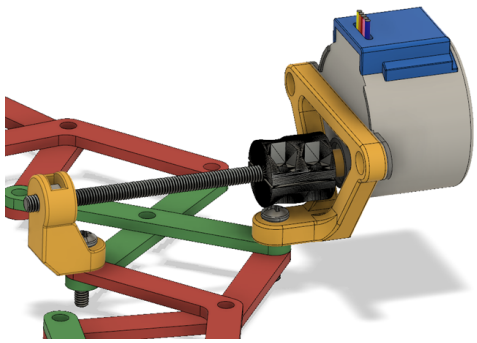

Figure 5.19: *Example of a linear baffle deployment actuator. [35]*

- **Rotary actuators.** These actuators adduct the ends of connected pantographic arms. The rotational axis is the common rotational hole of the arms.
- **Cable.** A long cable runs through a series of pulleys along the pantographic structure, and by shortening the cable the structure is deployed. Cable shortening is usually done by a mechanised drum, see Figure 5.20.

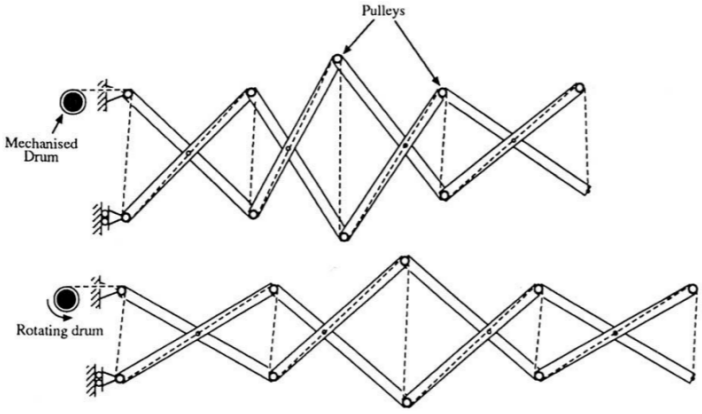

Figure 5.20: *An example for cable-driven pantographic deployment. [28]*

Deployment with a cable has the advantage that it acts on multiple joints (in theory even all is possible) synchronously, thus minimizing the internal stresses the deployment process would cause. On the other hand, having a redundant cable system in place greatly increases the complexity of the whole baffle.

The passive deployment techniques are:

- **Linear springs.** Similar to active linear actuators, linear springs adduct adjacent unconnected joints with a spring in tension.

- **Rotary springs.** Rotary springs are placed at the rotational points of the pantographic mechanisms, and they apply torque on the arms, trying to adduct them.
- **Flexible composite hinges.** Pantographic structures can be modified to incorporate flexible composite hinges instead of pins, which aim to return to their minimal energy state (deployed configuration) after setting free, see Figure 5.21 [51].

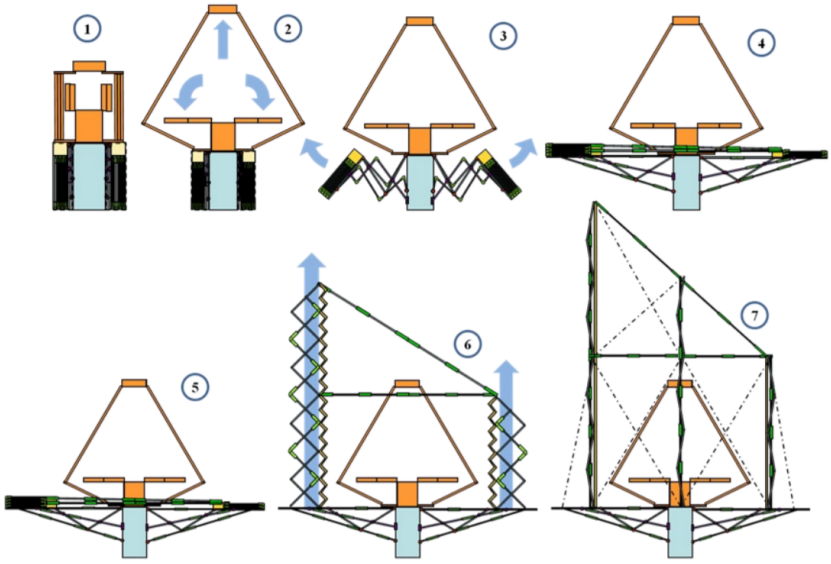

Figure 5.21: *SEDOBA telescope deployment sequence with flexible composite hinges (green). [51]*

Flexible composite hinges offer a great solution for passive deployment as it can be integrated to the pantographic structure seamlessly. However, in order to be able to do that, the pantographic modules need to be redesigned so that one arm of each pantographic unit (connected by the composite hinges) situates in one straight line, see step 7 in Figure 5.21.

Passive deployment actuators are usually preferred to active ones in space for reliability reasons. For the same reason the deployment actuator for the baffle is selected from the passive actuators. As mentioned, flexible composite hinges are great alternatives, but they require redesign from the beginning, consequently it is excluded from the options. However, when designing a pantographic baffle from the beginning, the flexible composite hinges should be considered.

Between linear and rotary springs, the rotary ones are preferred as linear springs accommodate a considerable space even when they are not in tension, and in deployed configuration the distance between the arm rotational points are just 15 mm (Figure 5.22). In this sense a rotary (torsion) spring takes up less space, and it can be placed on the top of joint that connects the arms. Furthermore, a rotary spring can provide torque even after deployment that keeps the structure deployed, or facilitates latching (based on the selected solution). On the other hand, where only linear motion is applicable, and there is enough space to accommodate it, a linear spring is a viable option.

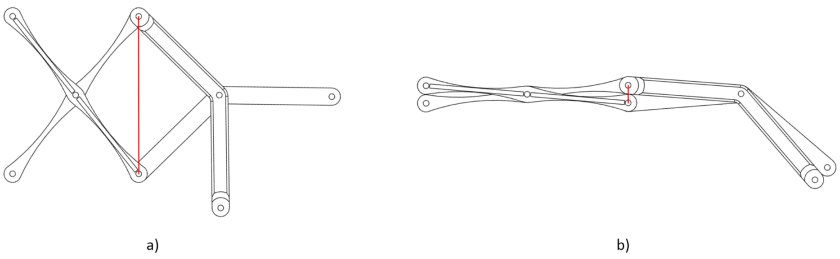

Figure 5.22: *Simplified linear spring (red) between pantographic arms in a) stowed and b) deployed configuration.*

For the placement of the actuation springs the following objectives are considered:

1. The amount and placement of the springs should allow for a deployment with minimal internal stresses.
2. The amount of springs should be minimized.
3. The placement of the springs should consider their effect on the stiffness of the structure.

Point 1 would aim for a spring at all joints, while point 2 seeks the opposite, consequently an optimized solution needs to be found. Point 3 highlights that the placement of the springs affects the stiffness of the structure (by preloading it), therefore it needs to be carefully considered. The least free-standing joints are favored.

Based on these, the springs shown in Figure 5.23 are added to the baffle. At the bottom of the baffle there are two options: placing linear springs inside the telescopic sections of the B2IH mechanism, or torsional springs at the vertices of the octagon. The second option requires smaller springs, and to save mass, this is utilized. By changing the angle between the angulated arms the radial module is deployed, which then deploys the axial modules. As the diameter of the radial module increases, the B2IH mechanism is deployed as well. All of the mentioned deployed modules are connected by the reinforced angulated arms, therefore kept close to each other, thus maximizing the efficiency of sharing the common deployment state. Half of the telescopic B2IH mechanisms are used: the four that are attached to octagonal vertices with axial module connection actuate the deployment, the rest follow it. At the top radial module four torsion springs are placed to vertices with axial module connection, again, to facilitate the deployment of not only the top radial module, but of the axial modules as well. There are no springs placed in the axial modules, but they are actuated from both ends indirectly by the utilized springs.

With 8 springs distributed symmetrically in the baffle, the deployment objective aiming form minimal internal stress is achieved. As discussed earlier, only one actuator is enough to deploy the baffle, but for redundancy and to minimize the internal stresses eight have been used. Compared to the more than 400 joints used in the baffle, eight is an acceptable number. These actuators have been placed in the baffle in a manner to adhere to point 3 in the objectives: they are at the most supported regions of the baffle.

The number and the required strength of the springs are recommended to be tested and verified on a (scaled) prototype, furthermore, when more data is available, damping is recommended to be introduced to the system to limit the deployment speed of the baffle.

Without selecting the actual torsion springs, 0.1 kg is budgeted for the mass of the springs and structure modifications to accept the springs. The mass of one spring is not expected to exceed 10 g.

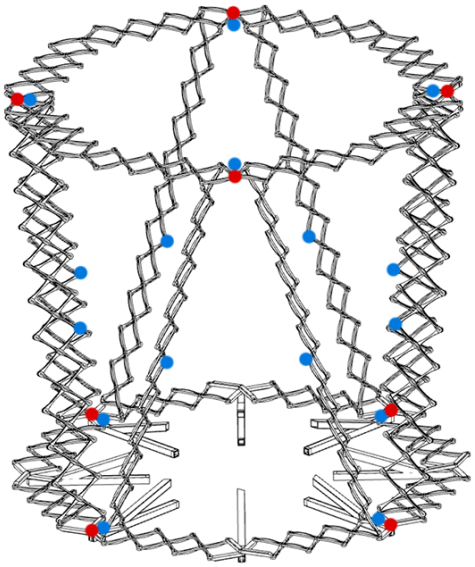

Figure 5.23: *Placement of the actuators (red) and hold down points (blue) in the baffle.*

5.4.2. Initial Locking

Without initial locking, there is no mechanism in the baffle to prevent the passive actuators from deploying the baffle. However, the baffle deployment initiation needs to be controlled, so hold down and release mechanisms (HDRMs) are introduced to the system. As their name suggest, these mechanisms hold down the

structure until the release command, then they release the locking. Many types of HDRMs exist, they can be explosive or non-explosive, and based on their operation principle there are pin pullers, pin pushers, explosive nuts, wire cutters, etc. It is advantageous to hold down the structure close to the actuation points to limit the internal stresses. Furthermore, additional HDRMs is used to clamp the stowed baffle to the instrument housing in order to increase its rigidity. Based on this, 8 hold down points are required for the baffle close to the actuators, and additional 8 in the axial modules (one/module) to increase the stowed rigidity.

It is easy to solve the initial locking close to the bottom actuators by locking the B2IH mechanism as it is close to instrument housing and directly connected with it, therefore (electrical) wire routing is not a problem. Also, several types of HDRMs can be used: a pin puller could hold the inner segment locked in the outer segment in stowed configuration with a pin, and when the release command arrives, it pulls the pin out, initiating the deployment. Another solution is locking the inner segment in the outer segment with a cable, and upon arrival of the release command the cable is cut, e.g. with a thermal knife.

Locking the stowed structure close to the torsion springs in the top radial module is more difficult. These actuators are far away from the instrument housing, and only connected to it through a long series of pantographic linkages. Placing a HDRM in the top radial module is disadvantageous, as the added mass of the mechanism and the electrical wires would have a negative impact of the eigenfrequencies of the baffle. A cable connecting the actuated vertices of the top radial module and the top part of the instrument housing can keep the structure locked in stowage, and cable cutters can be attached to the instrument housing. However, after cutting the cables the longer part of them remain attached to the vertices at one end, while the other floats freely. This is unacceptable as it potentially degrades the optical performance of the telescope. One solution is to attach passive mechanized drums to the vertices that quickly reel up the cables after cutting. This process needs to be quicker than the deployment of the baffle, because a free cable might get stuck between moving pantographic arms, hindering further deployment. Similar to the HDRMs in the top module, the hold down mechanisms that increase the rigidity of the axial modules are cables that are actuated with cable cutters. The hold sown positions in the stowed baffle are presented in Figure 5.23.

To limit the added mass and complexity of the system, one HDRM with 2 redundant thermal knives is added to the four bottom actuators, and one to the four top actuators plus to the 8 hold down points in the axial module, making the required number of HDRMs two in total. A HDRM with 2 redundant thermal knives in Airbus Defence and Space Netherlands' lineup has 0.5 kg mass [12], making the total mass of the HDRM 1 kg. An additional 0.2 kg is considered for the supplementary elements (e.g. cables).

5.4.3. Final Locking

The springs keep the baffle in deployed configuration after deployment, however, to increase the rigidity of the structure, the final locking in deployed configuration is achieved by the usage of the already introduced latch-pins (see Figures 5.8 to 5.9). The latch-pins are placed close to the actuators to be unaffected by the deflection of materials. In the B2IH mechanism they are placed within the segments as shown in Figure 5.8c.

To lock the top angulated arms in deployed configuration, the arms are supplemented with holes for the latching pin, see Figure 5.24. For both latching solutions a latching pin is pushed to the surface of the connecting element by a preloaded spring. The latching pin does not stop the motion of the elements until reaching deployed configuration, and to minimize the friction PTFE coating is applied to the contact surfaces. When the elements reach their deployed position, the holes and the pins are aligned, and the spring pushes the pin into the hole, locking the elements together. Next to the eight actuators, eight latching pins are placed.

One latching mechanism is approximated to have 15 times the mass of a pin used in the pantographic structure. Based on this, the added mass of the latching mechanisms is 61 g.

5.5. Shroud Integration

The thermal design of the baffle has been left at the preliminary design stage in Section 4.3.10. There, the baffle cross-conductance has been selected to be $h_{eff} = 0.17$ W/m^{2}K, that roughly corresponds to 2 layers of MLI [3]. The exact cross-conductance with 2 layers of MLI depends on the perforations, area, and MLI mean temperature as well [13]. For now, the baffle shroud is designed with 2 layers of MLI, and when a detailed thermal design is available, the shroud design can be updated, too.

The shroud situates outside of the baffle frame. The outer rotational holes/pins of the baffle structure serve as natural attachment points between the shroud and the frame: in Figure 5.25 one side of the octagonal baffle is depicted, showing the positions of the outer pins. During deployment the movement of the outer pins deploys the shroud. Because of the axial module selection, the geometries laid out by the attachment points

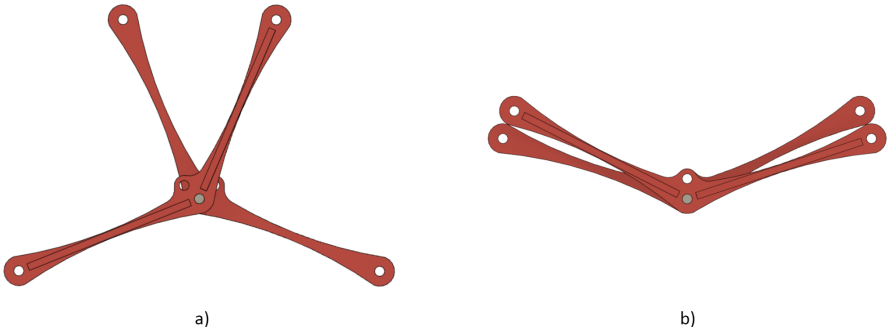

Figure 5.24: *Top angulated arms supplemented with holes for latching in a) stowed and b) deployed configuration.*

in stowed and deployed configurations are similar, and it facilitates the folding of the shroud.

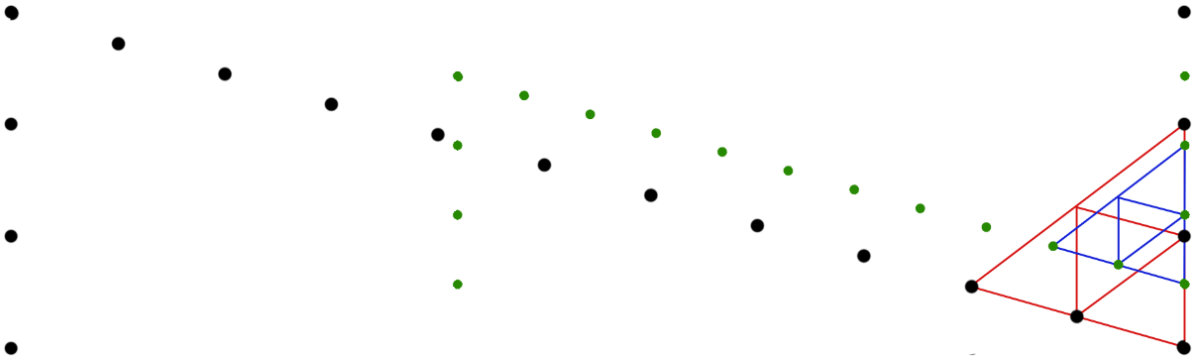

Figure 5.25: *Attachment point is stowed (green) and deployed (black) configuration. Part of lattice laid out by the attachment points are shown in blue for stowed and in red for deployed configuration. The figure is rotated by 90°.*

The mass of the MLI is calculated using Arink's MLI selection and properties [5]. With 146 kg/m^3 bulk density, 0.506 mm thickness, and 13.03 m^3 total MLI area, the mass of the MLI (shroud) is 0.96 kg. The attachment points are approximated to triple the mass of the pins, increasing the total mass of the baffle by 0.16 kg. The shroud outside the stowed baffle is approximated to add 10 mm to the baffle outer diameter on both sides, increasing it to 1342 mm.

5.6. Truncated Cone

The truncated cone recommended in the preliminary thermal design can be attached to the top radial module at the inner rotational points of the angulated arms. A modification of Arink's telescopic truncated cone segments (see Figure 5.26) can be implemented for the pantographic structure as well, the design is stowed configuration is shown in Figure 5.27. The attachment points keep the cone segments at a fixed 13.8° from vertical (specified in Section 4.3.10), and as they move away from each other during deployment, they increase the length of the truncated cone segments. As the geometry at the octagon vertices change during deployment, the truncated cone plates can only spread along the straight pantographic arms, and at the vertices a flexible and foldable material needs to be used.

The mass of the truncated cone segments with 0.5 mm thickness of Al-Li 8090 is 66 g, and twice of this mass is considered for the additional mass, including the attachments, reinforcements, and flexible parts. In total the mass of the truncated cone is 0.2 kg.

5.7. Mass Review

The total mass of the baffle assembly is shown in Table 5.9. If the budgeted mass of the VIS DST of 15 kg is kept, the total mass leaves 2,24 kg (17.6%) for safety margin and mass uncertainties. However, requirement BAF-SYS-06 prescribes 25% mass uncertainty margin, and it is not met.

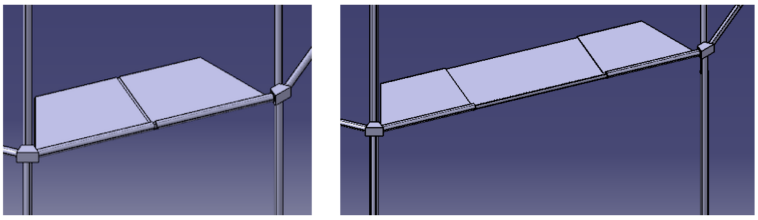

Figure 5.26: *Part of the truncated cone designed by Arink in stowed and deployed configuration. [5]*

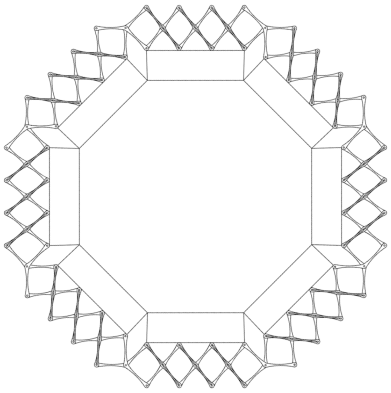

Figure 5.27: *Simplified top view of the truncated cone in stowed configuration.*

Table 5.9: *Mass breakdown of the baffle assembly.*

Part	Mass, kg
Frame	10.01
MLI + attachments	1.19
Truncated cone	0.20
Actuation	0.10
HDRM	1.20
Final locking	0.06
TOTAL	**12.76**

5.8. Discussion

In this chapter the mechanical design of the baffle has been worked out in greater details based on the preliminary mechanical and thermal design. First, the baffle has been integrated to the instrument housing in a way that it supports the baffle in all deployment states. Then, the connection between the axial and radial modules has been worked out, followed by the design optimization of the pantographic arms and other baffle elements. Next, the passive actuation has been designed, along with the systems for initial and final locking. After that, the baffle shroud and the truncated cone have been integrated to the baffle frame.

The final design of the pantographic baffle is presented in Figure 5.28 in stowed, and in Figure 5.29 in deployed configuration. The final mass of the baffle assembly is 12.76 kg, which conforms to the 15 kg mass budget, but does not have 25% mass uncertainty budget that is prescribed by the requirements. The stowed volume of the telescope is 1.7 m^3, which exceeds the 1.5 m^3 budget by 13%. The mentioned mass and volume budgets are a heritage of the VIS DST, and have not been updated. When new budgets are available for the TIR DST, the mass and volume (and the decisions leading to these values) can be critically reviewed, and the severity of the (possible) budget exceedance be weighed on systems level. If the volume is deemed to be too high, the height of the baffle can be decreased on the expanse of baffle complexity, which is – again – a systems engineering decision.

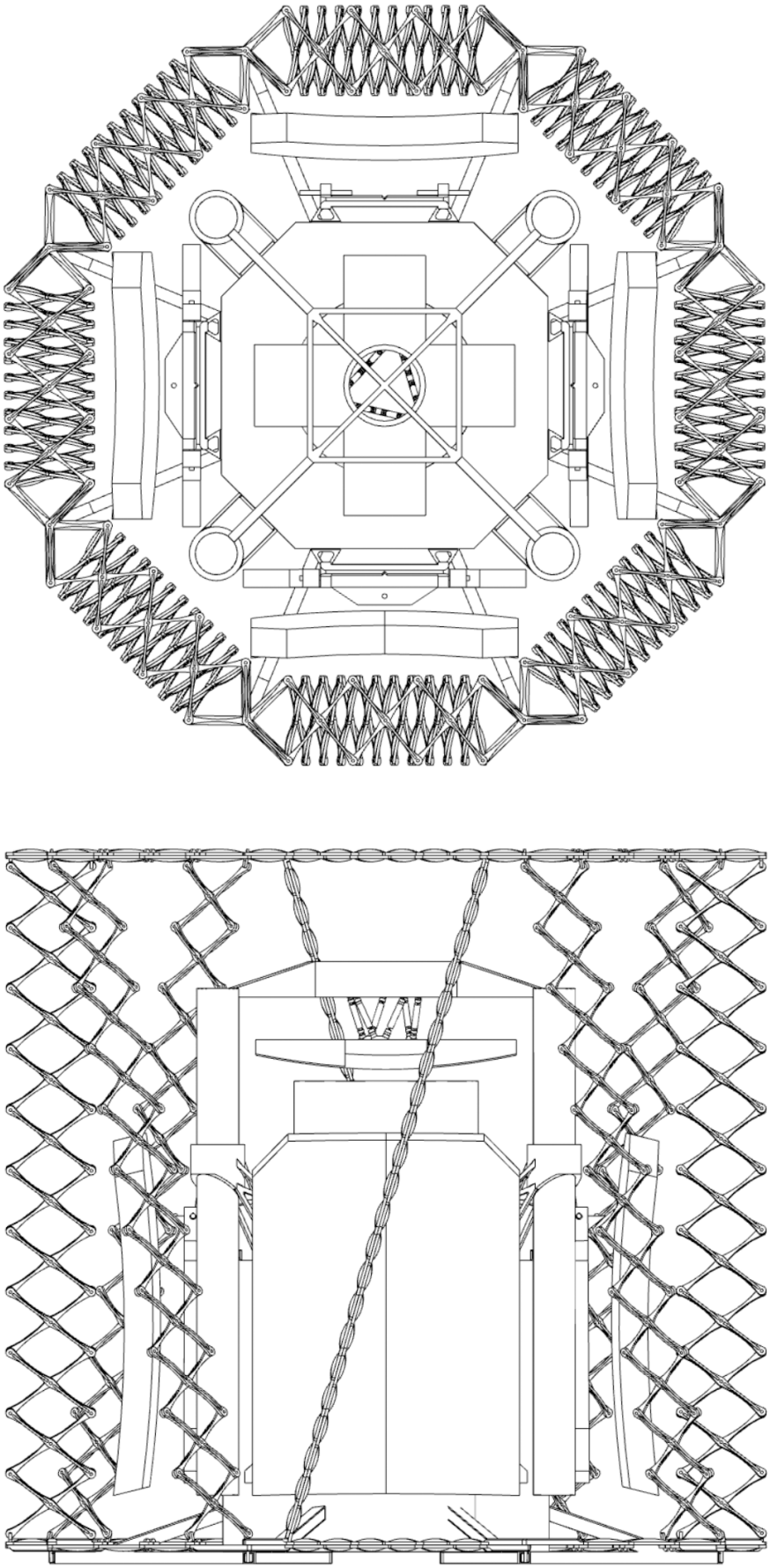

Figure 5.28: *Final pantographic baffle design in stowed configuration.*

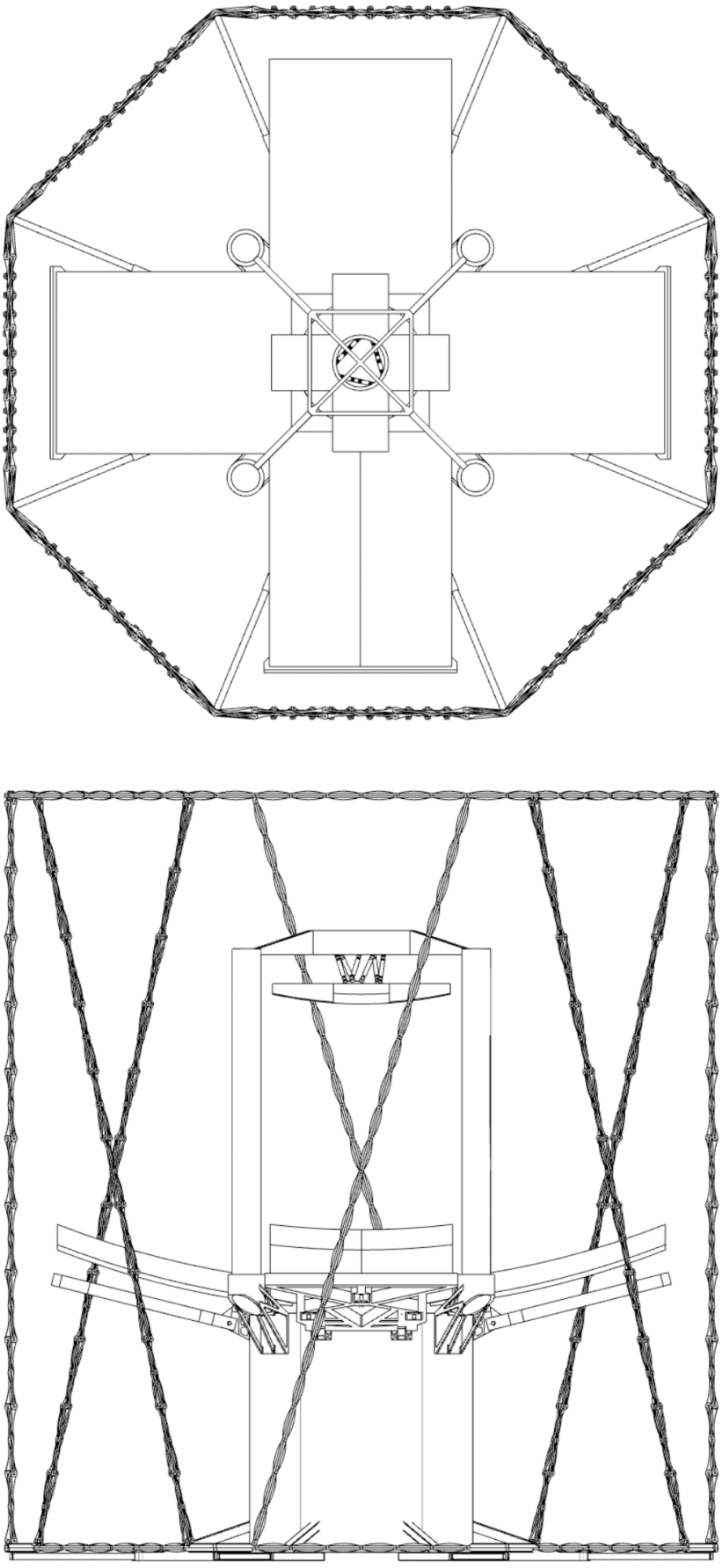

Figure 5.29: *Final pantographic baffle design in deployed configuration.*

6

Conclusion

This chapter summarizes and concludes the thesis, presents the key design points of the designed deployable baffle, and marks the path for future work.

6.1. Process Summary

The design process of a deployable baffle for the Deployable Telescope project started with critically reviewing the requirements already presented for the baffle of VIS Deployable Space Telescope in the past theses, and based on them, assembling a new, updated set of requirements. Then, a trade-off has been made among 7 alternatives based on 10 criteria to select the best deployment mechanism, which resulted in a close competition between telescopic and pantographic structures. The preliminary design of the pantographic structure has been made with working out the geometrical relationships of the pantographic linkages, assembling radial and axial modules, and connecting them in such a way that they support each other during deployment. The design phase ended with a preliminary optimization and material selection. Ultimately, apart from the pantographic structure having slightly higher global preferences, the decisive reason for its winning in the trade-off has been its novelty.

Then, the focus of the Deployable Space Telescope project has been shifted to thermal infrared wavelengths instead of visual, which basically restarted the projected. A preliminary thermal design has been done, and the achievable thermal environment within the baffle has been been presented. Based on the thermal design, the baffle height and thickness has been selected.

The work has been concluded with the detailed mechanical design, in which the baffle frame has been integrated with the instrument housing, the attachment of the radial and axial modules has been worked out, the pantographic linkages have been optimized for stiffness and mass. Finally, the deployment actuation of the baffle has been worked out, and the shroud and a truncated cone have been integrated to the baffle.

6.2. Design Summary

This section answers the research question: *"What are the most effective strategies to improve the deployability of the baffle of the Deployable Space Telescope, while ensuring compliance with thermal-, mass-, volume-, and structural requirements and budgets?"*

The designed baffle consists of pantographic arms that are connected in such a way that the entire structure has only one degree of freedom: if one angle or joint distance in the structure changes, the whole baffle follows. Two radial and eight axial modules make up the baffle frame. The radial modules are octagonal, with angulated pantographic arms in the vertices, and straight arms along the sides. The angulated units are responsible for the shape definition, while the straight arms between them increase the deployment ratio of the module. The axial modules are arranged above the straight radial units in a mirrored diagonal manner, this way optimizing the baffle stiffness, buckling resistance, and mass. The angle between the axial and radial modules do not change during deployment, but it constrained the baffle to a set of available heights. The integration of the baffle to the instrument housing is done by a telescopic mechanism in such a way that the baffle maintains its single degree of freedom.

The shroud of the baffle consists of two layers of MLI, with OSR-like coating on the outside, and Magic Black coating on the inside. A truncated cone is added to the top side of the baffle to limit the sun exposure

Table 6.1: *Design summary with key figures.*

Total mass, kg	12.76
Stowed volume, m^3	1.70
Deployed volume, m^3	5.30
Stowed eigenfrequency, Hz	103.2
Deployed eigenfrequency, Hz	16.2
Number of actuators	8

of the inner side of the baffle.

The deployment actuation is solved by 8 torsion springs placed at the vertices of the octagonal radial modules with axial module connections. The structure is held down at 16 locations with cables that are cut with thermal knives upon deployment command. Locking the structure in place after deployment is done by 8 latching pins close to the 8 actuators.

The key figures of the designed baffle is shown in Table 6.1. There is no point to compare these result directly with the previously designed baffles, as they have been prepared for the VIS DST. The 12.76 kg mass does not include the 25% uncertainty margin yet. If the heritage VIS mass and volume budgets are considered for the TIR telescope as well, then the baffle exceeds the mass budget by 0.95 kg (6.3%, including the mass uncertainty margin), and the volume budget by 0.2 m^3 (13%), however, the budgets have not been updated when changing the project to TIR. After the new budgets are available, the design can be critically reviewed. The stowed eigenfrequency meets the 100 Hz requirement, but to achieve that, the structure needs to be held down at 16 locations. The deployed eigenfrequency considerably exceeds 0.9 Hz requirement.

The compliance with the baffle functions is checked:

1. **Stable thermal environment.** The designed baffle greatly reduces the temperature differences and gradients within the baffle, and successfully shifts the temperature profiles towards colder temperatures, but without the thermal requirements from the other components within the baffle the compliance cannot be assessed. In the worst hot case the expected temperature ranges are presented in Figure 4.25 and Table 4.10 case a). IR telescopes usually prefer lower temperatures to limit IR self-emittance, therefore the introduction of some kind of cooling is foreseen in the future.

2. **Stray-light mitigation.** The baffle has Magic Black coating on the inner side, and every other component (apart from the mirror surfaces) facing the inner side of the baffle has high IR emissivity and UV absorptivity. The limited diameter of the deployed baffle, along with the introduction of the truncated cone further decrease the stray-light. However, updated requirements for the TIR telescope, and more detailed stray-light analysis are required to decide the compliance of the baffle.

3. **Protection from space debris.** Debris protection has not been considered during the design of the baffle. With increasing number of MLI layers the protection of the baffle increases, but it is impossible to quantify it without actual testing. Small size debris (<1 mm) impact probably does not degrade the ability of the DST to continue its mission, but its effect greatly depends on the debris velocity and what it hits. Medium - and large size debris, on the other hand, have a potential to cause an end of mission level impact, and more serious hardware (e.g. Whipple shield) are needed to provide protection against them. However, the addition of the extra hardware degrades the utility of the satellite, as it increases both the mass and volume of the telescope.

6.3. Requirement Verification

The compliance with the requirements are summarized in Table 6.2. Because of the change to TIR, many requirements cannot be verified yet, and several requirements are not covered by this thesis, but the finalized and covered requirements are all compliant. It is recommended to collect all required inputs and do the remaining analyses to be able to determine the compliance of all requirements.

Table 6.2: *Compliance with the requirements.*

ID	Requirement	Compliance	Comment
Survive Launch			
BAF-MEC-01	The baffle shall survive the launch in stowed configuration.	TBD	Further analysis needed.
BAF-MEC-01-01	The baffle shall survive a quasi-static load of 30g applied simultaneously to the x- and y- axes in the launcher coordinate frame in the stowed configuration during launch (TBC).	TBD	Further analysis needed.
BAF-MEC-01-02	The baffle shall survive a quasi-static load of 30g applied simultaneously to the x- and z- axes in the launcher coordinate frame in the stowed configuration during launch (TBC).	TBD	Further analysis needed.
BAF-MEC-01-03	The baffle shall survive a quasi-static load of 30g applied simultaneously to the y- and z- axes in the launcher coordinate frame in the stowed configuration during launch (TBC).	TBD	Further analysis needed.
BAF-MEC-01-04	The baffle shall have a minimum first eigenfrequency of 100 Hz in stowed configuration.	Compliant	First eigenfrequency: 103.2 Hz.
BAF-T-01	The stowed baffle shall survive a heat flux of 1135 W/m2 immediately after separation of the fairing.	TBD	Further analysis needed.
M2-T-01	The bulk temperature of the booms shall not exceed 373K during stowage (TBC).	TBD	Further input and analysis needed.
Successful Deployment			
BAF-MEC-02	The baffle shall be deployable.	Compliant	
BAF-MEC-02-01	The baffle deployment mechanism shall have at least TBD % reliability.	TBD	Further input and analysis needed.
BAF-MEC-02-02	The deployment sequcence shall not damage the baffle.	Compliant	
BAF-MEC-02-02-01	The baffle shall survive local- and global buckling loads during deployment.	TBD	Further analysis needed.
BAF-MEC-02-02-02	The baffle shall survive deployment shocks and vibrations.	TBD	Further analysis needed.
BAF-MEC-02-02-03	The baffle shall mitigate the creation of hot-spots during deployment such that it shall not result in consequential structural- or thermal damage that does not conform to the operational requirements.	TBD	Further analysis needed.
BAF-MEC-02-03	The baffle geometry shall not obstruct any telescope elements and not interfere with the optical performance.	Compliant	
BAF-MEC-02-03-01	The baffle shall achieve a deployed configuration that conforms to the operational requirements with a minimal position accuracy of 50 mm (TBC).	TBD	Further input and analysis needed.
BAF-MEC-02-03-02	The baffle shall have a clearance of at least 100 mm in all configarations between any point of the baffle and each of the following elements of the telescope: M1, M2, PMSS, SMSS.	Compliant	
BAF-MEC-02-04	The baffle shall not impede the deployment of the primary- and secondary mirror.	Compliant	
BAF-MEC-02-04-01	The baffle shall deploy before the primary- and secondary mirror.	Compliant	
BAF-MEC-02-05	The baffle shall deploy in 1800 s (TBC).	TBD	Further input and analysis needed.
Perform Operations			
BAF-T-02	The baffle shall create a stable thermal environment for all sub-systems located inside the baffle, so that the mechanical displacement budgets will be met.	TBD	Further input and analysis needed.
BAF-T-02-01	The baffle shall maintain its operational functionality in both extreme cases of BOL- and EOL thermo-optical material properties.	TBD	Further input and analysis needed.
BAF-O-01	The straylight fraction of the incoming radiation on the detector shall be less than 1% (TBC) after correction.	TBD	Further input and analysis needed.
BAF-O-01-01	The internal layer of the baffle shall absorb at least 90% (TBC) of incident radiation in UV wavelength spectra.	Compliant	If the required value remains the 90%.
Survive OPS & Space Environment			
BAF-MEC-03	An impact of small sized debris (d <1mm) to the baffle shall not degrade the ability of the DST to continue its mission (TBC).	TBD	Further input and analysis needed.
BAF-MEC-04	The materials to be used for the baffle shall limit outgassing to a TML of <1 % and CVCM of <0.01 %.	TBD	Further analysis needed.
BAF-MEC-05	The baffle shall be resistant to atomic oxygen.	TBD	Further analysis needed.
BAF-MEC-06	The baffle shall be resistant to plasma present in DST orbit.	TBD	Further analysis needed.
BAF-MEC-07	The baffle shall be resistant to ionizing radiation.	TBD	Further analysis needed.
BAF-MEC-08	The baffle shall avoid electrical charging.	TBD	Further analysis needed.
BAF-T-03	The baffle shall survive the thermal operational- and environmental loads in deployed configuration.	TBD	Further analysis needed.
BAF-T-03-01	The baffle shall survive extreme hot and cold temperatures (including 15 K modelling uncertainties) bounded by the operational range of all used materials in the baffle.	TBD	Further analysis needed.
BAF-T-03-02	The baffle shall survive the thermal loads both with BOL- and EOL optical properties.	TBD	Further analysis needed.
BAF-MEC-09	The baffle shall survive the mechanical operational- and environmental loads in deployed configuration.	TBD	Further analysis needed.
BAF-MEC-09-01	The baffle shall survive on-board vibrations due to the reaction wheel in deployed configuration.	TBD	Further analysis needed.
BAF-MEC-09-02	The baffle shall mitigate the effect of thermal flutter in deployed configuration.	TBD	Further analysis needed.
BAF-MEC-09-03	The baffle shall survive vibration fatigue due to on-board vibrations and thermal flutter.	TBD	Further analysis needed.
BAF-MEC-09-04	The baffle structure shall have a minimum first eigenfrequency >0.9 Hz in deployed configuration (TBC).	Compliant	If the required value is <16.2 Hz.
M2-T-02	The bulk temperature of the SMSS booms shall not exceed 473K when deployed (TBC).	TBD	Further input and analysis needed.
Cost			
BAF-SYS-01	The total cost of the baffle shall be no more than TBD.	TBD	Further input and analysis needed.
Safety			
BAF-SYS-02	The baffle shall have an expected operational lifetime of 5 years.	TBD	Further input and analysis needed.
BAF-SYS-02-01	The baffle shall have a MTBF of at least 5 years for single point of failure components.	TBD	Further input and analysis needed.
BAF-SYS-03	Active elements of mechanisms, such as sensors, motor windings, brushes, actuators, switches and electronics, shall be redundant if a mechanism is is not completely redundant.	Compliant	
BAF-SYS-04	The baffle shall use space qualified parts, materials and procesess (PMP).	TBD	Further analysis needed.
BAF-SYS-05	The baffle shall be designed such that conformance to performance requirements can be demonstrated by thermal analyses and thermal test.	TBD	Further analysis needed.
BAF-SYS-06	Verification by analysis shall take into account uncertainties: a 15 K temperature calculation uncertainty margin and 25 % mass uncertainty.	TBD	Further input and analysis needed.
BAF-SYS-07	The baffle shall be designed using factors of safety (FoS) conform with ECSS-E-ST-32-10.	TBD	Further analysis needed.
BAF-SYS-07-01	The baffle shall use a minimum yield stress safety factor (FoS) of 1.25 for standard metallic materials	TBD	Further analysis needed.
BAF-SYS-07-02	The baffle shall use a minimum ultimate stress safety factor (FoS) of 1.5 for standard metallic materials.	TBD	Further analysis needed.
BAF-SYS-07-03	The baffle shall use a minimum buckling safety factor (FoS) of 2 for standard metallic materials.	TBD	Further analysis needed.
BAF-SYS-07-04	The baffle shall use a minimum fatigue safety factor (FoS) of 4 for standard metallic materials.	TBD	Further analysis needed.
Regulations			
BAF-SYS-08	The baffle shall not use any ITAR controlled components or technologies	Compliant	
BAF-SYS-09	The baffle shall comply with national and international regulations during AIT activities, launch, operations and EOL.	TBD	Further analysis needed.
BAF-SYS-10	The materials used in the baffle shall be non-toxic and have no known negative effect on human health.	TBD	Further analysis needed.
Flexibility			
BAF-SYS-11	The baffle design shall incorporate flexibility to accommodate modifications of requirements imposed on the TCS and deployement system during the project development phase.	Compliant	
BAF-SYS-12	The baffle design shall incorporate flexibility to offer design trimming capabilities to accommodate late requirement updates.	Compliant	
Constraints			
BAF-SYS-13	The volume of the baffle shall not exceed 1.5 m3 (threshold) / 0.75 m3 (goal) when in stowed configuration.	TBD	TIR volume budget required.
BAF-SYS-14	The stowed baffle shall not require any power during launch.	Compliant	
BAF-SYS-15	The operational functionality of the baffle, as well as the ability to survive the operations and space environment shall be compatible with the power- and radiation exchange of the solar panels.	TBD	Further input and analysis needed.
BAF-SYS-16	The baffle in deployed configuration should fit inside a TV/TB chamber to allow for thermal testing.	Compliant	
BAF-SYS-16-01	The maximum volume of the baffle in deployed configuration shall conform to the usable volume of the Large Solar Simulator from ESA/ESTEC: 10 m diameter and 15 m height.	Compliant	
BAF-SYS-17	The mass of the entire baffle including deployment mechanism shall not exceed 15 kg (TBC).	TBD	TIR mass budget required.
BAF-SYS-18	The baffle shall be given sufficient structural support by other sub-systems.	Compliant	
BAF-SYS-19	The baffle shall be manufacturable with compliance to the availability of parts and materials.	Compliant	

6.4. Recommendations for Future Work

The following list contains the recommended future work that are direct continuation of this thesis.

1. **TIR change.** This is the first thesis about the TIR DST, and the updated project is in its infancy. The missing requirements, budgets, designs, components, etc. are recommended to be prepared, and then

the baffle design needs to be revisited. Some decisions along the design process might be affected by the availability of more information. The deployment mechanism trade-off should be repeated for the TIR DST, as currently the pantographic structure has been selected for the VIS DST. Depending on the new mission parameters and telescope dimensions, the outcome of the trade-off might be different.

2. **Mechanical design in more detail.** In the current design of the the joints and pins nothing stops them to slide out of the holes of the pantographic arms. It is necessary to update their design in the future to prevent this. Additionally, the rotational motion of the arms around the pins is currently facilitated by PTFE coating that reduces friction. Other alternatives should be introduced and traded off to find the best solution for the baffle.

3. **(Scaled) prototypes.** Many decisions could be facilitated (e.g. deployment mechanism trade-off), and structural properties checked or verified with a (scaled) prototype. Additionally, the HDRMs and deployment actuators can be directly tested with prototypes, which can aid their fine-tuning, if needed.

4. **SMSS redesign.** Currently the Secondary Mirror Support Structure has multiple flaws (it intersects the VIS baffles in stowed configuration, and drives the baffle dimensions for a one-time deployment), therefore it is recommended to be redesigned, and in such a way that it should not drive the baffle design.

5. **Innovative manufacturing solutions.** During design optimization of the pantographic arms innovative manufacturing solutions (e.g. 3D printing) can be also considered, as they might be able to improve the stiffness/mass ratio of the baffle.

6. **Optical studies.** The result of optical studies (e.g. ray-tracing, stray-light analysis) is recommended to be considered in the design process, for example in the material selection for coatings, internal geometry selection for the baffle, etc. It also needs to be verified if the introduction of the truncated cone does not degrade the optical performance.

7. **Additional thermal analyses.** The thermal analyses in this thesis has been left at preliminary level. If more telescope parts are available, it is recommended to redo the thermal studies. Furthermore, more accurate baffle representation (coupled MLI parameters in accordance with the Doenecke-method) is advised. Currently only the worst hot case has been studied (December), but studies for all months are recommended to be prepared. The thermal analyses need to be extended to the stowed configuration as well to verify if the telescope survives the brief period before deployment.

8. **Active cooling.** The need for active cooling needs to be checked. Currently, only continuous cooling of the inner side of the baffle has been studied, but coolers with thermostat, and directly cooling sensitive telescope parts are recommended to be examined.

9. **Further analyses.** The compliance with several requirements cannot be decided yet, therefore it is recommended to perform the missing analyses to verify all requirements.

The change of the spectral range of the telescope during the preparation of the thesis has caused a sudden absence of requirements and budgets, which resulted in the need to work with the heritage of the visual telescope, as it had abundant information and designs readily available. If all the required information had been available for the thermal infrared baffle design, it is possible that the result of this thesis would have looked completely different. That is why it is crucial to revisit and critically review the important decisions made in this thesis when more information becomes available.

Because of the considerable radial thickness of the pantographic baffle in stowed configuration, the radial deployment ratio of the baffle needs to be big enough to justify the usage of a pantographic structure. If the radial deployment ratio is small or there is only axial deployment, there are possibly better deployment mechanisms that could fulfill the task with a simpler and/or lighter solution. On the other hand, the strength of the pantographic baffle lies in large deployment ratios, and the higher the deployment ratio is, the usage of pantographic structures is more and more justified.

The result of this thesis is not only the design of a deployable pantographic baffle for the thermal infrared Deployable Space Telescope, but also a design guide for deployable pantographic prisms that synchronously deploy in all directions, and have only one degree of freedom, consequently – in theory – only one actuator is enough to deploy them. With the presented geometrical relationships the base of the prism can be any regular polygon, and its dimensions can be customized easily.

Bibliography

[1] *ESA PSS-03-108 Issue 1. Spacecraft thermal-control design data handbook – Volume 1.* 1989.

[2] S.K. Agrawal, S. Kumar, M. Yim, and J.W. Suh. Polyhedral single degree-of-freedom expanding structures. In *Proceedings 2001 ICRA. IEEE International Conference on Robotics and Automation (Cat. No.01CH37164)*. IEEE, 2001. doi: 10.1109/robot.2001.933133. URL https://doi.org/10.1109/robot.2001.933133.

[3] I. Akkerhuis. *Deployable Space Telescope: Redesign of the Secondary Mirror Support Structure*. Master's thesis, Delft University of Technology, 2020.

[4] J. Antonenko. *BepiColombo Technology Status Review. EADS-ST*, 2005.

[5] J.W. Arink. *Thermal-Mechanical Design of a Baffle for the Deployable Space Telescope*. Master's thesis, Delft University of Technology, 2019.

[6] W. Belvin, Marco Straubel, Juan Fernandez, Martin Zander, and Martin Hillebrandt. *Advanced Deployable Structural Systems for Small Satellites*. 09 2016.

[7] Jasper Bouwmeester. Personal communication.

[8] Claus P. Cagran, Leonard M. Hanssen, Mart Noorma, Alex V. Gura, and Sergey N. Mekhontsev. Temperature-resolved infrared spectral emissivity of SiC and pt–10rh for temperatures up to 900°c. *International Journal of Thermophysics*, 28(2):581–597, May 2007. doi: 10.1007/s10765-007-0183-1. URL https://doi.org/10.1007/s10765-007-0183-1.

[9] Metal Coatings Corp. *Non Stick Fluoropolymer Coatings*, 2021. URL https://www.metcoat.com/ptfe-coatings.htm.

[10] Dr. Antonius de Rooij. *PTFE*, 2021. URL https://www.spacematdb.com/spacemat/datasearch.php?name=PTFE.

[11] Roelof Jan de Vries. Personal communication.

[12] Airbus Defence and Space Netherlands. *Hold Down and Release System*, 2015. URL https://www.airbusdefenceandspacenetherlands.nl/dsstuff/uploads/2016/02/HDRS.pdf.

[13] Jochen Doenecke. Survey and evaluation of multilayer insulation heat transfer measurements. In *SAE Technical Paper Series*. SAE International, July 1993. doi: 10.4271/932117. URL https://doi.org/10.4271/932117.

[14] Dennis Dolkens. Personal communication.

[15] Dennis Dolkens, Hans Kuiper, and Victor Villalba Corbacho. The deployable telescope: a cutting-edge solution for high spatial and temporal resolved earth observation. *Advanced Optical Technologies*, 7(6):365–376, November 2018. doi: 10.1515/aot-2018-0043. URL https://doi.org/10.1515/aot-2018-0043.

[16] ECSS-E-ST-10-04C. Space engineering – space environment. Standard, ESA-ESTEC, November 2008.

[17] P. Ehrburger, J. B. Donnet, A. R. Ubbelohde, J. W. Johnson, M. O. W. Richardson, and R. A. M. Scott. Interface in composite materials [and discussion]. *Philosophical Transactions of the Royal Society of London. Series A, Mathematical and Physical Sciences*, 294(1411):495–505, 1980. ISSN 00804614. URL http://www.jstor.org/stable/36374.

[18] Klaus D Goepel. Implementation of an online software tool for the analytic hierarchy process (AHP-OS). *International Journal of the Analytic Hierarchy Process*, 10(3), December 2018. doi: 10.13033/ijahp.v10i3.590. URL https://doi.org/10.13033/ijahp.v10i3.590.

[19] Valentin Gomez-Jauregui. *Tensegrity Structures and their Application to Architecture*. Master's thesis, Queen's University Belfast, 2004.

[20] Fabbio Hu. Personal communication.

[21] J. Marjan Hummel, John F. P. Bridges, and Maarten J. IJzerman. Group decision making with the analytic hierarchy process in benefit-risk assessment: A tutorial. *The Patient - Patient-Centered Outcomes Research*, 7(2):129–140, March 2014. doi: 10.1007/s40271-014-0050-7. URL https://doi.org/10.1007/s40271-014-0050-7.

[22] F. Jensen and S. Pellegrino. *Arm Development Review of Existing Technologies*, 2001.

[23] Amit Joshi. *LITHIUM ALUMINIUM ALLOYS The New Generation Aerospace Alloys*. 2020.

[24] E.A. Korhonen. *Design of a Deployable Baffle for the Deployable Space Telescope*. Master's thesis, Delft University of Technology, 2019.

[25] A. Krikken. *Design of the Secondary Mirror Support Structure for the Deployable Space Telescope*. Master's thesis, Delft University of Technology, 2018.

[26] Sudarshan Krishnan. Deployable structures: An interdisciplinary design process. In *2017 ASEE Annual Conference & Exposition Proceedings*. ASEE Conferences. doi: 10.18260/1-2--28104. URL https://doi.org/10.18260/1-2--28104.

[27] J.M. Kuipers. *DST Systems Engineering Document (revision December 2018)*, 2018.

[28] A.S.K. Kwan. A parabolic pantographic deployable antenna (PDA). *International Journal of Space Structures*, 10(4):195–203, December 1995. doi: 10.1177/026635119501000402. URL https://doi.org/10.1177/026635119501000402.

[29] ITP Engines UK Ltd. *ESATAN-TMS Workbench Getting Started Guide*, 2017.

[30] G.P. Marrewijk. *Aberration correction system for a Deployable Space Telescope*. Master's thesis, Delft University of Technology, 2018.

[31] Azo Materials. *Aluminum 8090 Alloy (UNS A98090)*, 2013. URL https://www.azom.com/article.aspx?ArticleID=8789.

[32] Mersen. *BOOSTEC® SiC Silicon Carbide Material*. URL https://www.mersen.com/sites/default/files/publications-media/gs-boostec-sic-silicon-carbide-mersen.pdf.

[33] M. Mobrem and C. Spier. Design and performance of the telescopic tubular mast. 2012.

[34] V. Nagy. *Literature Study: Thermomechanical Design and Deployment of the DST Baffle*, 2020.

[35] Viktor Nagy. *AE4S06 Spacecraft Mechatronics - Deployable Baffle Prototype*, 2019. URL https://www.youtube.com/watch?v=63FY2H1xoxg.

[36] NASA. *NASA Science: Infrared Waves*. URL https://science.nasa.gov/ems/07_infraredwaves.

[37] Lorenzo Olivieri, Francesco Branz, Matteo Duzzi, Riccardo Mantellato, Francesco Sansone, Enrico Lorenzini, and Alessandro Francesconi. *TETHERED ELECTROMAGNETIC CAPTURE: A CUBESAT MISSION CONCEPT*. 10 2015.

[38] S. Pellegrino, editor. *Deployable Structures*. Springer Vienna, 2001. doi: 10.1007/978-3-7091-2584-7. URL https://doi.org/10.1007/978-3-7091-2584-7.

[39] S.M. Pepper. *Design of a Primary Mirror Fine Positioning Mechanism for a Deployable Space Telescope*. Master's thesis, Delft University of Technology, 2018.

[40] R. Peyrou-Lauga. Using real earth albedo and earth ir flux for spacecraft thermal analysis. *47th International Conference on Environmental Systems, ICES-2017-142*, 2017.

[41] V. Rajendran, S. Muthu Kumaran, T. Jayakumar, P. Palanichamy, P. Shankar, and Baldev Raj. Microstructure and ultrasonic behaviour on thermal heat-treated al–li 8090 alloy. *Journal of Alloys and Compounds*, 478(1-2):147–153, June 2009. doi: 10.1016/j.jallcom.2008.11.067. URL https://doi.org/10.1016/j.jallcom.2008.11.067.

[42] Kelvin Roovers and Niels De Temmerman. Deployable scissor grids consisting of translational units. *International Journal of Solids and Structures*, 121:45–61, August 2017. doi: 10.1016/j.ijsolstr.2017.05.015. URL https://doi.org/10.1016/j.ijsolstr.2017.05.015.

[43] Thomas Saaty. *Group decision making: drawing out and reconciling differences*. RWS Publications, Pittsburgh, PA, 2008. ISBN 978-1-888603-08-8.

[44] DST Project Team. *3D model of the Deployable Space Telescope (Catia)*, 2018.

[45] Gunnar Tibert. *Deployable Tensegrity Structures for Space Applications*. PhD thesis, KTH Royal Institute of Technology, 2002.

[46] The Engineering ToolBox. *Friction and Friction Coefficients*, 2021. URL https://www.engineeringtoolbox.com/friction-coefficients-d_778.html.

[47] Inc. Toray Composite Materials America. *M55J data sheet*. URL http://stg.toray.testcrafting.com/file_viewer.php?id=4474.

[48] T.T.D. van Wees. *Thermal Modelling & Analysis of the Deployable Space Telescope*. Master's thesis, Delft University of Technology, 2019.

[49] Víctor Villalba, Hans Kuiper, and Eberhard Gill. Review on thermal and mechanical challenges in the development of deployable space optics. *Journal of Astronomical Telescopes, Instruments, and Systems*, 6(01):1, March 2020. doi: 10.1117/1.jatis.6.1.010902. URL https://doi.org/10.1117/1.jatis.6.1.010902.

[50] H. Daniel Wagner and Richard A. Vaia. Nanocomposites: issues at the interface. *Materials Today*, 7 (11):38–42, November 2004. doi: 10.1016/s1369-7021(04)00507-3. URL https://doi.org/10.1016/s1369-7021(04)00507-3.

[51] Peter Warren, Mark Silver, Benjamin Dobson, and Howard MacEwen. *Experimental characterization of deployable outer barrel assemblies for large space telescopes*. page 886008, 10 2013. doi: 10.1117/12.2025577.